Department of Construction Sciences
Solid Mechanics

ISRN LUTFD2/TFHF-17/5219-SE(1-138)

Sharp Edge Cutting Through Paperboard

Master's Dissertation by

Daniel Jern
and
August Leek

Supervisors:
M. Sc. Tommy Lindström, Tetra Pak® and ESSIQ AB
M. Sc. Alexander Persson, Tetra Pak®
Adj. Prof. Johan Tryding, Div. of Solid Mechanics

Examiner:
Prof. Mathias Wallin, Div. of Solid Mechanics

Printed by Media-Tryck AB, Lund, Sweden
For information, address:
Division of Solid Mechanics, Lund University, Box 118, SE-221 00 Lund, Sweden
Webpage: www.solid.lth.se

Acknowledgements

We would first like to thank our three supervisors for all their help, enthusiasm and for making this thesis fun and interesting. Tommy Lindström has always been available for discussion and assisted us with modelling issues, but has also given us a lot of laughter. Alexander Persson has supported us throughout the whole project and has contributed with a lot of ideas and input. Adj. Prof. Johan Tryding has shared his knowledge within paperboard and fracture mechanics and has also given us valuable feedback for our report. Without you three, this thesis would not have been possible and for this, we are ever so grateful.

Ph.D. Eskil Andreasson has with his positive attitude and pedagogical as well as enthusiastic mindset contributed to valuable input regarding presentation of results and fracture modelling.

Ass. Prof. Stephen Hall and Dag Svärd have contributed with their great experience in tomography analysis, which has made it possible to produce high quality tomography images.

Annika Andersson, Anna Bellini, Klas Bogsjö, Eric Borgqvist, Per-Göran Heide and Johann Steiner are only a few of the Tetra Pak® employees who have shown their interest in our progress and have helped us throughout our work.

Thank you all, for a pleasant time at Tetra Pak®.

Daniel Jern and August Leek
Lund, June 2017

Abstract

The aim of this thesis is to investigate the micro mechanical damage and the failure of paperboard during sharp edge cutting. Tetra Pak is at the very forefront of the food packaging industry and in order to keep this market position, continuous improvements are of great importance. Increased understanding of paperboard behaviour is a driving factor for these improvements, since it enables more accurate simulations and further on manufacturing optimisations.

This thesis is divided into two parts: Experimental testing and finite element modelling. The experiments are thoroughly evaluated by using tomography, microscopy and statistical analysis. The interesting observations made during the experiments are all clarified. Several possible modelling approaches are theoretically reviewed and a final finite element model using element deletion is implemented.

The physical reasoning about the cutting phenomenon, based on the experiments, contributes to an increased understanding of which parameters that affect the cutting and also the understanding of the virtual responses. The results from the finite element modelling captures the observations and responses.

This thesis constitutes a foundation from which further development should be based. Future work should include development of the testing procedure as well as the implemented finite element model.

Keywords:

Slitting, Cutting, Fracture mechanics, Fracture modelling, Crack propagation modelling, Paperboard modelling

Sammanfattning

Syftet med avhandlingen är att undersöka den mikromekaniska skadan och brottet av kartong vid skärning med skarp egg. Tetra Pak tillhör den absoluta spjutspetsen inom förpackningsindustrin, och för att behålla denna position krävs ständiga förbättringar. Ökad förståelse av kartongbeteende är en drivande faktor av dessa förbättringar, då det möjliggör mer pricksäkra simuleringar som i längden kan bidra till optimeringar i tillverkningsprocessen.

Uppsatsen består huvudsakligen av två delar: Experimentell testning och finita elementmodellering. Experimenten är noggrant utvärderade genom användning av såväl tomografi som mikroskopi, samt statistisk analys. Samtliga intressanta observationer som gjordes under experimenten klarläggs. Ett flertal tillgängliga modelleringsmetoder gås igenom teoretiskt och en slutlig finita elementmodel med elementborttagning implementeras.

De förda fysikaliska resonemangen om skärfenomentet, vilka är baserade på de genomförda experimenten, bidrar till ökad förståelse av de parameterarna som påverkar skäret samt ökad förståelse av de simulerade responserna. Resultaten från simuleringarna fångar upp samtliga av de experimentella observationerna.

Avhandlingen utgör en grund, från vilken vidare utveckling bör baseras. Framtida arbete bör inkludera vidare utveckling av såväl testutförandet som den framtagna finita elementmodellen.

Contents

1 Introduction **1**

1.1 Presentation of Tetra Pak 1

1.2 Background to assignment 1

1.3 Thesis objectives 3

1.4 Delimitations and assumptions 3

1.5 Basic introduction to paperboard 4

1.6 Notations 8

1.6.1 Indices 9

2 Measurements **11**

2.1 Introduction 11

2.1.1 Sample preparation 11

2.2 Tensile tests 12

2.2.1 Test equipment 12

2.2.2 Results 13

2.2.3 Analysis 16

2.3 Cutting tests 19
2.3.1 Test equipment 20
2.3.2 Screening experiments 24
2.3.3 Final experiments 44
2.4 Summary of performed measurements 51

3 Constitutive modelling **53**
3.1 In-plane orthotropic linear elasticity 53
3.2 Plasticity 54
3.2.1 Hill's yield criterion 58
3.2.2 Elasto-plastic stiffness tensor 60

4 Fracture and cutting **63**
4.1 Fracture mechanics 63
4.1.1 Cutting 66
4.2 Modelling 68
4.2.1 Cohesive elements 68
4.2.2 Extended finite element method 70
4.2.3 Element deletion 71

5 Modelling in Abaqus **73**
5.1 Tensile tests 73
5.1.1 Procedure 73

5.1.2 Results 75
5.2 Cutting tests 79
5.2.1 Procedure 79
5.2.2 Results 82
5.2.3 Analysis 91

6 Discussion and conclusions **93**
6.1 Summary of thesis outcome 93
6.2 Measurements discussion 93
6.3 Modelling discussion 95
6.4 Future work 97

Bibliography **99**

Appendix A Plastic data **101**

Appendix B Mean results - Screening tests **117**

Appendix C Statistics - Screening experiments **119**

Appendix D Measured results - Final experiments **131**

Appendix E Mean results - Final Experiments **137**

Chapter 1

Introduction

1.1 Presentation of Tetra Pak

Tetra Pak is a world leading food packaging company founded in Lund, Sweden by Ruben Rausing in 1951. The company offers complete solutions from food processing to finished packages, including packaging material, filling machines and equipment necessary to obtain an efficient production process. Today, Tetra Pak is located in more than 175 countries [24][25].

This thesis was carried out within the groups of Material Treatment - Finishing and Virtual Engineering at Tetra Pak Packaging Solutions in Lund.

1.2 Background to assignment

Packaging material typically consist of the base materials paperboard, polymer, aluminium foil and ink. In order to produce the rolls of packaging materials, different converting stages are gone through. These stages are often separated into three main processes: printing, lamination and slitting. During the printing process, ink is added to the paperboard through any of the printing methods used within Tetra Pak. The most commonly used printing method is flexography. In the printing station the paperboard is creased and punched (often referred to as cut within Tetra Pak, this internal notation is here avoided) as well. The lamination is where the final packaging material structure

is assembled. The different polymer layers and eventually aluminium foil are added and are alternated with sterilisation actions in order to ensure that the material is aseptic when it is assembled. The slitting process is where the full width rolls are cut into narrower one packages wide reels. The reels may then be fed to filling machines. A representative scheme of the packaging material conversion is presented in Figure 1.1

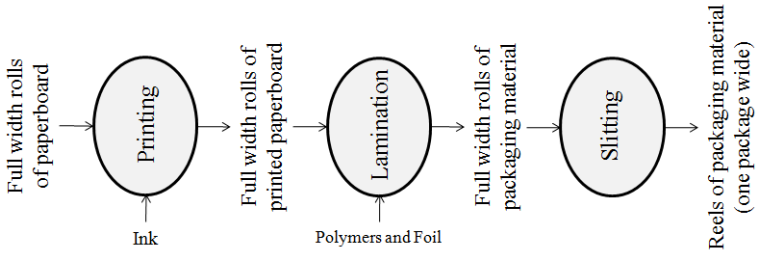

Figure 1.1: Scheme representing the conversion of the packaging material

During the converting line, there are several stages where the aim is to introduce controlled damage or failure to the plies. The slitting station is one of the stages where controlled failure of the packaging material is needed.

In the slitting station, the packaging material is cut into individual packaging material reels by sharp metal slitting blades. Unfavourable settings of the metal blades lead to bad cut quality, increased dust production from the paperboard and excessive blade wear. This in turn may lead to integrity issues. One method to analyse the cutting mechanics in the slitting station is by using finite element simulations which require calibrated material models from physical test data.

Much is today known about the macroscopic damage and failure of paperboard, for example see J. Tryding's PhD thesis [26]. Some studies have also been done on regular crack propagation, for example P. Mäkele has investigated commonly used crack propagation concepts and their suitability for paperboard modelling [16]. Less is, on the other hand, known about the damage and failure of paperboard fibres on a microscopic scale, especially when the failure is forced by a sharp external object, such as a slitting blade. Knowledge within this area would, in the long term, enable increased efficiency in several converting applications, such as the slitting process.

To be able to characterise the behaviour of the paperboard under such circumstances, measurements and modelling were performed and analysed during this thesis.

1.3 Thesis objectives

The purpose of this master's thesis was to contribute to improved knowledge of micro mechanical damage and failure of paperboard during sharp edge cutting. This was done by combining experimental measurements and numerical simulations with a theoretical study, in order to investigate the paperboard cutting process.

This paper will focus on the following issues:

- On which structural level is the paperboard damaged during the cutting process?
- What possible measuring techniques for sharp edge cutting can be used to characterise the cutting process?
- How can suitable material models be calibrated in a commercial finite element software?
- How can paperboard mechanics and its microscopic damage/failure behaviour be modelled?

1.4 Delimitations and assumptions

During this thesis some general delimitations and assumptions were made, which are presented below. Some further modelling assumptions are not presented here, but instead later throughout the report.

- The cutting process was assumed to be mainly affected by the paperboard plies in the packaging material. Other base material plies, such as aluminium and polymers, were therefore not considered in this work.
- The focus of the thesis was mainly on the paperboard behaviour and the cutting knife was treated as a rigid body during all virtual modelling. Aspects such as wear of the knife were therefore not taken into account during this process. Experimental methods, such as microscopy, were on the other hand used in order to investigate the impact of the cutting process on both the knife and the paperboard.

- The experiments were performed on paperboard samples consisting of four different bending stiffnesses, all consisting of a single ply.
- The considered cutting technique consisted of a razor blade cut, which is a much simpler method than the standard slitting process. It is on the other hand more alike methods used in other Tetra Pak applications.
- The focus was on sharp edged knives, specified in Section 2.3.1. I.e. the knife geometry was not varied.
- The modelling included just one of the failure approaches that were reviewed theoretically, see Section 4.2.

1.5 Basic introduction to paperboard

Paperboard consists of light-weight cellulose fibres distributed in a certain way into a number of stacked fibre planes. The fibre length varies between 0.5-5 mm and the fibre diameter between 10-50 µm depending on application. The longer and thinner the fibres are, the less stiff the paperboard is [5]. Shorter fibres are extracted from hardwood, such as birch or eucalyptus, and longer fibres are extracted from softwood, such as pine or spruce. The fibres possess, much alike carbon fibre and glass fibre, high tensile strength. The stiffness of a single ply paperboard is affected by the fibre dimensions, the number of stacked fibre planes, the mass per area ratio, i.e. grammage, as well as its moisture content.

The paperboard characterisation levels are illustrated in Figure 1.2.

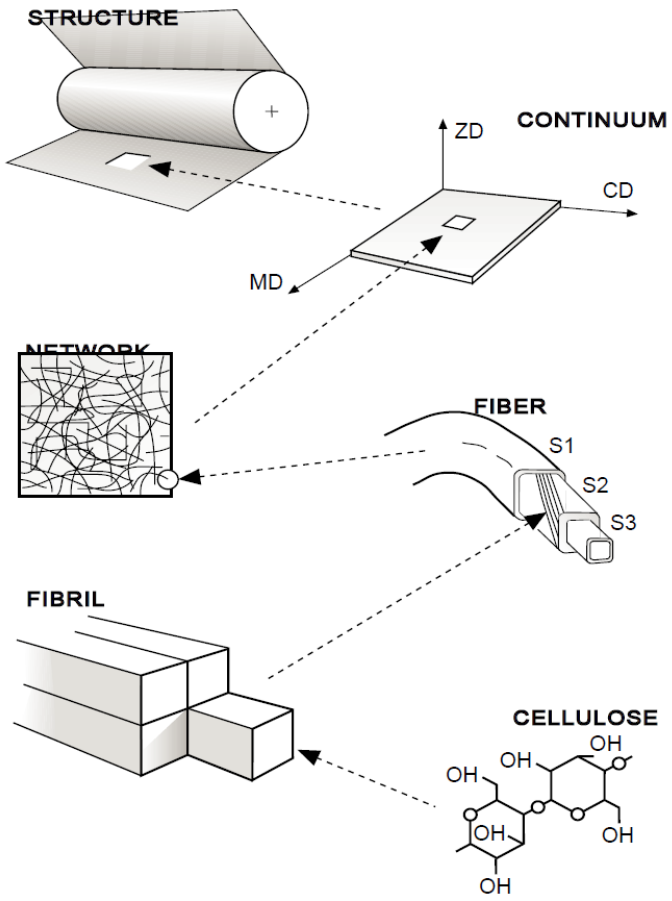

Figure 1.2: An illustration of the different characterisation levels for paperboard; From large sheets of paperboard to fibrils made of cellulose [26].

Due to the fibre based structure, paperboard shows a high directional dependence, i.e. anisotropy [6]. During the manufacturing process the fibres are aligned and stacked in such a way that an anisotropic material is created. This means that the material properties are different along three mutually-orthogonal axes, often referred to as Machine direction (MD), Cross direction (CD) and out-of-plane direction (ZD). The property differences between the directions are caused by the fibre orientation in the paperboard plies and a typical strength relation are MD:CD:ZD 100:50:1 [5].

The three orthogonal material axes are illustrated in Figure 1.3.

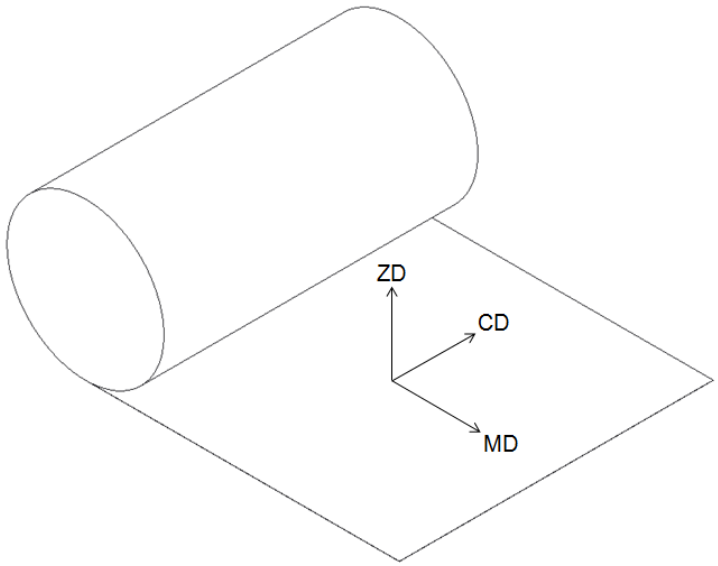

Figure 1.3: The orientation of the three mutually-orthogonal material axes; Machine Direction (MD), Cross-machine Direction (CD) and out-of-plane direction (ZD).

Paperboard may consist of a single ply or multiple plies with different fibre densities stacked upon each other. A typical stacking order is three plies with a top and a bottom ply with higher density. This order gives rise to bending properties similar to an I-beam, which has a higher bending stiffness per unit weight compared to a beam of solid rectangular cross-section [5]. This behaviour is illustrated in Figure 1.4.

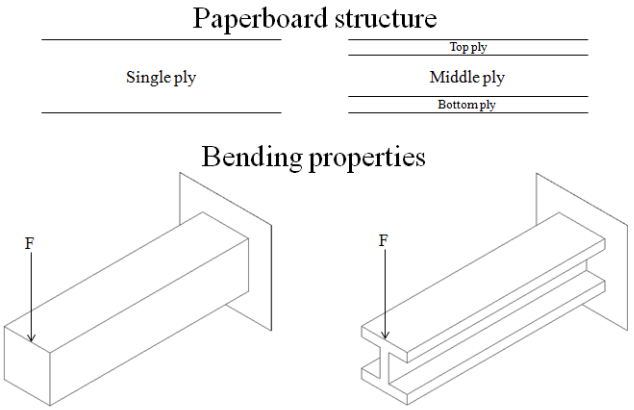

Figure 1.4: An illustrative explanation of how the different plies contribute to the bending properties.

Paperboard differ from ordinary paper due to its flexural rigidity, more often referred to as bending stiffness. This quantity is measured by bending a clamped paperboard

sample a specified angle and thereafter reading the resulting bending force [21]. The bending stiffness of the sample is the magnitude of this measured force. This quantity is measured in milliNewton [mN].

Paperboard possesses a number of favourable properties such as a high strength to weight ratio and good cuttability and foldability [5]. On the other hand it is very sensitive to moisture, which will impair the mechanical properties extensively. It is therefore of great importance to protect the paperboard surface, especially in the food packaging industry. Hence, packaging material consists of several plies of different materials, each ply contributing to specific properties. Such properties may not have to be coupled to mechanical properties, but can be specific chemical as well as optical properties. An example of this is the aluminium foil used in aseptic (sterile) packages, which adds an oxygen barrier to the package material as well as prevents UV light from making contact with the content and bacteria to diffuse. Two typical packaging material compositions can be seen in Figure 1.5.

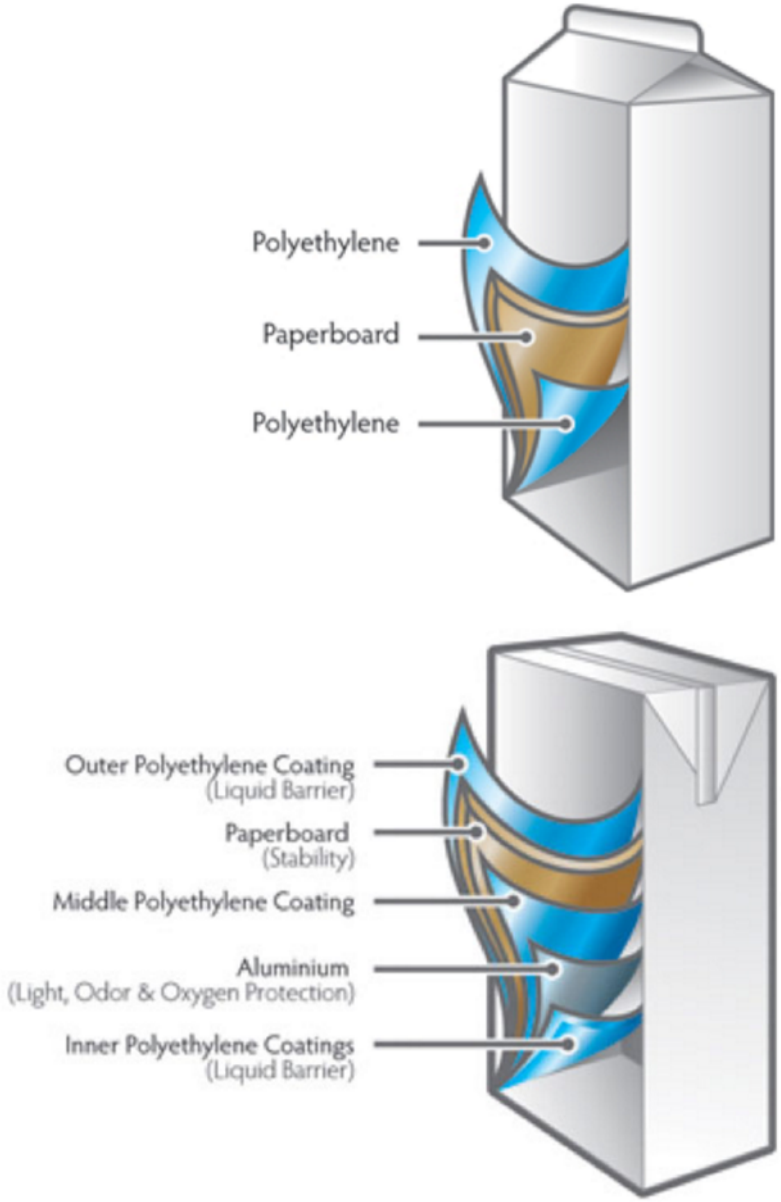

Figure 1.5: Typical packaging material composition for a non-aseptic packaging, at the top, and for an aseptic packaging, at the bottom [7].

1.6 Notations

Throughout this report, both matrix and tensor notations are used. The following index-free notations were adopted for second and fourth order tensors

$m_i \Leftrightarrow \boldsymbol{m}$	$M_{ij} \Leftrightarrow \boldsymbol{M}$	$M_{ijkl} \Leftrightarrow \mathbb{M}$
First order tensors	Second order tensors	Fourth order tensors

To be able to describe the loading in an inelastic domain it is convenient to describe the elastic and the plastic strains separately. The notation introduced in the relation below will therefore be used throughout this paper.

$$\boldsymbol{\varepsilon} = \boldsymbol{\varepsilon}^e + \boldsymbol{\varepsilon}^p$$

where ε^e and ε^p answer to the elastic and the plastic strains, respectively. Note that this notation is only valid for a small deformation setting. In a more general case a multiplicative split of the deformation gradient would be more accurate. Small deformations were therefore assumed during all constitutive calibration. The strains were during the calibration procedure measured in engineering strain and the stresses in engineering stress.

Abbreviations are introduced continuously throughout the report together with their meaning.

Cutting, in this thesis, refers to sharp edge cutting with a razor blade, and not punching operations that cutting often refers to at Tetra Pak.

1.6.1 Indices

In all mathematical expressions in this thesis, the material directions MD, CD and ZD are referred to as 1, 2 and 3, respectively. Two examples are listed below.

$$E_{\text{MD}} \Rightarrow E_1$$
$$\varepsilon_{\text{MD-CD}} \Rightarrow \varepsilon_{12}$$

When dealing with other configurations than MD-CD-ZD, a tilde is added to the tensor notation. Apart from the addition of tilde, the same subscripts are used for other configurations. The subscripts in combination with tilde, do therefore refer to another configuration than MD-CD-ZD.

Chapter 2

Measurements

2.1 Introduction

The measurements section is divided into two parts: Tensile testing and Cutting testing. The purpose of the first experimental part, the tensile testing, was to gain knowledge of the paperboard behaviour on a large scale. This enabled calibration and accurate modelling of the paperboard in areas outside the cutting zone. The cutting testing was a more innovative process which Tetra Pak has an ambition to continuously improve. The purpose was to examine the damage of the paperboard caused by the knife interaction. Properties that may be of interest were differences in fibre structure, the size of the damage effected region along the crack path and whether there are any palpable differences between the effects on paperboard of different qualities or not. The different effects that arose during the cutting was later examined with microscopy and tomography.

2.1.1 Sample preparation

Four paperboard types of different bending stiffnesses, all consisting of a single ply, were used in the experiments. For the tensile tests, specimens dimensioned 50×15 mm were used and for the cutting tests the specimen dimensions were altered between 80×70 mm and 80×100 mm. The paperboard samples were also divided into three different directions; MD, CD and 45°.

Before initiating the tests, all paperboard material was conditioned at 60°C in a drying cabinet for 30 minutes and thereafter kept at 23°C ±1°C and 50 % RH for at least three hours. All tests were thereafter performed at 23°C ±1°C and 50 % RH. This is all according to ISO 187.

Furthermore, thickness, grammage and density were measured for each paperboard quality. This was done by using a scale and a pair of digital calipers with a precision of 0.1 µm.

2.2 Tensile tests

In order to build and calibrate a theoretical paperboard model, measurements of the mechanical deformation for the desired paperboard qualities are required. To be able to capture the in-plane properties, three types of deformation measurements are needed for an orthotropic assumption: Uni-axial tension in MD, CD and 45° [18]. The MD and CD measurements yield information about the tensile properties in the principal in-plane directions, while the 45° test enables information about the in-plane shear properties. In order to capture quality variance, twelve tests were performed per material quality and direction. The constant rate of elongation was 7 mm/min for all tests.

2.2.1 Test equipment

When performing the tensile tests, a tensile machine from Instron 3360 Series Dual Column Tabletop Testing Systems was used together with a software called Bluehill, which enabled handling of the test data. The testdata could thereafter be processed and plotted using MATLAB. The tensile equipment is shown in Figure 2.1.

Figure 2.1: The used tensile equipment [12].

2.2.2 Results

Before initiating the tensile tests, mean values of thickness, grammage and density were measured. These quantities are presented in Table 2.1 below.

Table 2.1: Measurements of mean values of density, thickness and grammage for each paperboard bending stiffness.

Property	30 mN	80 mN	150 mN	260 mN
Density [kg/m^3]	870	840	800	780
Thickness [µm]	190	260	330	400
Grammage [g/m^2]	160	220	260	310

The results obtained by the tensile tests consisted of measured force and displacement, which allowed determination of several linear elastic mechanical material properties as well as the evolution of the plastic strains. For further explanation of the use of the plastic strain data, see Section 2.2.3.

Furthermore, out-of-plane data were collected from earlier tests performed at Tetra Pak [25].

The results from the tensile tests are presented in Figure 2.2 - 2.5 and the obtained properties are summarised in Table 2.2 together with the collected out of-plane-data. Note that all data after tensile failure have been removed in Figure 2.2 - 2.5.

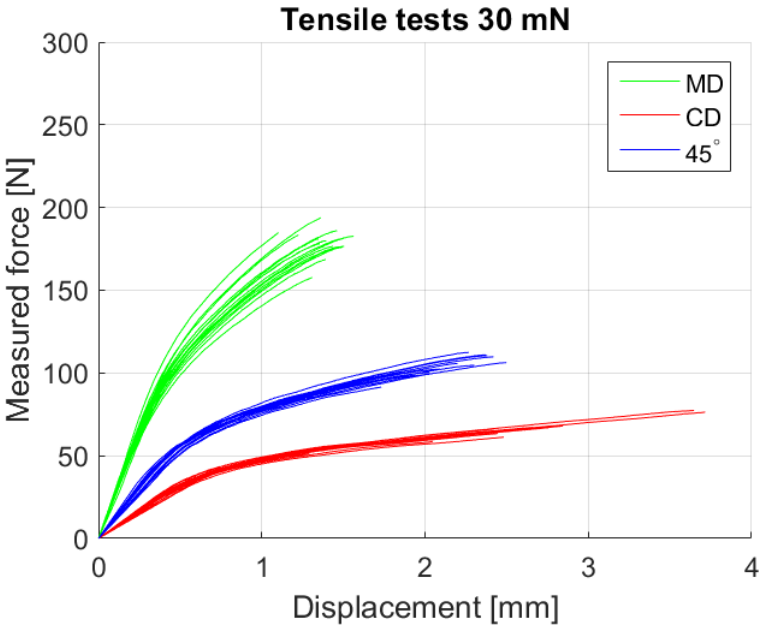

Figure 2.2: Results from tensile tests carried out with 30 mN paperboard presented in a force-displacement curve.

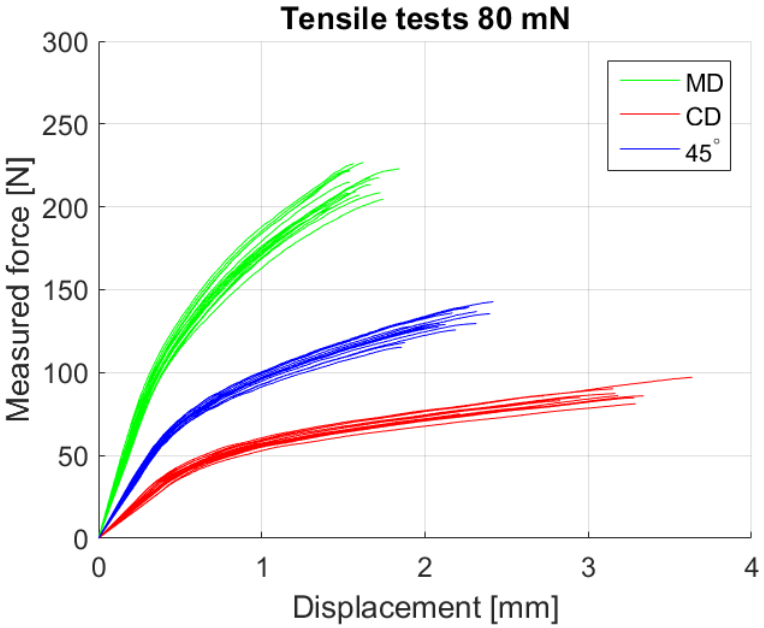

Figure 2.3: Results from tensile tests carried out with 80 mN paperboard presented in a force-displacement curve.

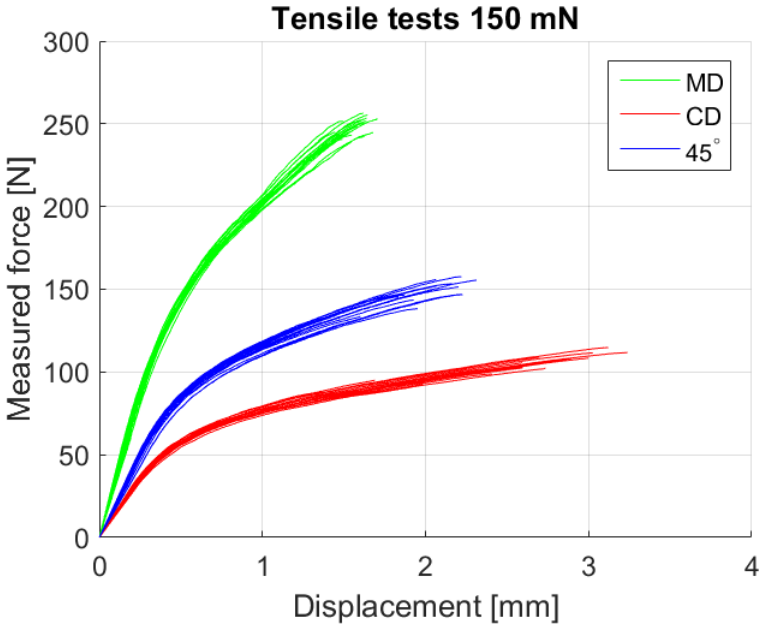

Figure 2.4: Results from tensile tests carried out with 150 mN paperboard presented in a force-displacement curve.

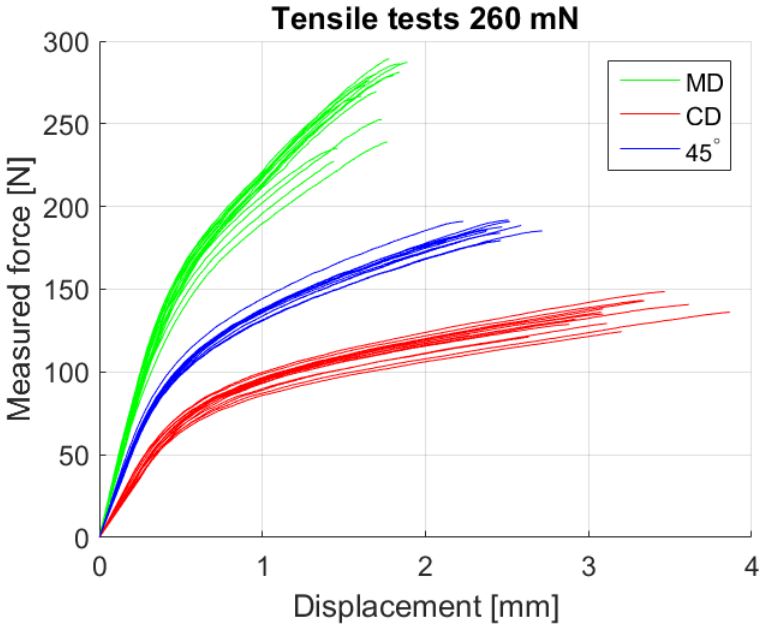

Figure 2.5: Results from tensile tests carried out with 260 mN paperboard presented in a force-displacement curve.

2.2.3 Analysis

The relation between force and displacement in Figure 2.2 - 2.5 is initially linear and becomes non-linear after a certain force value for all four materials. Previous work show that some part of the deformation is not recovered after unloading of a previously loaded sample [11], which indicates that permanent deformation is present. When considering this behaviour in modelling terms, it is of great importance to handle the linearly elastic part and the plastic part separately. This is handled by assuming elasto-plasticity. When the material is loaded elastically, the stresses are directly proportional to the strains, but during plastic loading no such proportionality exists. By assuming elasto-plastic behaviour and dividing the elastic and the plastic part, one get a partitioning between elastic and plastic strains. This clearly requires an assumption regarding initiation of plasticity, which was done by calculating mean values of the Young's moduli, E, and thereafter evaluating for which stress and strain the Force-Displacement curve deviates from the linearity by 0.1 %. The found stress was set to the initial yield strength and the plastic stress-strain relation was from this point and on interpolated in accordance with the test data. Theory for the elasto-plastic modelling is described further in Chapter 3.

The Young's moduli for the different material directions do not only give information about the tensile elastic properties in each direction, but also about how the directional mechanical properties are related, i.e. the Poisson's ratio ν. The Poisson's ratio for a uni-axial tension case is defined as

$$\varepsilon^e_{\text{lateral}} = -\nu\varepsilon^e_{\text{axial}} \tag{2.1}$$

Baum, Brennan and Habeger [2] showed empirically that the root mean square value of the in-plane Poisson's ratios $\sqrt{\nu_{12}\nu_{21}} = 0.293 \pm 0.023$ is constant and independent of paper quality and relative humidity. When this is combined with the symmetry of the stiffness and flexibility matrix, i.e.

$$\frac{\nu_{12}}{E_1} = \frac{\nu_{21}}{E_2} \tag{2.2}$$

an approximate relation between the in-plane Poisson's ratios and the in-plane Young's modulus yields

$$\nu_{12} = 0.293\sqrt{\frac{E_1}{E_2}} \text{ and } \nu_{21} = 0.293\sqrt{\frac{E_2}{E_1}} \tag{2.3}$$

This proves to be a good assumption for machine-made paperboard.

As previously mentioned, the uni-axial tensile tests in MD and CD give information of the pure tensile properties. In order to capture the in-plane shear properties one would have to make a pure shear test, which may be difficult. It proves that by making a 45° test and making an orthotropic assumption, one could more easily determine the shear properties. This is done by transforming the uni-axial stress state $\tilde{\boldsymbol{\sigma}}$ at 45° to the MD-CD stress state $\boldsymbol{\sigma}$, i.e. $\boldsymbol{\sigma} = \boldsymbol{A}^T \tilde{\boldsymbol{\sigma}} \boldsymbol{A}$, where $\boldsymbol{A}$ is the transformation tensor. The given stress and strain state for the 45° configuration can be expressed as

$$[\tilde{\boldsymbol{\sigma}}] = \begin{bmatrix} \tilde{\sigma}_{11} & 0 \\ 0 & 0 \end{bmatrix}; \quad [\tilde{\boldsymbol{\varepsilon}}] = \begin{bmatrix} \tilde{\varepsilon}_{11} & \tilde{\varepsilon}_{12} \\ \tilde{\varepsilon}_{12} & \tilde{\varepsilon}_{22} \end{bmatrix} \tag{2.4}$$

How the two configurations are related is shown in Figure 2.6 below.

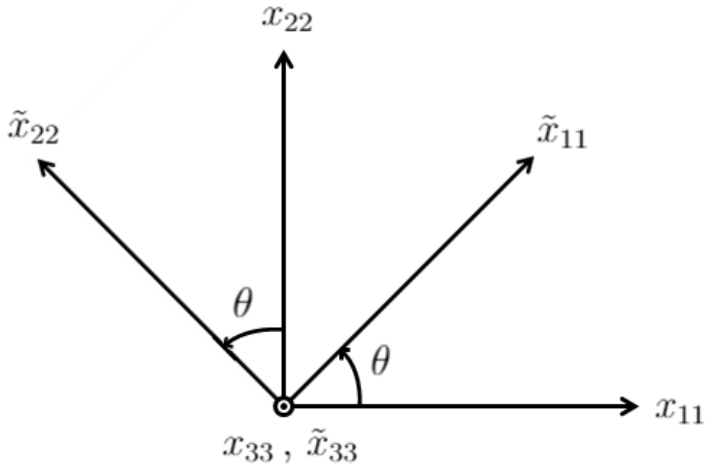

Figure 2.6: The 45° coordinate system ($\tilde{x}_{11}$-$\tilde{x}_{22}$-$\tilde{x}_{33}$) in relation to the MD-CD-ZD coordinate system (x_{11}-x_{22}-x_{33}), where $\theta = 45°$ is the angle of rotation.

The coordinates axes $\tilde{x}_{11}$ and $\tilde{x}_{22}$ can be expressed in terms of x_{11} and x_{22} by making the following in-plane transformation

$$\begin{cases} \tilde{x}_{11} = x_{11} \cos\theta + x_{22} \sin\theta \\ \tilde{x}_{22} = -x_{11} \sin\theta + x_{22} \cos\theta \end{cases} \quad \Leftrightarrow \quad \tilde{\boldsymbol{x}} = \boldsymbol{A}\boldsymbol{x} \tag{2.5}$$

With $\theta = 45°$, the transformation matrix $[\boldsymbol{A}]$ yields

$$[\boldsymbol{A}] = \frac{1}{\sqrt{2}} \begin{bmatrix} 1 & 1 \\ -1 & 1 \end{bmatrix}$$

The stress and strain state at 45° can now be expressed in the MD-CD configuration, by making use of $\boldsymbol{\sigma} = \boldsymbol{A}^T \tilde{\boldsymbol{\sigma}} \boldsymbol{A}$ and $\boldsymbol{\varepsilon} = \boldsymbol{A}^T \tilde{\boldsymbol{\varepsilon}} \boldsymbol{A}$, i.e.

$$[\boldsymbol{\sigma}] = \frac{\tilde{\sigma}_{11}}{2} \begin{bmatrix} 1 & 1 \\ 1 & 1 \end{bmatrix}; \quad [\boldsymbol{\varepsilon}] = \frac{1}{2} \begin{bmatrix} \tilde{\varepsilon}_{11} + \tilde{\varepsilon}_{22} - 2\,\tilde{\varepsilon}_{12} & \tilde{\varepsilon}_{11} - \tilde{\varepsilon}_{22} \\ \tilde{\varepsilon}_{11} - \tilde{\varepsilon}_{22} & \tilde{\varepsilon}_{11} + \tilde{\varepsilon}_{22} + 2\,\tilde{\varepsilon}_{12} \end{bmatrix} \tag{2.6}$$

The performed uni-axial tensile tests only enable measurements of axial strain in 45°, i.e. $\tilde{\varepsilon}_{11}$. By assuming that $\tilde{\sigma}_{11} = \tilde{E}_1\,\tilde{\varepsilon}^e_{11}$ is valid for the 45° state, the shear modulus G_{12} can be solved out of Hooke's law [13], i.e.

$$G = \left(\frac{4}{\tilde{E}_1} - \frac{1 - \nu_{12}}{E_1} - \frac{1 - \nu_{21}}{E_2} \right)^{-1} \tag{2.7}$$

The total strain tensor $\boldsymbol{\varepsilon}$ for elasto-plasticity can be divided into an elastic and a plastic part, which makes it possible to expand the strain expression in equation 2.6, i.e.

$$\begin{aligned} [\boldsymbol{\varepsilon}] = \frac{1}{2} &\begin{bmatrix} \tilde{\varepsilon}^e_{11} + \tilde{\varepsilon}^e_{22} - 2\,\tilde{\varepsilon}^e_{12} & \tilde{\varepsilon}^e_{11} - \tilde{\varepsilon}^e_{22} \\ \tilde{\varepsilon}^e_{11} - \tilde{\varepsilon}^e_{22} & \tilde{\varepsilon}^e_{11} + \tilde{\varepsilon}^e_{22} + 2\,\tilde{\varepsilon}^e_{12} \end{bmatrix} + \\ + \frac{1}{2} &\begin{bmatrix} \tilde{\varepsilon}^p_{11} + \tilde{\varepsilon}^p_{22} - 2\,\tilde{\varepsilon}^p_{12} & \tilde{\varepsilon}^p_{11} - \tilde{\varepsilon}^p_{22} \\ \tilde{\varepsilon}^p_{11} - \tilde{\varepsilon}^p_{22} & \tilde{\varepsilon}^p_{11} + \tilde{\varepsilon}^p_{22} + 2\,\tilde{\varepsilon}^p_{12} \end{bmatrix} \end{aligned} \tag{2.8}$$

The only quantities in equation 2.8 that are known from the tests, are the elastic and plastic axial strains $\tilde{\varepsilon}^e_{11}$ and $\tilde{\varepsilon}^p_{11}$, respectively. In order to get information about the plastic shear strain $\varepsilon^p_{12} = \tilde{\varepsilon}^p_{11} - \tilde{\varepsilon}^p_{22}$, some assumptions are required regarding $\tilde{\varepsilon}^p_{22}$. Measurements made in Xia, Boyce and Parks [29] and Harrysson and Ristinmaa [11] show that the relation between the axial and lateral strains is approximately constant for the entire elasto-plastic domain. It is therefore, in accordance with these measurements, assumed that

$$\begin{aligned} \frac{\varepsilon^e_{22}}{\varepsilon^e_{11}} = \frac{\varepsilon_{22}}{\varepsilon_{11}} = \frac{\varepsilon^p_{22}}{\varepsilon^p_{11}} = -\nu_{12} \\ \frac{\tilde{\varepsilon}^e_{22}}{\tilde{\varepsilon}^e_{11}} = \frac{\tilde{\varepsilon}_{22}}{\tilde{\varepsilon}_{11}} = \frac{\tilde{\varepsilon}^p_{22}}{\tilde{\varepsilon}^p_{11}} = -\tilde{\nu}_{12} \end{aligned} \tag{2.9}$$

With $\varepsilon^e_{22} = -\nu_{12}\varepsilon^e_{11}$ together with the given strain state in (2.6) and the symmetry of the stiffness and flexibility matrix according to (2.2), the following relation yields

$$\tilde{\nu}_{12} = \frac{E_1E_2 - E_2G_{12}(1-2\,\nu_{12}) - E_1G_{12}}{E_1E_2 + E_2G_{12}(1-2\,\nu_{12}) + E_1G_{12}} \tag{2.10}$$

Finally, the plastic shear strains can now be expressed as

$$\varepsilon^p_{12} = \tilde{\varepsilon}^p_{11}(1+\tilde{\nu}_{12}) \tag{2.11}$$

The relation in (2.11) together with the stress state in (2.6), enable the interpolation of the plastic stress-strain relation in accordance with what is previously mentioned in this section.

Furthermore, small deformations have been assumed during all constitutive calibration during this thesis. This also means that all strain quantities are measured in engineering strain $\varepsilon_E = \Delta u/l_0$.

The resulting material properties based on the tensile tests are presented in Table 2.2.

Table 2.2: Summary of linear elastic mechanical properties. The plastic stress-strain evolution can be found in Appendix A.

Property	30 mN		80 mN		150 mN		260 mN	
	mean	SD	mean	SD	mean	SD	mean	SD
E_1 [MPa]	5 000	6.26 %	4 200	8.68 %	3 900	7.76 %	3 400	7.09 %
E_2 [MPa]	1 200	6.99 %	1 200	9.06 %	1 500	4.78 %	1 500	8.22 %
$\tilde{E}_1$ [MPa]	2 300	8.45 %	2 200	5.47 %	2 200	6.60 %	2 400	7.48 %
ν_{12} [-]	0.59	-	0.55	-	0.47	-	0.45	-
ν_{21} [-]	0.15	-	0.15	-	0.18	-	0.19	-
G_{12} [MPa]	1 000	-	1000	-	900	-	1 000	-

2.3 Cutting tests

To get data and information about the cutting process, physical cutting tests were performed. These tests were of great importance, both to collect data to calibrate

a virtual model against and to get knowledge about the paperboard damage during cutting.

The cutting tests were done in two stages. First, a screening was done and after investigation of the screening results an additional experiment session was done, called 'Final experiments'. The purpose of the screening tests was to study which parameters that affect the cut and therefore should be considered during the final experiments. During this session all available parameters were varied. The final experiments were performed in a greatly reduced parameter space, which allowed a more comprehensive test plan. The test planes for the screening and the final experiments are presented in Table 2.3 and 2.7, respectively.

During the performed cutting tests, a significant out-of-plane deformation was observed. In order to investigate and measure this observation a microscopic analayis was performed. Thus, the purpose of the microscopical analysis was to determine if there was any relation between the measured deformation and the input parameters. The deformation was measured at two different measuring points per sample and to be able to compare the deformation between the different paperboard stiffnesses, it was designated as a strain.

In order to observe the crack path, the crack tip and the surrounding crack region in detail an X-ray tomograph was used. Interesting properties to investigate were the size of the region that is affected by the cut, fineness of the cut (in terms of fuzz and fibre reorientation) and other phenomena present, such as delamination or densification.

2.3.1 Test equipment

Cutting rig

The cutting tests were also performed by using the tensile equipment mentioned in Section 2.2.1, together with an additional cutting rig. A sharp edge blade was attached to the tensile device and thereafter forced down through the paperboard sample, similar to a compression test. An illustration of how the cutting rig was mounted and used, is shown in Figure 2.7

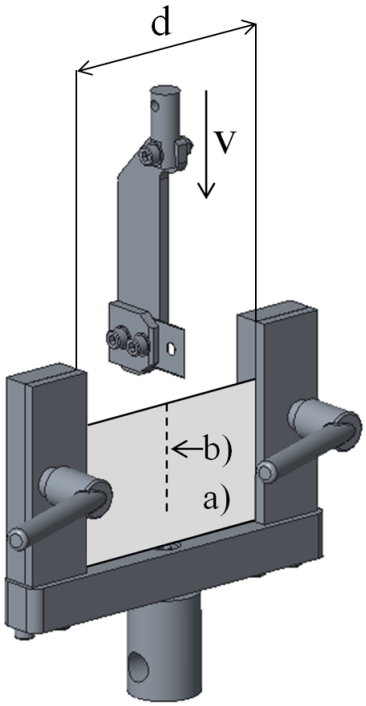

Figure 2.7: The cutting rig. Paperboard: a), Fictitious cutting line: b), Clamping distance: d and Cutting velocity: v.

The edge geometry of a brand new knife is presented in Figure 2.8. This geometry was also used for the virtual modelling.

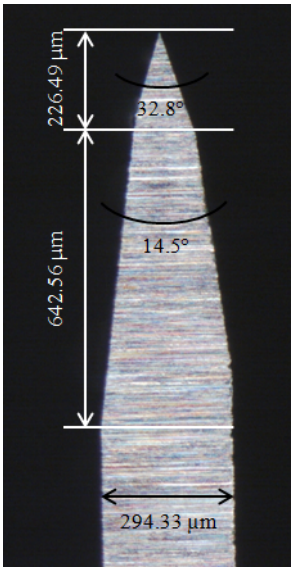

Figure 2.8: The edge geometry of a brand new knife.

Microscope

The used microscope was of the model Olympus SZX12. A magnification factor up to 90x was used during the measurements.

When investigating the cut sample in the microscope, three measurements were made per sample; two deformed thicknesses and one undeformed thickness. First of all, the sample was cut into two separate pieces according to Figure 2.9.

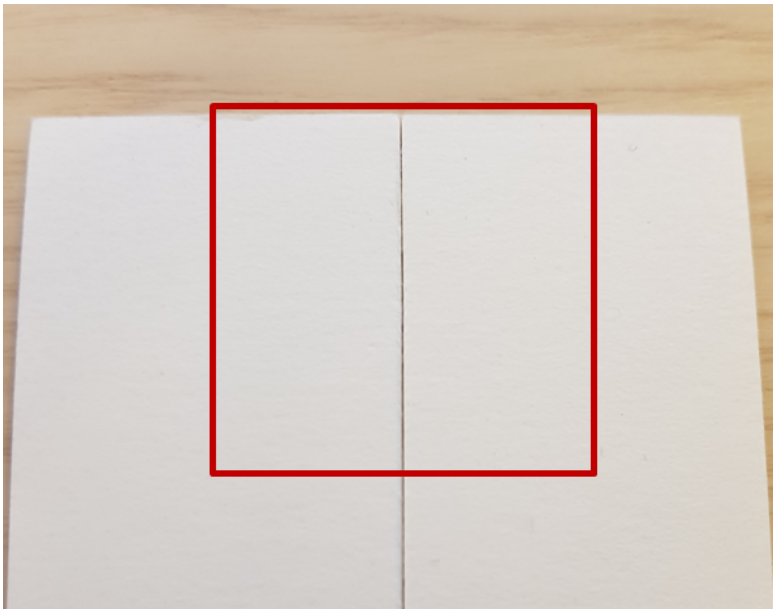

Figure 2.9: The considered area (enclosed in red) when examining the out-of-plane deformation in microscope.

The paperboard thickness along the crack was thereafter measured for each piece. The undeformed thickness was measured for an area far away from the crack. This undeformed thickness was later used as a reference length when computing the out-of-plane strain.

Tomograph

Tomography has some obvious benefits compared to visual observations. It is a non-destructive technique, which offers the opportunity to observe an object throughout its volume without destroying it. This is done by placing the object between a X-ray

source and a detector. The divergence of the X-ray beam allows some variation in magnification by moving the object closer or farther from the source. This kind of magnification is often referred to as geometrical magnification. In addition to the geometric magnifications, optical magnification was also used. The optical magnification was obtained using a lens. The principle of the magnification is presented in Figure 2.10

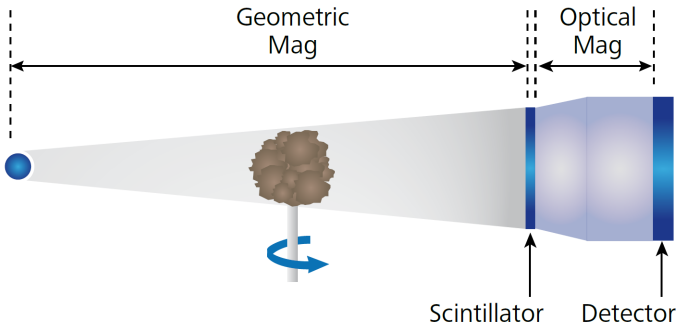

Figure 2.10: Principle of geometric and optical magnification in the tomograph [30].

When the X-ray beams hit the detector, a 2D image is generated. Depending on the path from the source to the detector the beams have different energy, which is represented by a grey scale. By rotating the object, several 2D images are collected. These are then assembled to form a 3D representation of the specimen.

The model of the tomograph used during this project was Zeiss Xradia XRM 520.

The region that was investigated during the tomography analysis is shown below in Figure 2.11.

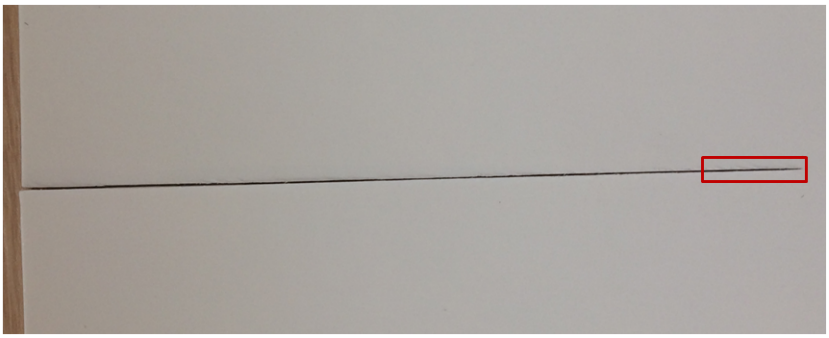

Figure 2.11: The investigated region (enclosed in red) during the tomography analysis.

2.3.2 Screening experiments

The purpose of the screening tests was to identify which parameters that significantly affect the cut. The available test equipment together with the different material qualities, made it possible to vary the following parameters

- Material parameters
  - Bending stiffness
  - Material orientation
  - Clay coating - Yes or No
- Cutting rig parameters
  - Cutting speed
  - Clamping distance
  - Knife angle - α
  - Knife angle - β

The bending stiffness was varied between 30 mN, 80 mN, 150 mN and 260 mN. The material orientation indicates in which direction the cutting is performed. The clay coating-parameter decides whether the cut is initiated on the clay coating side or not. Cutting speed is the (constant) speed of the cutting knife. Clamping distance is the distance referred to as d in Figure 2.7. Knife angle - α is defined in Figure 2.12.

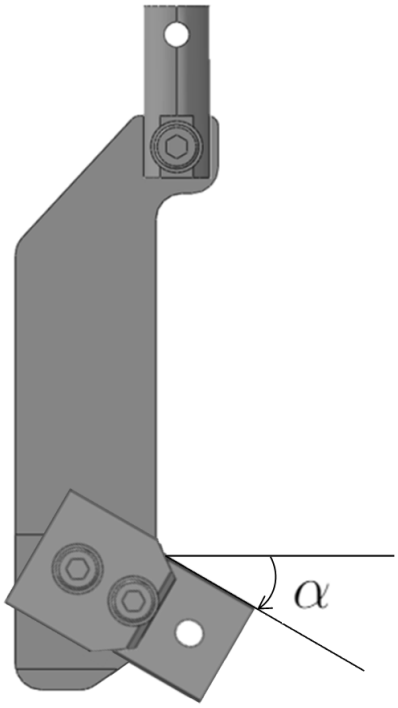

Figure 2.12: Knife angle - α.

How the knife angle - β is defined, is shown in Figure 2.13.

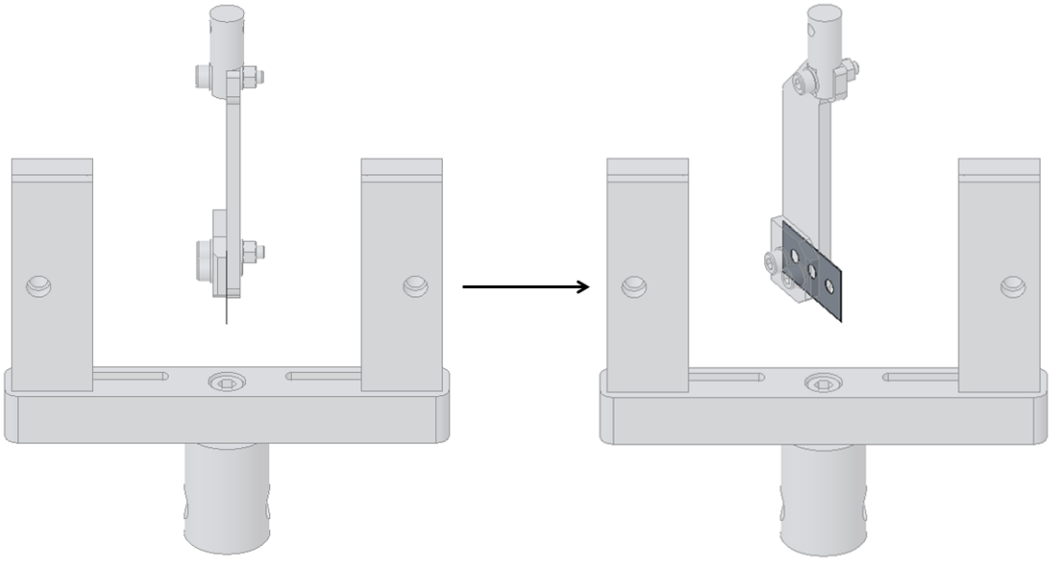

Figure 2.13: Knife angle - $\beta = 0°$ (to the left) and Knife angle - $\beta = 30°$ (to the right).

The screening tests were performed by varying one parameter at a time in accordance with the test plan in Table 2.3 below.

Table 2.3: Test plan for the Screening tests

#	Number of tests	Bending stiffness [mN]	Cutting speed [mm/s]	Clamping distance [mm]	Material orientation	Knife angle - α [°]	Knife angle - β [°]	Clay coating	Comments:
1	3	150	10	50	MD	0	0	-	Reference
2	3	30	10	50	MD	0	0	-	
3	3	80	10	50	MD	0	0	-	
4	3	260	10	50	MD	0	0	-	
5	3	150	1	50	MD	0	0	-	
6	3	150	0.1	50	MD	0	0	-	
7	3	150	10	80	MD	0	0	-	
8	3	150	10	50	CD	0	0	-	
9	3	150	10	50	45°	0	0	-	
10	3	150	10	50	MD	17.5	0	Yes	
11	3	150	10	50	MD	35	0	Yes	
12	3	150	10	50	MD	35	0	No	
13	3	150	10	50	MD	0	5	-	
14	3	150	10	50	MD	0	45	-	

Results

The results from the performed screening tests are presented in terms of force-displacement curves in Figure 2.14 - 2.20.

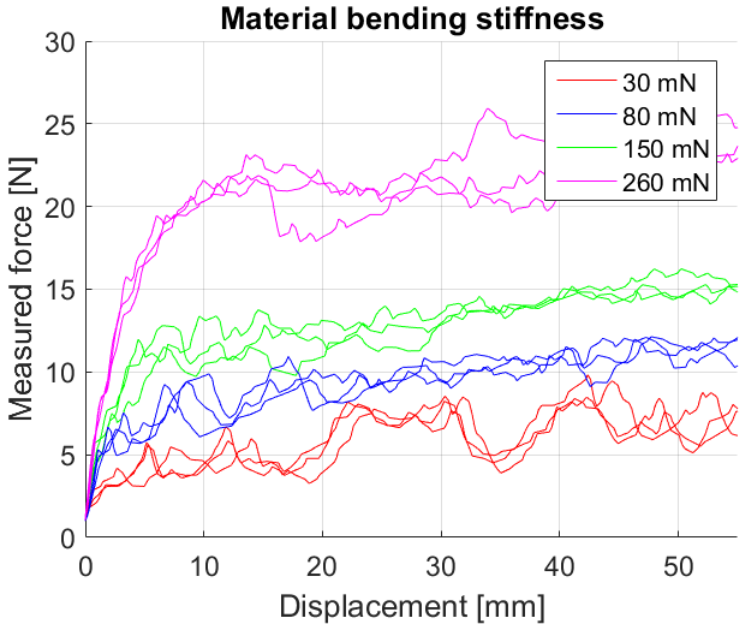

Figure 2.14: Results from the screening cutting tests for different bending stiffnesses presented in a force-displacement curve. The tests were performed with the cutting speed 10 mm/s, a clamping distance of 50 mm, MD as the cutting direction and the knife angles $\alpha = 0°$ and $\beta = 0°$.

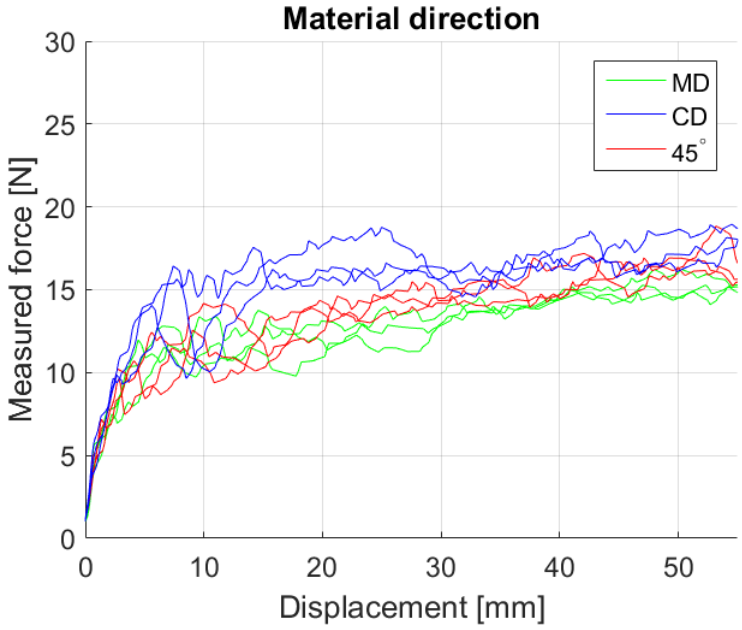

Figure 2.15: Results from the screening cutting tests for different material directions presented in a force-displacement curve. The tests were performed on a sample of bending stiffness 150 mN with the cutting speed 10 mm/s, a clamping distance of 50 mm and the knife angles $\alpha = 0°$ and $\beta = 0°$.

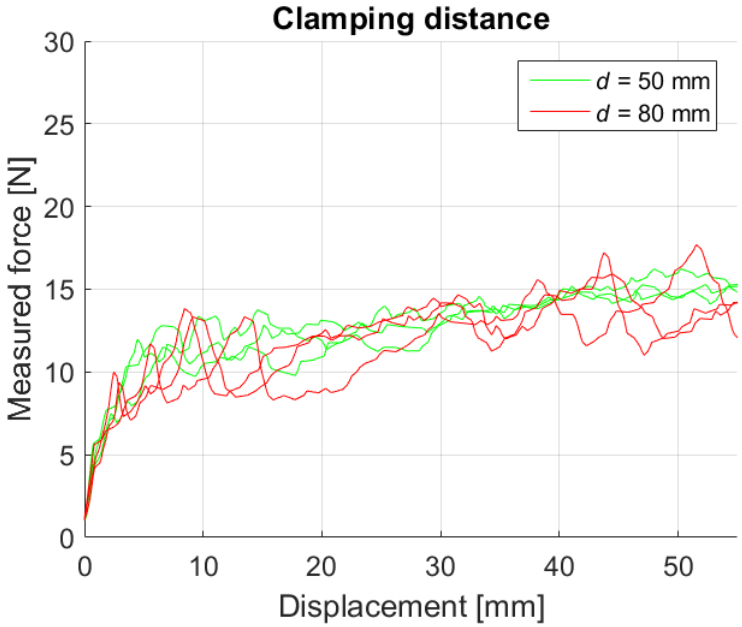

Figure 2.16: Results from the screening cutting tests for different clamping distances presented in a force-displacement curve. The tests were performed on a sample of bending stiffness 150 mN with the cutting speed 10 mm/s, MD as the cutting direction and the knife angles $\alpha = 0°$ and $\beta = 0°$.

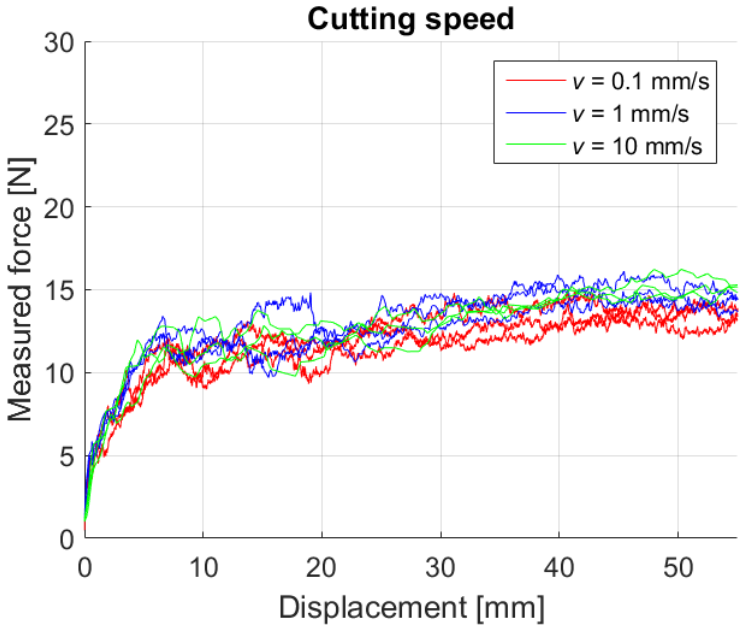

Figure 2.17: Results from the screening cutting tests for different cutting speeds presented in a force-displacement curve. The tests were performed on a sample of bending stiffness 150 mN, with a clamping distance of 50 mm, MD as the cutting direction and the knife angles $\alpha = 0°$ and $\beta = 0°$.

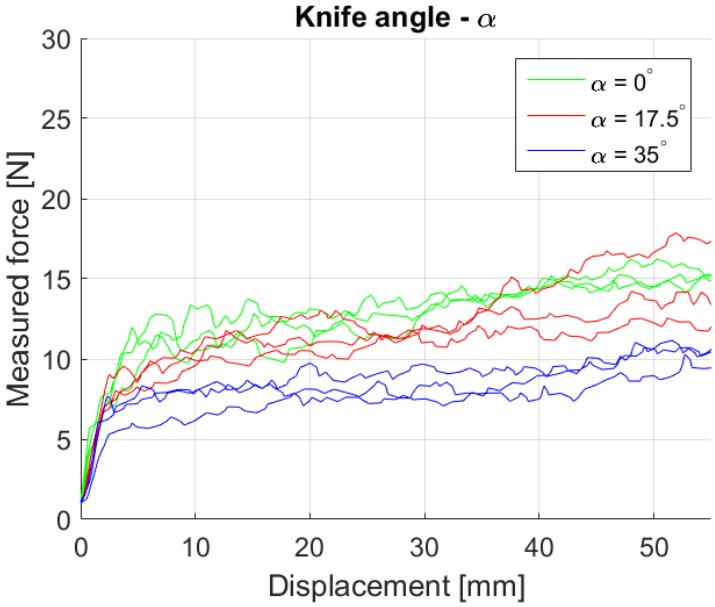

Figure 2.18: Results from the screening cutting tests for different knife angles α presented in a force-displacement curve. The tests were performed on a sample of bending stiffness 150 mN, with the cutting speed 10 mm/s, with a clamping distance of 50 mm, MD as the cutting direction and the knife angle $\beta = 0°$.

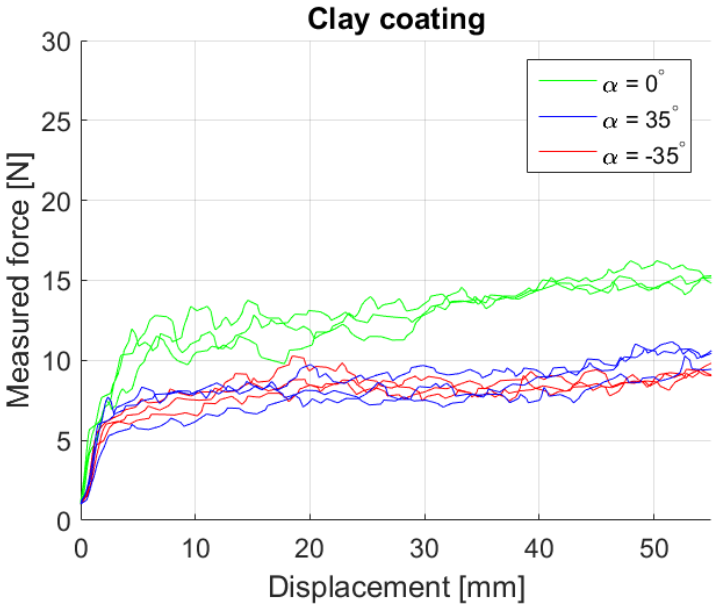

Figure 2.19: Results from the screening cutting tests where the cut is initiated on the clay coated side as well as on the non-clay coated side, presented in a force-displacement curve. The tests were performed on a sample of bending stiffness 150 mN, with the cutting speed 10 mm/s, with a clamping distance of 50 mm, MD as the cutting direction and the knife angle $\beta = 0°$.

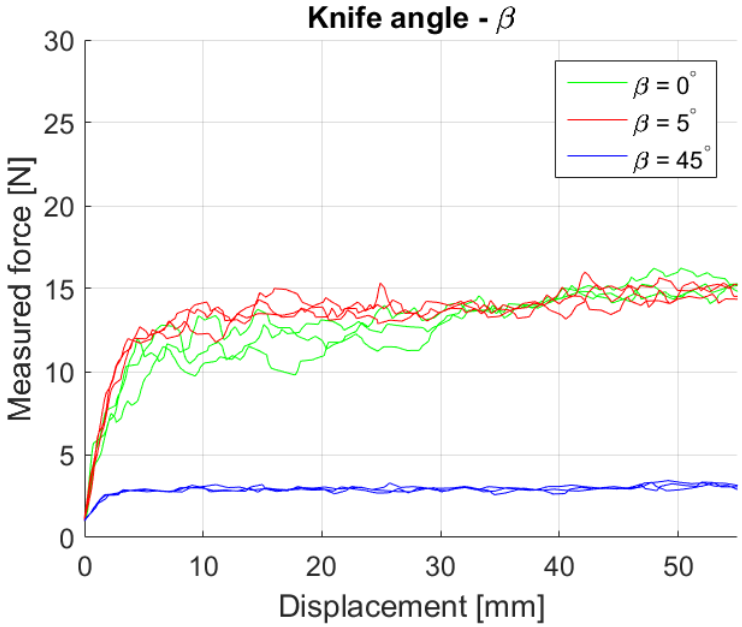

Figure 2.20: Results from the screening cutting tests for different knife angles β presented in a force-displacement curve. The tests were performed on a sample of bending stiffness 150 mN, with the cutting speed 10 mm/s, with a clamping distance of 50 mm, MD as the cutting direction and the knife angle $\alpha = 0°$.

The out-of-plane strain for each test setup, according to Table 2.3, were measured using a microscope. The results are presented in Table 2.4 below. Three tests were done for each test setup. The convention Test setup:Test number is therefore used in Table 2.4.

Table 2.4: Out-of-plane deformation.

Test	Out-of-plane strain	Test	Out-of-plane strain	Test	Out-of-plane strain
1:1	0.64	6:1	0.96	11:1	0.62
1:2	0.87	6:2	0.76	11:2	0.62
1:3	0.77	6:3	0.48	11:3	0.63
2:1	0.32	7:1	0.75	12:1	0.54
2:2	0.84	7:2	0.78	12:2	0.59
2:3	0.49	7:3	0.73	12:3	0.64
3:1	0.99	8:1	0.66	13:1	1.00
3:2	0.42	8:2	0.32	13:2	1.13
3:3	0.29	8:3	0.35	13:3	1.05
4:1	0.35	9:1	0.72	14:1	0.05
4:2	0.64	9:2	0.82	14:2	0.17
4:3	0.44	9:3	0.72	14:3	-
5:1	0.85	10:1	0.96		
5:2	0.59	10:2	0.92		
5:3	0.82	10:3	0.87		

Example pictures from the tomography analysis are presented in Figure 2.21 - 2.23. Further investigation of the results may be found in Section 2.3.2.

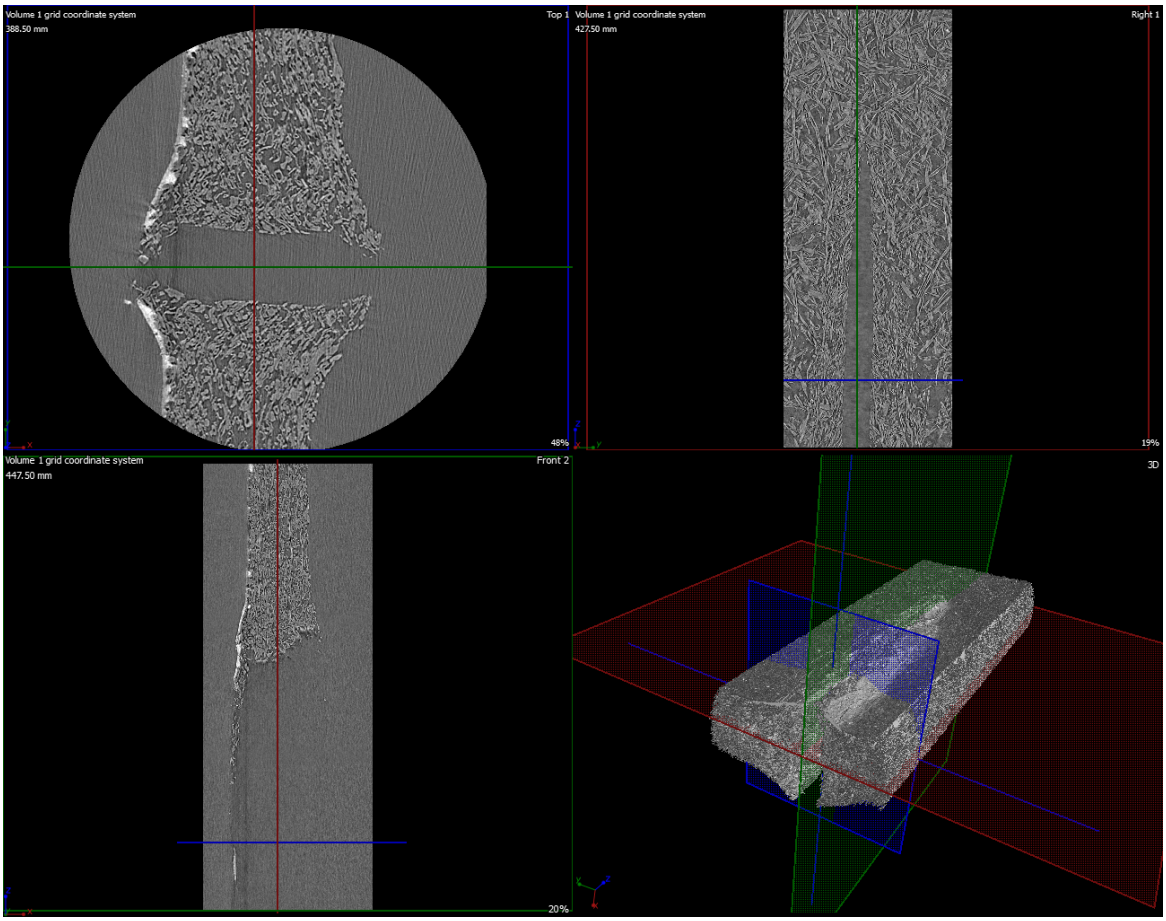

Figure 2.21: Tomographic pictures of the crack far away from the crack tip. The picture in the bottom right corner shows the different cross sections that are presented in the remaining three pictures. The evaluated paperboard sample has the bending stiffness 150 mN, was cut in MD with 10 mm/s and was clamped at a distance of 50 mm.

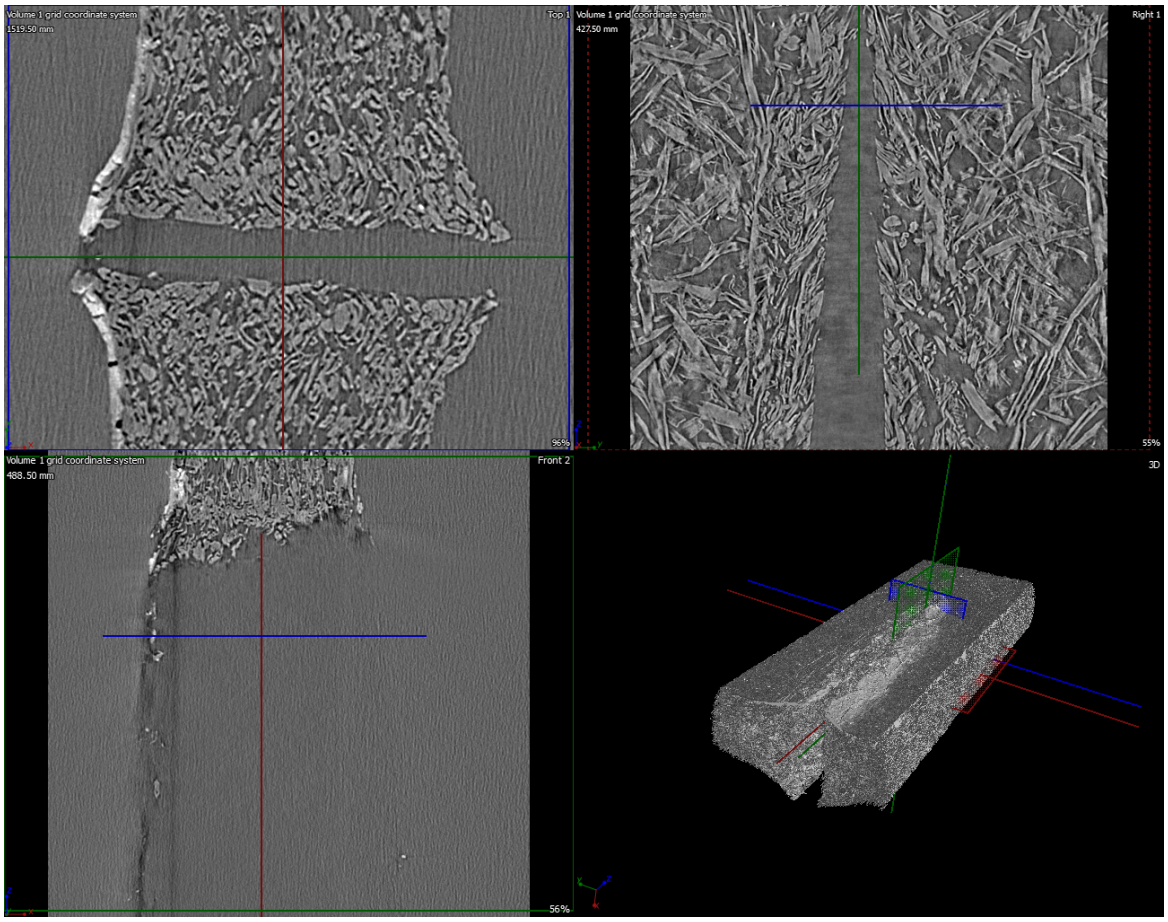

Figure 2.22: Tomographic pictures of the crack near the crack tip. The picture in the bottom right corner shows the different cross sections that are presented in the remaining three pictures. The evaluated paperboard sample has the bending stiffness 150 mN, was cut in MD with 10 mm/s and was clamped at a distance of 50 mm.

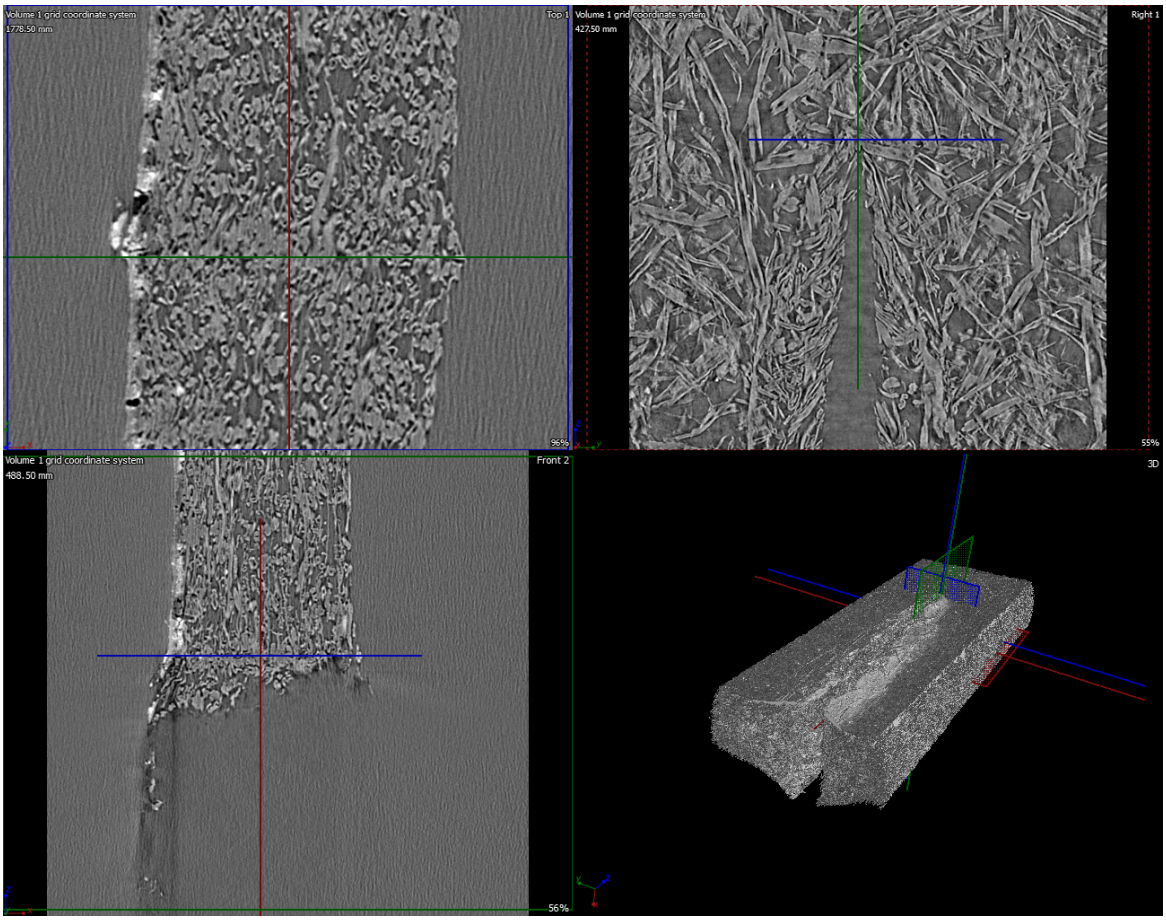

Figure 2.23: Tomographic pictures of the crack near the crack tip. The picture in the bottom right corner shows the different cross sections that are presented in the remaining three pictures. The evaluated paperboard sample has the bending stiffness 150 mN, was cut in MD with 10 mm/s and was clamped at a distance of 50 mm.

Beside the cutting force and the out-of-plane strain, another interesting observation was revealed during the screening experiments. Paperboard with low bending stiffness (30 mN) showed a wavelike behaviour, both in the cutting force and geometrically. This response is shown in Figure 2.24.

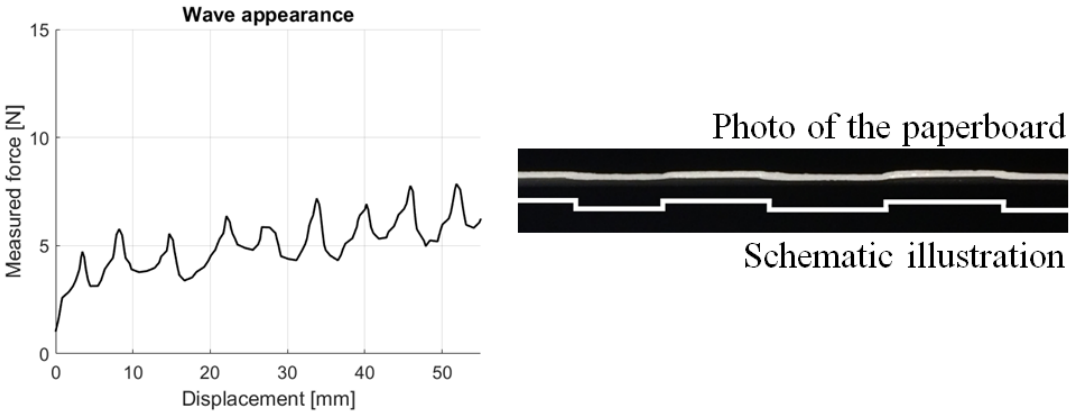

Figure 2.24: The wave appearance observed during cutting of weak paperboard, presented with a force-displacement curve (to the left) and geometrically illustrated (to the right).

Analysis

To be able to evaluate how the cutting parameters affect the measured force, some kind of statistical model is needed. By using regression analysis, one could find a model based on experimental data that gives a relation between a number of describing parameters and some kind of response [3]. The measured response Y^i can be expressed as a polonomial of order k, i.e.

$$Y^i = \alpha^i + \sum_{j=1}^{m} \beta_j^i \, x_j^i + \sum_{j=1}^{m} \sum_{l=1}^{m} \beta_{jl}^i \, x_j^i x_l^i + ... + \sum_{j=1}^{m} \sum_{l=1}^{m} ... \sum_{q=1}^{m} \beta_{jl...q}^i \, x_j^i x_l^i \, ... \, x_q^i + \gamma^i \quad (2.12)$$

where α^i is a constant and γ^i is a residual describing the model deviation in relation to the real response, all for each observed response $i = 1, 2, ..., n$, where n is the number of observations. For each observed response i, x_j^i denote the j^{th} describing variable and β_j^i is a (constant) term multiplier for $j = 1, 2, ..., m$, where m is the number of describing variables.

In order to determine the goodness of the regression model, one could examine the so called coefficient of determination R^2 [14]. This coefficient gives a percentage of how much of the response variable variation that can be explained by the predictor

variables in the model. R^2 is defined as

$$R^2 = 1 - \frac{\sum_{i=1}^{n}(y_i - \hat{y}_i)^2}{\sum_{i=1}^{n}(y_i - \bar{y}_i)^2} \tag{2.13}$$

where y_i is the observed response, $\hat{y}_i$ is the model fitted response and $\bar{y}_i$ is the mean response, all for each observation $i = 1, 2, ..., n$.

Furthermore, there exists different types of R^2, such as the adjusted R^2 and the predicted R^2. The R^2 value in (2.13) will increase as one add more predictors [14]. This can lead to that a model of more terms seems to be better only because of the high number of terms. The adjusted R^2 will adjust the number of predictors in order to help choosing a reliable model, which goodness is more based on significant predictors rather than the number of terms.

The predicted R^2 value indicates on how good the model predicts new observations [14]. This is done by removing one observation at the time and thereafter determining how good the estimated regression model predicts the removed observation.

All three, above mentioned, R^2 values were considered when choosing suitable regression models during this thesis.

During the statistical analysis of the cutting force measured during the screening experiments, the first step was to examine the response of every individual parameter. This was done by performing a regression analysis of the mean value of the cutting force measured in the displacement interval presented in Figure 2.25. Furthermore, the variance of the cutting force was examined in the same interval. A regression analysis was also performed of the measured out-of-plane strain.

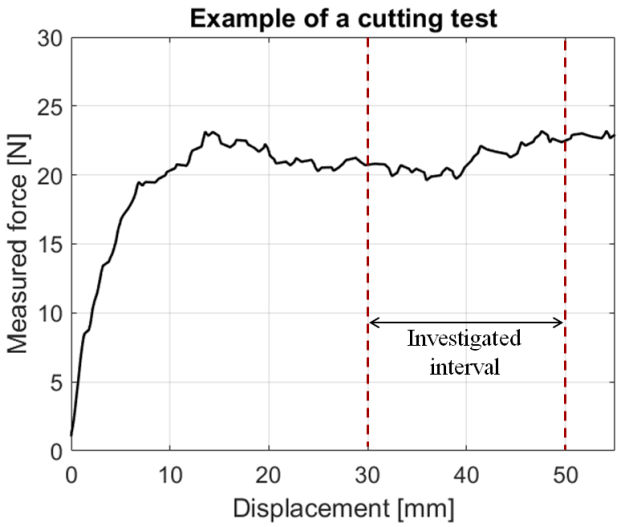

Figure 2.25: Example of force-displacement curve from a cutting test with the analysis interval marked.

From the regression results obtained, additional regression analyses of the measured responses where performed. Here, all parameters were limited to the order of influence derived in the first analysis part, considered. The regression method used was Stepwise - Forward selection, which means that the term with the most statistical significant improvement of the fit is added first, then the term with the second most statistical significant improvement is added and so on, until all terms that improves the fit 'enough' has been added. 'Enough' in this thesis was chosen as having a P-value greater than 0.1. The measured data used in the regression analysis can be seen in Appendix B and for a more thorough review of the statistical work, see Appendix C.

Next, the main effects of the parameters in the regression models, residual plots and the obtained regression equations are presented. The results regarding the measured force may be seen in Figure 2.26, 2.27 and (2.14) and the results regarding the out-of-plane strain may be seen in Figure 2.29, 2.30 and (2.16). Furthermore, the coefficients of determinations of the regression are also presented.

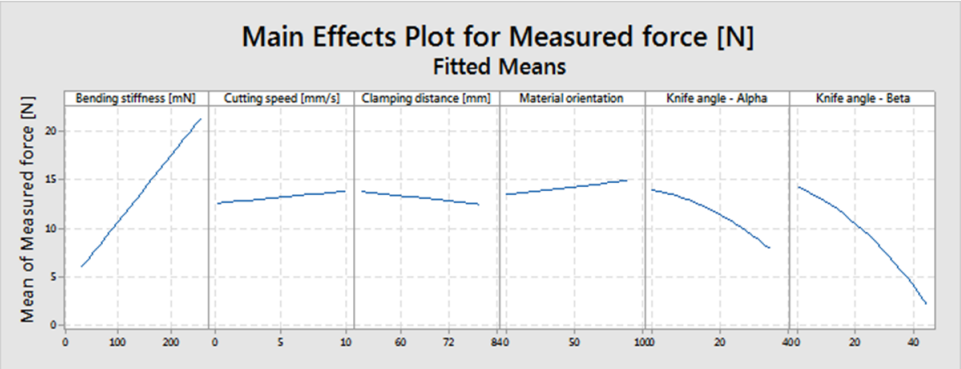

Figure 2.26: Main effect plot regarding the measured force.

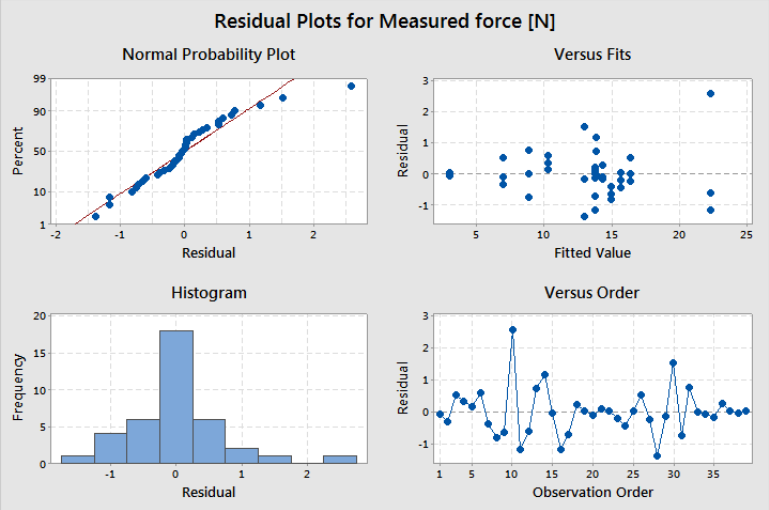

Figure 2.27: Residual plot regarding the measured force.

$$F_{fitted} = 5.8 + 6.7 \cdot 10^{-1} P_1 + 1.3 \cdot 10^{-1} P_2 - 4.2 \cdot 10^{-2} P_3 + 1.6 \cdot 10^{-2} P_4 - \\ -6.6 \cdot 10^{-1} P_5 - 3.1 \cdot 10^{-3} P_5^2 - 1.2 \cdot 10^{-1} P_6 - 3.3 \cdot 10^{-3} P_6^2 \tag{2.14}$$

where the parameters are denoted as follows

F_{fitted}	=	The fitted value of the cutting force	[N]
P_1	=	Material bending stiffness	[mN]
P_2	=	Cutting speed	[mm/s]
P_3	=	Clamping distance	[mm]
P_4	=	Material orientation	[° from MD]
P_5	=	Knife angle - α	[°]
P_6	=	Knife angle - β	[°]

$$R^2 = 97.56\,\% \qquad R^2_{adj} = 96.91\,\% \qquad R^2_{pred} = 95.57\,\%$$

From the results presented, one may note that there are some parameters having greater influence on the cutting force than others. It may also be seen that some parameters are not favourable to vary since variation yields unstable results. For example if cutting speed, clamping distance and material orientation are excluded from the model, a more neat regression equation is obtained, still with satisfying coefficients of determination, see (2.15). Since the statistical software however included these terms in the regression, they are present in the previous presented results.

$$\begin{aligned} F_{fitted} = 4.9 + 6.6 \cdot 10^{-2}\, P_1 - 5.1 \cdot 10^{-2}\, P_5 - 3.4 \cdot 10^{-3}\, P_5^2 - \\ -8.1 \cdot 10^{-2}\, P_6 - 4.1 \cdot 10^{-3}\, P_6^2 \end{aligned} \tag{2.15}$$

$$R^2 = 95.17\,\% \qquad R^2_{adj} = 94.44\,\% \qquad R^2_{pred} = 93.51\,\%$$

In Table 2.5 the different parameters' influence may be seen. This table formed a large part of the basis for the reduction of the parameter space, will are presented later on, see Table 2.6.

Table 2.5: Parameter impact on cutting force

Parameter	Big impact	Increased variation	Should be varied
Material bending stiffness	Yes	No	Yes
Cutting speed	No	No	No
Clamping distance	No	Yes	No
Material orientation	No	No	Yes
Knife angle - α	Yes	No	Yes
Knife angle - β	Yes	No	Yes
Clay coating	No	No	No

If the results in Figure 2.14 - 2.20 are more closely examined, it can be found that the force increases initially and thereafter reaches a more steady force level. This initial force ramp can be explained by the increasing normal surface contact between the knife and the cut paperboard surfaces during the initial knife penetration. Thus, this normal interaction between the already cut paperboard surfaces and the knife seems to have a greater impact than the contact interaction in the crack tip.

Moreover, an increase of knife angle α leads to a decrease of measured force, which can be studied in Figure 2.18. This can be explained by a decrease of the knife interaction angle, which makes the knife act sharper. This is schematically illustrated in Figure 2.28.

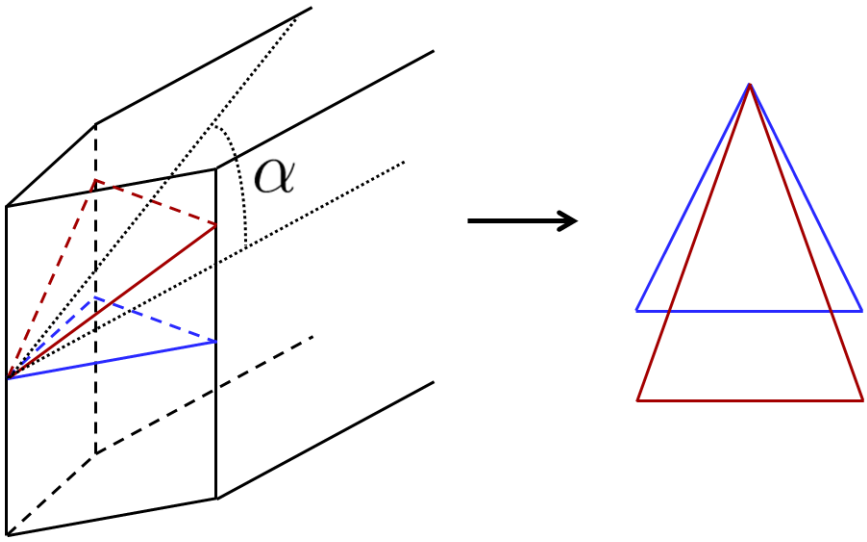

Figure 2.28: A change of knife angle α makes the knife act sharper, which can be proven by comparing the top angles of the two triangles. The top angle of the red triangle is clearly smaller than the top angle of the blue triangle ($\alpha = 0$).

Next follows the analysis of the out-of-plane deformation. The results are presented in the same way as for the cutting force. The measured data used in the regression analysis can be seen in Appendix B and for a more thorough review of the statistical work, see Appendix C.

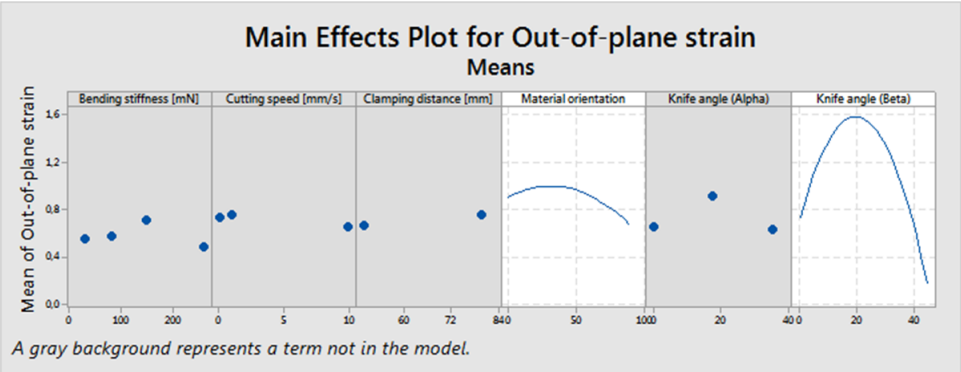

Figure 2.29: Main effect plot regarding the measured out-of-plane strain.

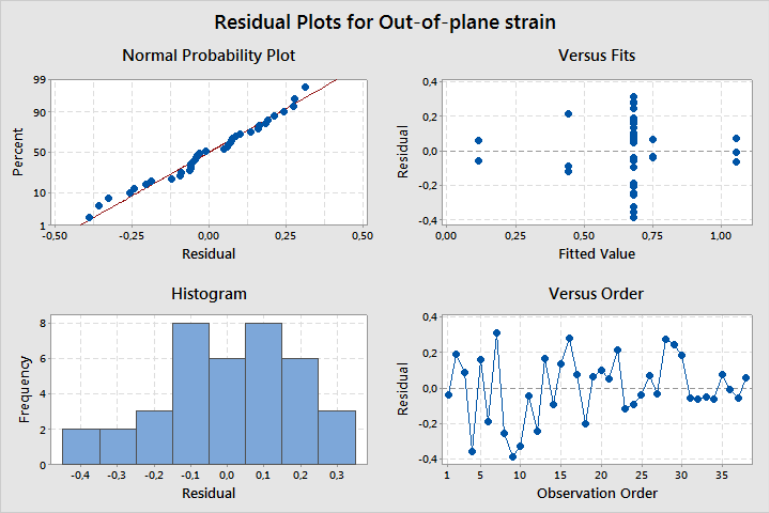

Figure 2.30: Residual plot regarding the measured out-of-plane strain.

$$\varepsilon_{fitted} = 6.8 \cdot 10^{-1} + 8.7 \cdot 10^{-2}\, P_1 - 2.2 \cdot 10^{-3}\, P_1^2 + 5.9 \cdot 10^{-3}\, P_2 - 9.5 \cdot 10^{-5}\, P_2^2 \tag{2.16}$$

where the parameters are denoted as follows

ε_{fitted}	=	The fitted value of the out-of-plane strain	[-]
P_1	=	Knife angle - β	[°]
P_2	=	Material orientation	[° from MD]

$$R^2 = 51.29\,\% \qquad R^2_{adj} = 45.39\,\% \qquad R^2_{pred} = 42.60\,\%$$

If the out-of-plane deformation results are studied, it may be seen that there are just two of the considered parameters that have a significant impact on the deformation. The R^2-values also indicate that the fit is not as good as desired which indicates that there are effects not captured by the statistical model. After considering the measuring technique of the deformation, some possible sources of errors were found. Firstly, the specimens may have been deformed during the storage between the test and the measurements, since the equipment was located at different places. Secondly, the measuring was performed locally and not along the entire cutting path, this leaves room for measuring variance, which in this case is not possible to capture.

The great dependence on just a few parameters, mainly the dependence on the knife angle β, enabled a simple investigation of the phenomenon that probably causes the significant out-of-plane deformation. Figure 2.31 shows a scaled-down free body diagram and a deformation image of a '$\beta = 0°$' and a '$\beta = 45°$' cut focusing on the impact on the out-of-plane deformation.

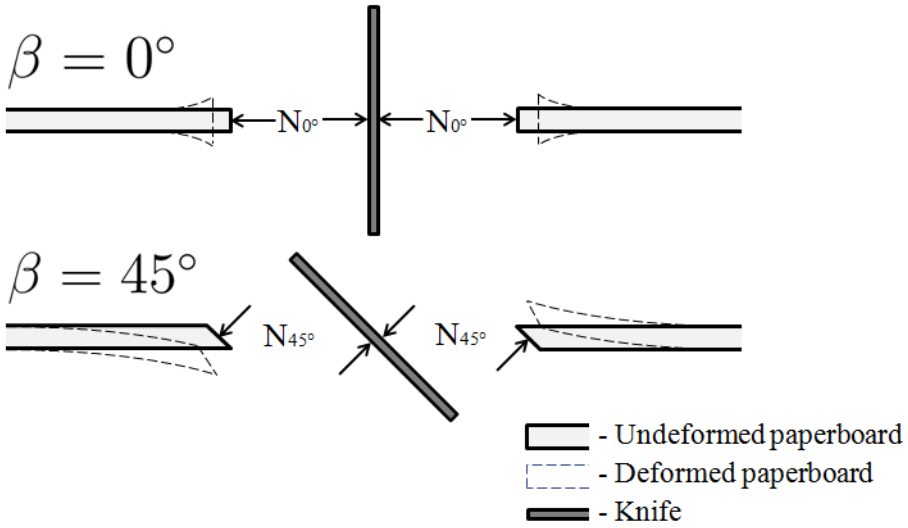

Figure 2.31: Free body diagram and a illustration of the defomration image of a '$\beta = 0°$' and a '$\beta = 45°$' cut.

The fibre based paperboard structure is often referred to as relatively weak in compression, since the fibres are able to buckle locally [25]. In comparison with bending, the force needed to buckle the paperboard is much greater. Thus, if the free-body diagram is studied it may be understood that the compressive load at the cut surface of the paperboard decreases with increased β.

The underlying phenomenon of the out-of-plane deformation, could be explained by local fibre buckling, due to the compressive load that arises during a cut with a more upright blade. This hypothesis was later strengthened since it seemed to exist a critical value of β, where a great increase in the deformation occurred. This is in accordance with buckling theory where buckling occurs at a critical load [20]. The observations from the tomographic analysis also strengthen the theory of fibre buckling, since a small densified region was present close to the crack path. In this region the fibres were deformed and buckled.

The tomography response also showed that the effect on the paperboard was very local, i.e. the process region is very small compared to the crack length and sample size. It was also seen that the cut surface was very fine with almost no fuss at all. The out-of-plane deformation was also clearly seen in the tomographic pictures.

The measuring inconsistency and the probable physical description of the out-of-plane strain according to Figure 2.31, contributed to the decision to not investigate this out-of-plane response further in the final experiments.

As previously presented, the paperboard samples of low bending stiffness showed a wavelike behaviour when cut. This proved to be an effect of difficulties to get the weak paperboard properly clamped. This resulted in the paperboard buckling back and forth, with force peaks and geometrical folds in the transitions as a consequence. Since this was assumed to be an imperfection in the test setup, it is not further investigated in this thesis.

2.3.3 Final experiments

The purpose of the final experiments was to further investigate how the parameters that passed the screening affect the cut. As previously mentioned, the parameter reduction, shown in Table 2.6, enabled a comprehensive test plan, which may be found in Table 2.7.

Table 2.6: Reduction of the parameter space

Parameter	Number of test points before reduction	Number of test points after reduction
Material bending stiffness	4	2
Cutting speed	3	1
Material direction	3	2
Clamping distance	2	1
Clay coating	2	1
Knife angle - α	3	3
Knife angle - β	3	3
Available combinations	1 296	36
Number of tests	-	5
Total number of tests	-	180

Table 2.7: Test plan for the Final experiments tests.

#	Number of tests	Bending stiffness [mN]	Material orientation	Knife angle - α [°]	Knife angle - β [°]	#	Number of tests	Bending stiffness [mN]	Material orientation	Knife angle - α [°]	Knife angle - β [°]
1	5	80	MD	0	0	19	5	80	CD	17.5	22.5
2	5	260	MD	0	0	20	5	260	CD	17.5	22.5
3	5	80	CD	0	0	21	5	80	MD	0	22.5
4	5	260	CD	0	0	22	5	260	MD	0	22.5
5	5	80	MD	17.5	0	23	5	80	CD	0	22.5
6	5	260	MD	17.5	0	24	5	260	CD	0	22.5
7	5	80	CD	17.5	0	25	5	80	MD	0	45
8	5	260	CD	17.5	0	26	5	260	MD	0	45
9	5	80	MD	30	0	27	5	80	CD	0	45
10	5	260	MD	30	0	28	5	260	CD	0	45
11	5	80	CD	30	0	29	5	80	MD	17.5	45
12	5	260	CD	30	0	30	5	260	MD	17.5	45
13	5	80	MD	30	22.5	31	5	80	CD	17.5	45
14	5	260	MD	30	22.5	32	5	260	CD	17.5	45
15	5	80	CD	30	22.5	33	5	80	MD	30	45
16	5	260	CD	30	22.5	34	5	260	MD	30	45
17	5	80	MD	17.5	22.5	35	5	80	CD	30	45
18	5	260	MD	17.5	22.5	36	5	260	CD	30	45

Results

The results from the final experiments are presented in Appendix D, in terms of force-displacement diagrams. The parameter data for each test setup can be found in Table 2.7 above.

Analysis

Before evaluating the connection between the measured force and the predictor variables in a regression analysis, a mean value of the measured force was computed for all 36 feasible combinations in Table 2.7. This mean force was computed for the same displacement interval that is shown in Figure 2.25. Since the tests, according to Table 2.7, consist of combinations of different settings for the four different parameters, only a full parameter regression analysis was done. The method used for the regression analysis was 'Stepwise' where a parameter requirement of a P-value above 0.1 was set for entering the model but also to stay in the model. The measured data used in the regression analysis can be seen in Appendix E.

The fitted regression model can be found in (2.17) below and the following presented results show the accuracy of the fitted model and the main parameter effects. Furthermore, the coefficients of determination of the regression are also presented.

$$\begin{aligned} F_{fitted} = 6.3 &+ 7.3 \cdot 10^{-2}\, P_1 - 2.5 \cdot 10^{-1}\, P_2 - 3.5 \cdot 10^{-3}\, P_1 P_2 - \\ &-5.9 \cdot 10^{-4}\, P_1 P_3 + 3.2 \cdot 10^{-3}\, P_2^2 + 1.6 \cdot 10^{-5}\, P_1 P_2 P_3 - \\ &-2.0 \cdot 10^{-6}\, P_1 P_2 P_4 + 4.7 \cdot 10^{-5}\, P_1 P_2^2 + 1.0 \cdot 10^{-6}\, P_1 P_4^2 \end{aligned} \tag{2.17}$$

where the parameters are denoted as follows

F_{fitted}	=	The fitted value of the cutting force	[N]
P_1	=	Material bending stiffness	[mN]
P_2	=	Knife angle - β	[°]
P_3	=	Knife angle - α	[°]
P_4	=	Material orientation	[° from MD]

$$R^2 = 99.31\,\% \qquad R^2_{adj} = 99.07\,\% \qquad R^2_{pred} = 98.59\,\%$$

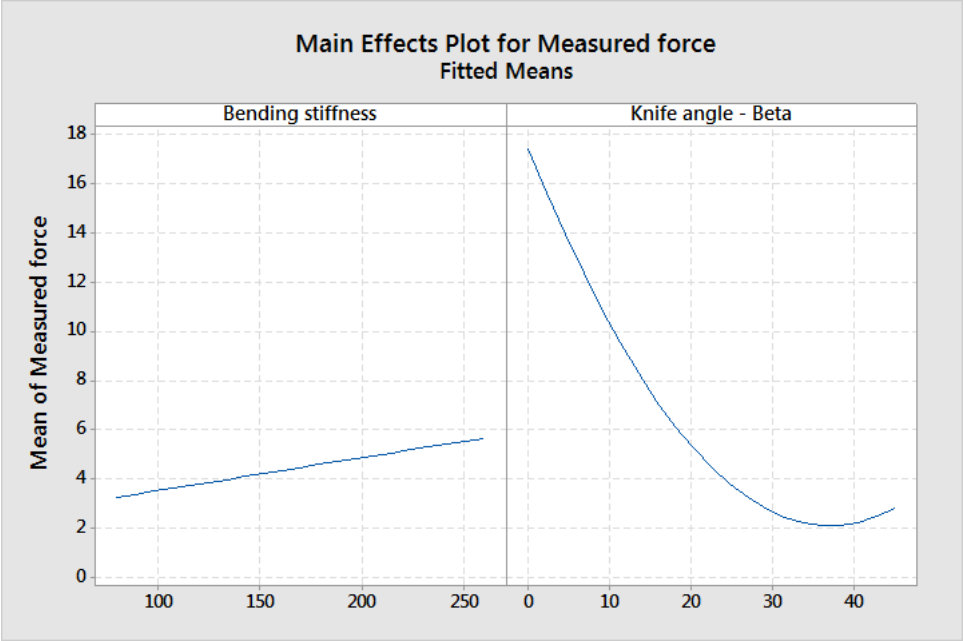

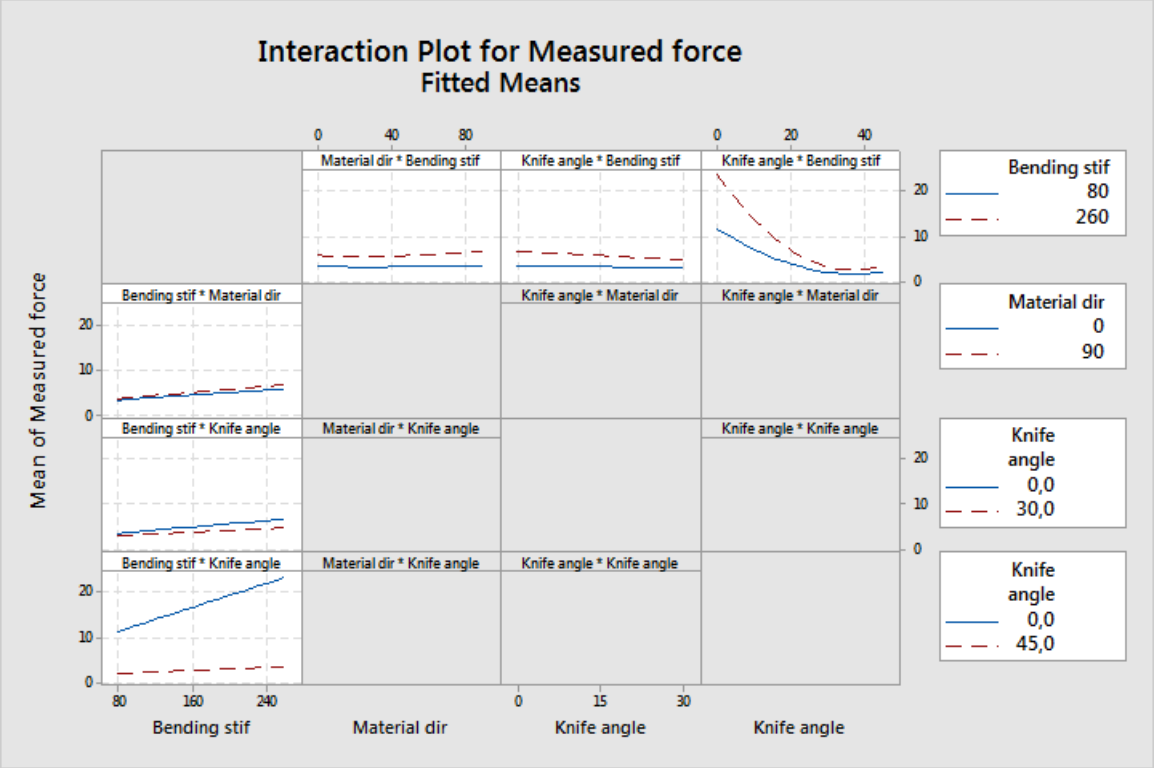

Figure 2.32: Main effect plot regarding the measured force.

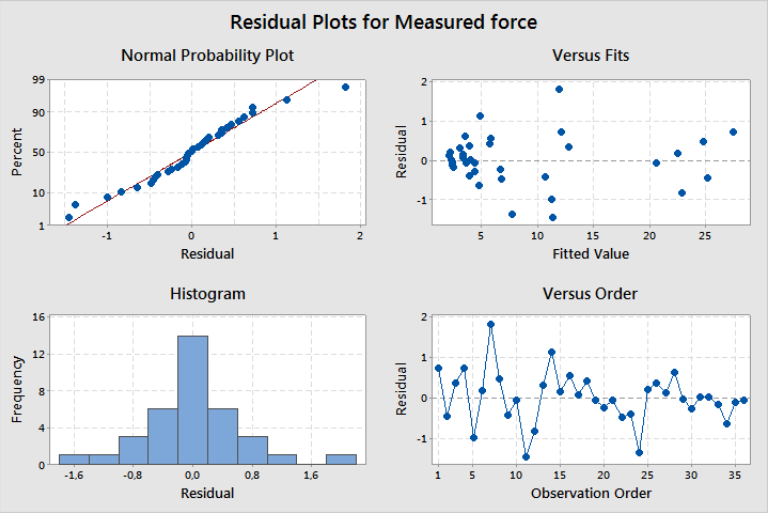

Figure 2.33: Residual plot regarding the measured force.

When the main effect plots are studied it may be seen that the bending stiffness and the knife angle β are the parameters that have the largest impact on the cutting force. These parameters seem to be able to change the contact force regardless of other parameters, this is also shown in Figure 2.32.

Figure 2.32 also shows an interesting interaction between the bending stiffness and the knife angle β. For low knife angles ($\beta = 0°$), the bending stiffness has a large impact on the measured force and for larger knife angles ($\beta = 45°$), the impact is very small. At first glance this may be very surprising and an increase in force for increased knife angle β would seem more intuitive, since the contact region increases with a factor $1/\cos\beta$. If the free body diagram presented in Figure 2.34 is considered, a possible explanation can be found.

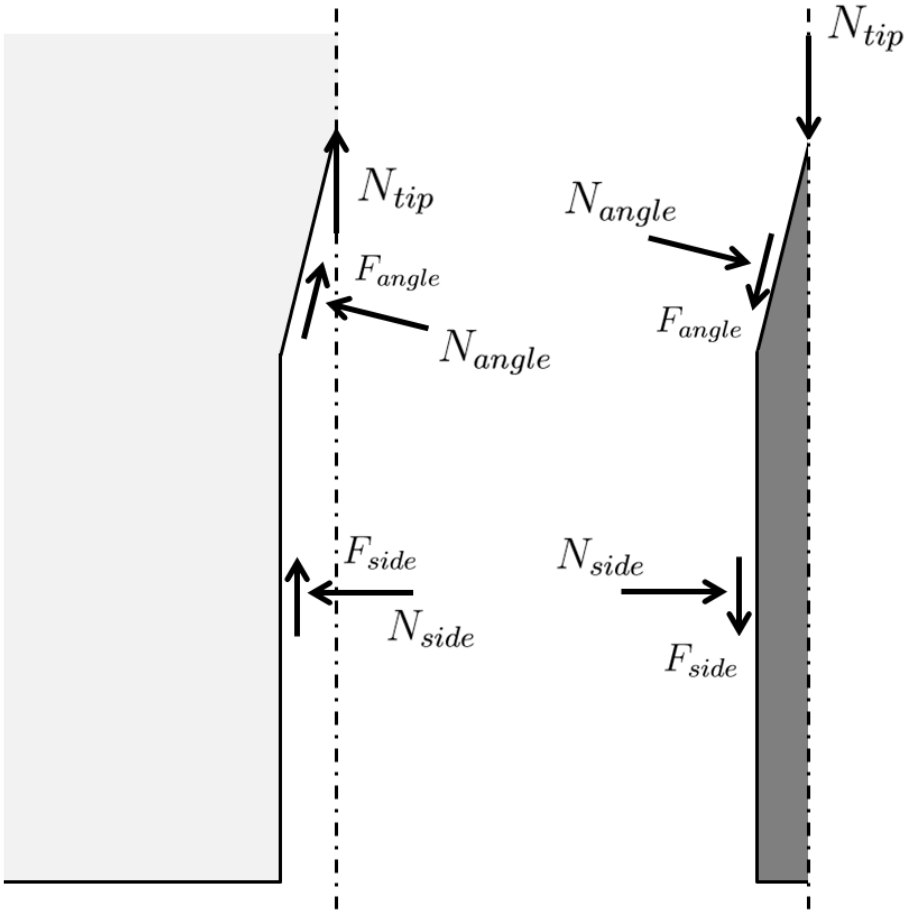

Figure 2.34: A schematic free body diagram showing the forces acting on the paperboard sample (to the left) and the knife (to the right) during cutting. Forces denoted N are normal forces and forces denoted F are frictional forces.

Cuts with small cutting angles β contribute to a local out-of-plane deformation, whereas a cut with a bigger cutting angle β yields an out-of-plane bending on a larger scale, all according to Figure 2.31. Considering Figure 2.34, the local out-of-plane deformation is a consequence of high normal contact forces N_{side} and N_{angle} compressing the paperboard, and contributing to buckling on fibre level. With increased β, the in-plane normal forces decrease and at a certain angle the force reaches a critical value, where buckling effects on a microscopic level are replaced by bending effects on a macroscopic level. This yields a smaller local out-of-plane deformation. Since paperboard is relatively weak in out-of-plane bending compared to in-plane compression, the normal forces N_{side} and N_{angle} are greatly decreased. A decrease in the normal forces acting on the cut surfaces does also mean a decrease in friction counteracting the knife movement. Thus, the force required to penetrate the paperboard sample is decreased. The palpable

decrease of the measured force in Figure 2.20 indicates that the friction forces have a greater influence on the measured force than the force N_{tip} needed to "split" the material.

If the main effect plots from the final tests are compared with the ones obtained from the screening tests, some differences may be found. The impact of knife angle β differs and if the results from the different studies are combined it may be found that the measured force is more or less the same for low values of β (0° and 5°). The same effect yields for higher values (22.5° and 45°). This could indicate the existence of a critical value, or an interval, of β where the cutting force is greatly changed. This would be in accordance with the earlier discussion about fibre buckling in Section 2.3.2. The earlier presented main effect plots showing the measured force's dependence of knife angle beta are presented in Figure 2.35 together with a more probable, but still hypothetical, main effect based on the earlier discussions.

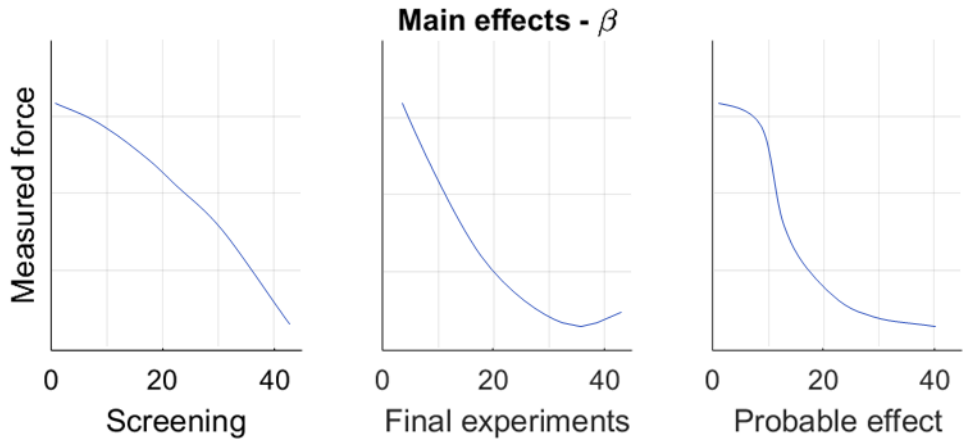

Figure 2.35: Earlier presented fitted main effect plots showing the measured force's dependence of knife angle β together with a more probable main effect.

2.4 Summary of performed measurements

The measurements contributed to a greatly increased knowledge within paperboard physics and laid a good foundation for further development. Several of the responses observed during the measurements were of importance when designing the virtual cutting model. These observations are listed together with a short description of why they were important.

- **Process region -** The tomography analysis showed that the process region is very small compared to the crack length and sample size, which should be taken into account when choosing fracture modelling approach. Information about this can be found further ahead in Section 4.1.

- **Increasing cutting force at the beginning of the measurements and great dependence of β -** In accordance with earlier hypotheses, these two observations are likely to indicate that the cutting force is mainly effected by geometrical effects (macroscale), rather than actual rupture of specific fibres (microscale).

- **Out-of-plane deformation -** Is of interest to capture in the model. Out-of-plane Poisson's ratio is in earlier work often set to be zero. This should be investigated further in order to see if it is possible to affect the out-of-plane deformation, by just changing this material property.

- **Dependence of α -** Is of interest to capture in the model. This may be solved geometrically since a greater value of α makes the knife appear sharper.

- **Dependence of material direction -** Is of interest to capture in the model. Can probably be captured, since the elastic modulus is greater in MD than in CD. This will make the contact forces, illustrated in Figure 2.31, greater for a cut in CD, increasing the friction and also thereby the cutting force. Note that an overestimation of the force needed to actually make the crack propagate, yields the reversed effect.

Chapter 3

Constitutive modelling

3.1 In-plane orthotropic linear elasticity

When modelling and trying to understand the behaviour of a material, it is of great importance to be able to describe its physical characteristics properly. A connection between the arisen stress and strain, when exposed to some kind of external mechanical loading, is needed.

The stress σ in a material that is subjected to uni-axial tension is during elastic deformation uniquely related to the elastic strain ε^e by the Hooke's law, i.e.

$$\varepsilon^e = \frac{1}{E}\,\sigma \tag{3.1}$$

where E is Young's modulus. For a more general load case, (3.1) can be expanded to

$$[\boldsymbol{\varepsilon}] = \begin{bmatrix} \varepsilon^e_{11} \\ \varepsilon^e_{22} \\ \varepsilon^e_{33} \\ 2\,\varepsilon^e_{12} \\ 2\,\varepsilon^e_{13} \\ 2\,\varepsilon^e_{23} \end{bmatrix} = \begin{bmatrix} C_{1111} & C_{1122} & C_{1133} & C_{1112} & C_{1113} & C_{1123} \\ C_{2211} & C_{2222} & C_{2233} & C_{2212} & C_{2213} & C_{2223} \\ C_{3311} & C_{3322} & C_{3333} & C_{3312} & C_{3313} & C_{3323} \\ C_{1211} & C_{1222} & C_{1233} & C_{1212} & C_{1213} & C_{1223} \\ C_{1311} & C_{1322} & C_{1333} & C_{1312} & C_{1313} & C_{1323} \\ C_{2311} & C_{2322} & C_{2333} & C_{2312} & C_{2313} & C_{2323} \end{bmatrix} \begin{bmatrix} \sigma_{11} \\ \sigma_{22} \\ \sigma_{33} \\ \sigma_{12} \\ \sigma_{13} \\ \sigma_{23} \end{bmatrix} = [\mathbb{C}]\,[\boldsymbol{\sigma}] \tag{3.2}$$

where $\mathbb{C}$ is called the linear elastic flexibility tensor and 1, 2, 3 denote three mutually-orthogonal material directions. When considering an assumed orthotropic material,

such as paperboard (1=MD, 2=CD and 3=ZD), (3.2) gets the following format

$$[\boldsymbol{\varepsilon}] = \begin{bmatrix} \varepsilon^e_{11} \\ \varepsilon^e_{22} \\ \varepsilon^e_{33} \\ 2\,\varepsilon^e_{12} \\ 2\,\varepsilon^e_{13} \\ 2\,\varepsilon^e_{23} \end{bmatrix} = \begin{bmatrix} \frac{1}{E_1} & -\frac{\nu_{21}}{E_2} & -\frac{\nu_{31}}{E_3} & 0 & 0 & 0 \\ -\frac{\nu_{12}}{E_1} & \frac{1}{E_2} & -\frac{\nu_{32}}{E_3} & 0 & 0 & 0 \\ -\frac{\nu_{13}}{E_1} & -\frac{\nu_{23}}{E_2} & \frac{1}{E_3} & 0 & 0 & 0 \\ 0 & 0 & 0 & \frac{1}{G_{12}} & 0 & 0 \\ 0 & 0 & 0 & 0 & \frac{1}{G_{13}} & 0 \\ 0 & 0 & 0 & 0 & 0 & \frac{1}{G_{23}} \end{bmatrix} \begin{bmatrix} \sigma_{11} \\ \sigma_{22} \\ \sigma_{33} \\ \sigma_{12} \\ \sigma_{13} \\ \sigma_{23} \end{bmatrix} \tag{3.3}$$

where ν_{ij} are Poisson's ratios, G_{ij} denote the shear moduli for i, j = 1, 2, 3.

Recall the symmetry of the flexibility matrix from (2.2), i.e.

$$\frac{\nu_{12}}{E_1} = \frac{\nu_{21}}{E_2}; \quad \frac{\nu_{13}}{E_1} = \frac{\nu_{31}}{E_3}; \quad \frac{\nu_{23}}{E_2} = \frac{\nu_{32}}{E_3}$$

By adopting plane stress conditions, (3.3) can be reduced further. Plane stress conditions generally mean that $\varepsilon^e_{33} = -\frac{\nu_{13}}{E_1}\sigma_{11} - \frac{\nu_{23}}{E_2}\sigma_{22} \neq 0$, but the out-of-plane Poisson's ratios are assumed to be $\nu_{13} = \nu_{23} = 0$ [22]. This results in $\varepsilon^e_{33} = 0$. The expression in (3.3) can now be reduced to

$$[\boldsymbol{\varepsilon}] = \begin{bmatrix} \varepsilon^e_{11} \\ \varepsilon^e_{22} \\ 2\,\varepsilon^e_{12} \end{bmatrix} = \begin{bmatrix} \frac{1}{E_1} & -\frac{\nu_{21}}{E_2} & 0 \\ -\frac{\nu_{12}}{E_1} & \frac{1}{E_2} & 0 \\ 0 & 0 & \frac{1}{G_{12}} \end{bmatrix} \begin{bmatrix} \sigma_{11} \\ \sigma_{22} \\ \sigma_{12} \end{bmatrix} \tag{3.4}$$

The relation between stress and strain can also be described the inverse way, i.e. $\boldsymbol{\sigma} = \boldsymbol{D}\boldsymbol{\varepsilon}$. The in-plane stiffness matrix $\boldsymbol{D}$ yields

$$\boldsymbol{D} = \boldsymbol{C}^{-1} = \frac{1}{1 - \nu_{12}\nu_{21}} \begin{bmatrix} E_1 & \nu_{21}E_1 & 0 \\ \nu_{12}E_2 & E_2 & 0 \\ 0 & 0 & G_{12}(1 - \nu_{12}\nu_{21}) \end{bmatrix} \tag{3.5}$$

3.2 Plasticity

The relations in (3.1) - (3.4) are, as previously mentioned, only valid during elastic loading, more specific when $\sigma < \sigma_y$, where σ_y is the current yield stress. Above this threshold value, plastic deformations will be introduced in the material, which will increase the yield stress to $\sigma_y > \sigma_{y0}$, where σ_{y0} is called the initial yield stress. When

entering the plastic domain, there is no longer any obvious relation between stress and strain. To be able to handle this difficulty, it is convenient to use a more general expression for the strain tensor. By assuming small deformations, the strain tensor can be expressed as

$$\boldsymbol{\varepsilon} = \boldsymbol{\varepsilon}^e + \boldsymbol{\varepsilon}^p \tag{3.6}$$

where ε^e and ε^p answer to the elastic and the plastic strains, respectively. This phenomenon is illustrated for an inelastic material in Figure 3.1 below.

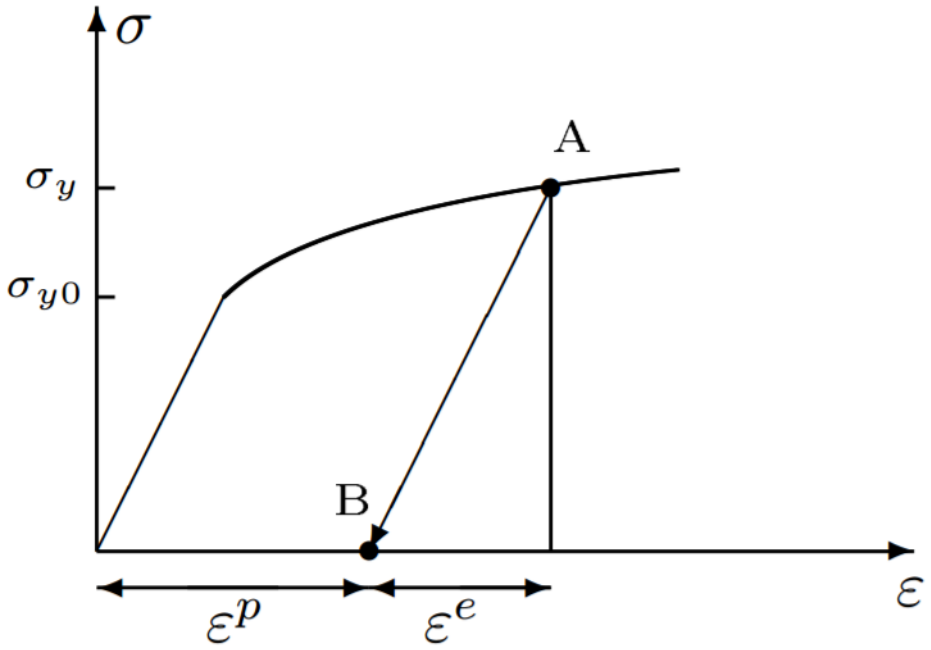

Figure 3.1: Loading of an inelastic material into the plastic region to point A. The material is thereafter unloaded, elastically, to point B, where now plastic strains are present in the material [4].

Furthermore, the strain rate tensor is obtained by differentiating (3.6) with respect to time, i.e.

$$\dot{\boldsymbol{\varepsilon}} = \dot{\boldsymbol{\varepsilon}}^e + \dot{\boldsymbol{\varepsilon}}^p \tag{3.7}$$

The linear elastic stress rate can be expressed as

$$\dot{\boldsymbol{\sigma}} = \mathbb{D} : (\dot{\boldsymbol{\varepsilon}} - \dot{\boldsymbol{\varepsilon}}^p) \tag{3.8}$$

In order to describe the initiation of plasticity, a yield function f is introduced

$$f = f(\boldsymbol{\sigma}, K_\alpha) \tag{3.9}$$

where $\boldsymbol{\sigma}$ is the stress tensor and K_α for $\alpha = 1, 2, ...$ are hardening parameters describing the evolution of the yield surface, i.e.

$$\sigma_y(\kappa_\beta) = \sigma_{y0} + K_\alpha(\kappa_\beta) \tag{3.10}$$

where κ_β for $\beta = 1, 2, ...$ are internal state variables that characterise the state of the assumed elasto-plastic material [19]. The yield function f is defined such that

$$f \begin{cases} = 0 \text{ during development of plasticity} \\ < 0 \text{ elastic behaviour} \end{cases} \tag{3.11}$$

and is a convex function in the stress space.

Since the internal variables κ_α are in some sense describing the plasticity history, they are initially zero.

The anisotropic material is assumed to be time independent, which implies that the consistency condition has to be satisfied, i.e.

$$\dot{f} = \frac{\partial f}{\partial \boldsymbol{\sigma}} : \dot{\boldsymbol{\sigma}} + \frac{\partial f}{\partial K_\alpha} \dot{K}_\alpha = 0 \tag{3.12}$$

where

$$\dot{K}_\alpha = \frac{\partial K_\alpha}{\partial \kappa_\beta} \dot{\kappa}_\beta \tag{3.13}$$

As previously mentioned, the internal state variables κ_α are describing the plasticity history and can therefore only change during plastic loading. This implies that

$$\dot{\kappa}_\alpha = 0 \;\; \Rightarrow \;\; \dot{K}_\alpha = 0 \qquad \text{during elastic loading} \tag{3.14}$$

The stress rate tensor $\dot{\boldsymbol{\sigma}}$ in equation can be expressed by Hooke's law, i.e. Isotropic hardening was adopted in order to simplify the constitutive model, i.e. $K = K(\kappa)$. This implies that the position and shape of the yield surface will remain fixed and its evolution is directionally independent [19].

To be able to describe how the yield surface progresses in the stress space, some kind of evolution law is required. Here, the plastic strain rate tensor $\dot{\boldsymbol{\varepsilon}}^p$ is expressed as

$$\dot{\boldsymbol{\varepsilon}}^p = \dot{\lambda} \frac{\partial g}{\partial \boldsymbol{\sigma}} \tag{3.15}$$

where $g = g(\boldsymbol{\sigma}, K)$ is an arbitrary convex potential function and $\dot{\lambda}$ is a plastic multiplier. The potential function g is a function of the same variables as the yield function f and by choosing associated plasticity, i.e. $g = f$, the laws of thermodynamics are proven to be satisfied [19].

The evolution law for the internal state variable will be defined in term of the plastic multiplier as

$$\dot{\kappa} = \dot{\lambda} k(\boldsymbol{\sigma}, K) \tag{3.16}$$

where $k(\boldsymbol{\sigma}, K)$ denotes some function that has to be chosen based on experimental evidence or by other assumptions. Here strain hardening is assumed, which means that $\kappa = \varepsilon^p_{eff}$ or $\dot{\kappa} = \dot{\varepsilon}^p_{eff}$, where ε^p_{eff} is the plastic effective strain.

Furthermore, the plastic multiplier $\dot{\lambda}$ is defined as

$$\dot{\lambda} = \Big(\frac{2}{3}\dot{\boldsymbol{\varepsilon}}^p \dot{\boldsymbol{\varepsilon}}^p\Big)^{1/2} = \dot{\boldsymbol{\varepsilon}}^p_{eff} \tag{3.17}$$

If (3.16) and (3.17) are compared, one find that $k = 1$, more specific

$$\dot{\kappa} = \dot{\lambda} \tag{3.18}$$

The consistency relation in (3.12) can be rewritten by using the relations in (3.13) and (3.16)

$$\frac{\partial f}{\partial \boldsymbol{\sigma}} : \dot{\boldsymbol{\sigma}} - H\dot{\lambda} = 0 \tag{3.19}$$

where the plastic modulus H is defined as

$$H = -\frac{\partial f}{\partial K}\frac{\partial K}{\partial \kappa}k = -\frac{\partial f}{\partial K}\frac{\partial K}{\partial \kappa} \tag{3.20}$$

for $k = 1$.

In order to find an elasto-plastic relation between the stresses and strains, a choice of yield criterion describing the function f is required.

3.2.1 Hill's yield criterion

Hill's yield criterion was used to describe the plasticity on a macroscopic scale in this thesis. Hill's yield criterion can be formulated in the following manner

$$f(\boldsymbol{\sigma}, K) = (\sigma_{y0}^2\, \boldsymbol{s} : \mathbb{P} : \boldsymbol{s})^{\frac{1}{2}} - \sigma_y(K) = 0 \tag{3.21}$$

where σ_{y0} is the initial yield stress, $\boldsymbol{s} = \boldsymbol{\sigma} - tr[\boldsymbol{\sigma}]\boldsymbol{I}$ are the deviatoric stresses, $\sigma_y(K)$ is the current yield stress and $\mathbb{P}$ is a symmetric fourth order tensor defined as

$$[\mathbb{P}] = \begin{bmatrix} \tilde{\boldsymbol{P}} & \boldsymbol{0} \\ \boldsymbol{0} & \tilde{\boldsymbol{Q}} \end{bmatrix}$$

where

$$\tilde{\boldsymbol{P}} = \begin{bmatrix} F+G & -F & -G \\ -F & F+H & -H \\ -G & H & G+H \end{bmatrix};\ \tilde{\boldsymbol{Q}} = \begin{bmatrix} 2L & 0 & 0 \\ 0 & 2M & 0 \\ 0 & 0 & 2N \end{bmatrix}$$

where F, G, H, L, M and N are material parameters that characterise the orthotropic material and are defined as

$$\begin{aligned} F &= \frac{1}{2}\Big(\frac{1}{R_{22}^2} + \frac{1}{R_{33}^2} - \frac{1}{R_{11}^2}\Big) \\ G &= \frac{1}{2}\Big(\frac{1}{R_{33}^2} + \frac{1}{R_{11}^2} - \frac{1}{R_{22}^2}\Big) \\ H &= \frac{1}{2}\Big(\frac{1}{R_{11}^2} + \frac{1}{R_{22}^2} - \frac{1}{R_{33}^2}\Big) \\ L &= \frac{3}{2R_{23}^2} \\ M &= \frac{3}{2R_{13}^2} \\ N &= \frac{3}{2R_{12}^2} \end{aligned} \tag{3.22}$$

where R_{ij} for $i = 1, 2, 3$ and $j = 1, 2, 3$ are the so called anisotropic yield stress ratios related to a user-defined reference yield stress σ^0 and $\tau^0 = \sigma^0/\sqrt{3}$ according to

$$\begin{aligned} R_{11} &= \frac{\bar{\sigma}_{11}}{\sigma^0} \\ R_{22} &= \frac{\bar{\sigma}_{22}}{\sigma^0} \\ R_{33} &= \frac{\bar{\sigma}_{33}}{\sigma^0} \\ R_{12} &= \frac{\bar{\sigma}_{12}}{\tau^0} \\ R_{13} &= \frac{\bar{\sigma}_{13}}{\tau^0} \\ R_{23} &= \frac{\bar{\sigma}_{23}}{\tau^0} \end{aligned} \tag{3.23}$$

where $\bar{\sigma}_{ij}$ for $i = 1, 2, 3$ and $j = 1, 2, 3$ are the measured current yield stress values when σ_{ij} is applied as the only nonzero stress component [9]. The Hill yield surface is illustrated in Figure 3.2.

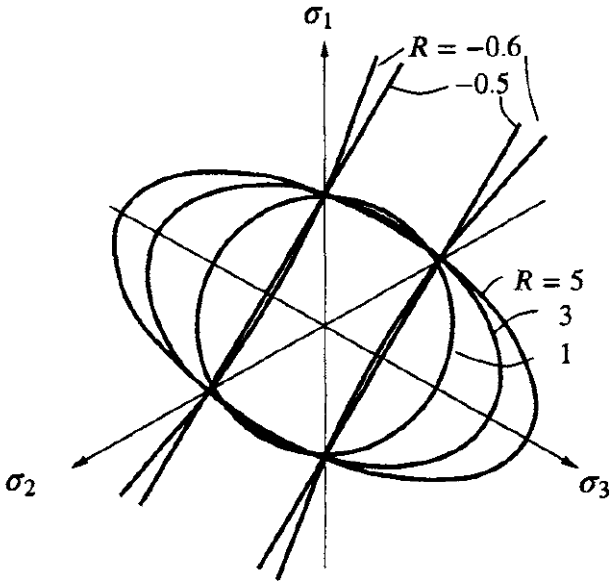

Figure 3.2: Yield curves for Hill's criterion plotted in the deviatoric plane for different R-values [19].

Hill's yield criterion does not distinguish compression from tension, which can clearly be seen in Figure 3.2 [26]. This is important to have in mind when evaluating the modelling results.

The yield criterion is now established and it is possible to compute the following quantities

$$\begin{aligned} \dot{\boldsymbol{\varepsilon}}^p &= \dot{\lambda}\frac{\partial f}{\partial \boldsymbol{\sigma}} = \dot{\lambda}\frac{\sigma_{y0}^2}{\sigma_y}\,\mathbb{P} : \boldsymbol{s} \\ \frac{\partial f}{\partial K} &= -1 \\ H = \frac{\partial K}{\partial \kappa} &= \frac{d\sigma_y(\varepsilon_{eff}^p)}{d\varepsilon_{eff}^p} \end{aligned} \tag{3.24}$$

According to Ottosen and Ristinmaa [19], the constitutive model can be calibrated by using experimental data from uni-axial tension tests. For the uni-axial tension case, the yield criterion in (3.21) get the following form

$$\sigma_y = \sigma_{y0}\,\sigma_{11}\sqrt{F+G} \tag{3.25}$$

Initial yielding occurs when $\sigma_y = \sigma_{y0}$, which means that $\sigma_{11} = 1/\sqrt{F+G}$ at this point. If the evolution law in (3.24) is combined with the criterion in (3.25), one receives

$$\begin{aligned} \dot{\varepsilon}_{11}^p &= \dot{\lambda}\,\sigma_{y0}\sqrt{F+G} \\ \dot{\varepsilon}_{eff}^p &= \frac{\dot{\varepsilon}_{11}^p}{\sigma_{y0}\sqrt{F+G}} \end{aligned} \tag{3.26}$$

The relations in (3.26) can now be utilised to create a stress-plastic strain diagram in order to approximate a curve $\sigma_y = \sigma_y(\varepsilon_{eff}^p)$, which thereafter can be used to compute the plastic modulus H together with the Hill parameters F, G, H, L, M and N.

Another approach was used in this thesis. Here the plastic data for the uni-axial tensile test in MD was used as reference and compared to the plastic data in the other directions. This was done by putting $\sigma^0 = \bar{\sigma}_{11}$ at $\approx 0.1\%$ plastic strain and comparing this reference stress to the corresponding stress in another direction at the same plastic strain. The anisotropic yield ratios $R_{\alpha\beta}$ for $\alpha = 1, 2$ and $\beta = 1, 2$ (only in-plane) could thereafter be computed in accordance with (3.23). This approach proved to yield good results, which can be studied further in Section 5.1.2.

3.2.2 Elasto-plastic stiffness tensor

By combining Hooke's law in (3.8) with the consistency relation in (3.19), the evolution law in (3.15) and the quantities in (3.24), an elasto-plastic relation between the stress

rate and the strain rate can now be determined, i.e.

$$\dot{\boldsymbol{\sigma}} = \mathbb{D}^{ep} : \dot{\boldsymbol{\varepsilon}} \tag{3.27}$$

where the elasto-plastic stiffness tensor $\mathbb{D}^{ep}$ is given by

$$\mathbb{D}^{ep} = \mathbb{D} - \frac{1}{A}\Big(\frac{\sigma_{y0}^2}{\sigma_y}\Big)^2 \Big(\mathbb{D} : \Big(\mathbb{P} : \boldsymbol{s}\Big)\Big) \otimes \Big(\Big(\mathbb{P} : \boldsymbol{s}\Big) : \mathbb{D}\Big) \tag{3.28}$$

and

$$A = H + \Big(\frac{\sigma_{y0}^2}{\sigma_y}\Big)^2 \Big(\mathbb{P} : \boldsymbol{s}\Big) : \Big(\mathbb{D} : \Big(\mathbb{P} : \boldsymbol{s}\Big)\Big)$$

The fourth order tensor $\mathbb{D}^{ep}$ in (3.28) is expressed for a general stress state, which was used during all modelling in Abaqus.

Chapter 4

Fracture and cutting

4.1 Fracture mechanics

Failure in materials occurs when cracks start to propagate [1]. The propagation may be triggered by a combination of material defects and loads. The load cases, or displacement cases, that arise the crack propagation is often divided into three independent crack opening modes: Mode I, Mode II and Mode III. Mode I corresponds to crack opening where the load is applied normal to the crack plane. The other modes are caused by shearing. Mode II corresponds to shearing along the crack, in plane shear, and Mode III corresponds to shearing perpendicular to the crack, out of plane shear. The different modes are illustrated below in Figure 4.1.

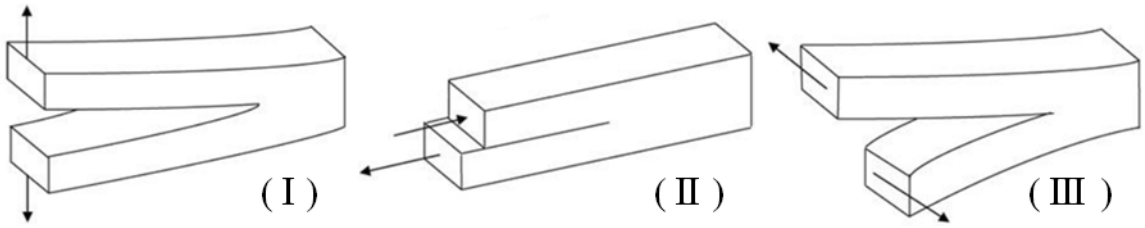

Figure 4.1: The three different fracture modes. From Mode I to the left, to Mode III to the right [8].

A crack starts to propagate when there is enough energy to create the new surfaces. The energy per unit area available for extending a crack is called the energy release rate, G, and the critical energy is called the fracture toughness, G_c [28]. The fracture

criterion can be stated as

$$G \geq G_c \tag{4.1}$$

There are several approaches to determine G and an important parameter to take into account choosing method is the process region [27]. The process region is the area around the crack tip that is affected by the crack propagation, illustrated in Figure 4.2.

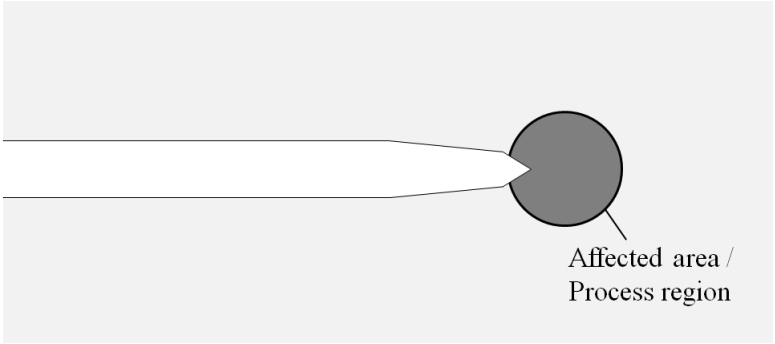

Figure 4.2: Schematic illustration of the process region at the crack tip.

If the process region is small compared to the crack length, i.e. can be described as a single point, traditional methods, such as Linear elastic fracture mechanics (LEFM) and J-integral, can be used [27]. Consider a crack moving acccording to Figure 4.2 for a plane elastic body. Let the crack tip be enclosed by two arbitrary curves C, which is fixed relative to the reference coordinate system, and C_{tip}, which is fixed to and moving with the crack. Let the region between the two curves be free of singularities. Let n_j and n'_j denote normal vectors of C and C_{tip}, respectively. An illustration of the curves and their normal vectors are shown in Figure 4.3.

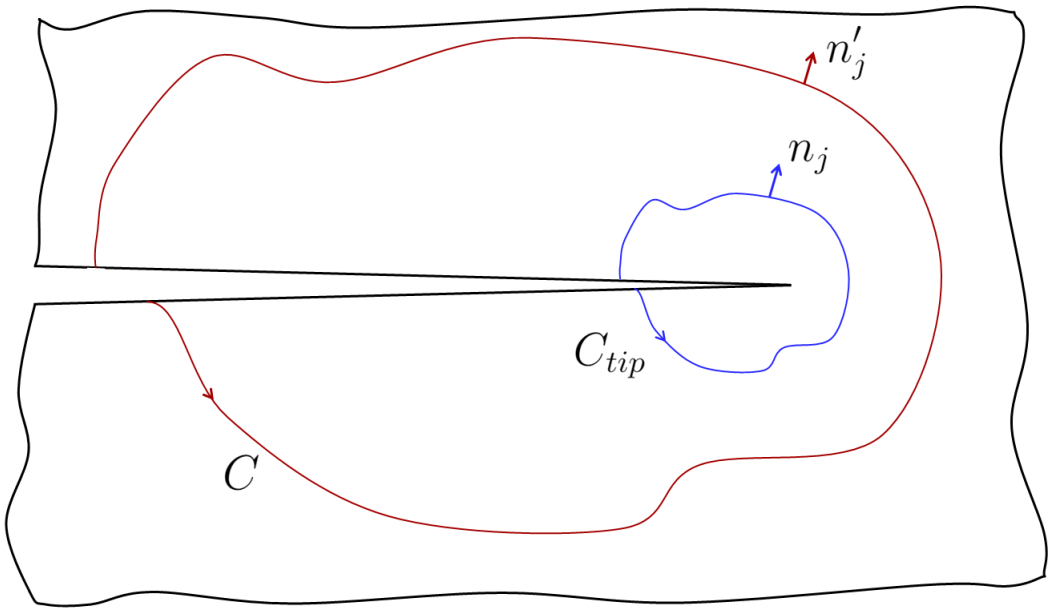

Figure 4.3: The crack enclosed by the curves C and C_{tip} together with their respective normal vectors n_j and n'_j.

The energy flow to crack tip in Figure 4.3, can be computed, independently of the choice of curve, according to

$$J = \int_C (W\,\delta_{1j} - \sigma_{ij}\,u_{i,1})\,n'_j\,dC = \int_{C_{tip}} (W\,\delta_{1j} - \sigma_{ij}\,u_{i,1})\,n_j\,dC_{tip} \tag{4.2}$$

where W is the strain energy density function and σ_{ij} is the stress tensor [17]. The integral expression in (4.2) is called the J-integral.

If the process region cannot be assumed to be small compared to the crack length, different methods should be used instead. Some different possibilities are illustrated in Figure 4.4.

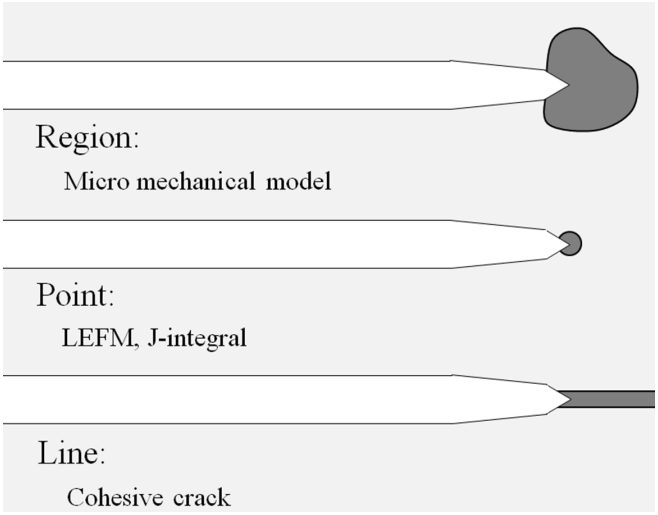

Figure 4.4: Different process region behaviours together with associated suitable modelling approaches.

4.1.1 Cutting

In accordance to what is previously mentioned, simple crack propagation is caused either by tension, shear or a combination of them both and is significantly depending on the amount of energy needed for the crack growth to proceed. When considering cutting, there is no obvious determination on how the material surfaces are separated, since the fracture is forced by an external object. Ståhle, Spagnoli and Terzano [23] explain the cutting by considering a large elastic plate with a single centered crack of length 2a and assuming the knife to have the form of an elliptic wedge, see Figure 4.5.

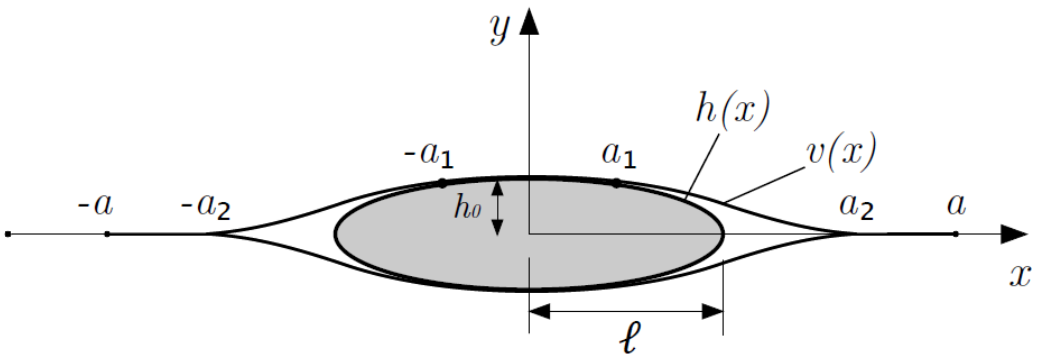

Figure 4.5: Elliptic wedge inside a straight cut. The wedge gives rise to a vertical displacement $h(x) = h_0\sqrt{1-(x/l)^2}$ for $|x| \leq a_1$, where h_0 and l are the elliptic semiaxes of length. In the regions $a_1 < |x| < a_2 \leq a$, the contact between the wedge and the surfaces is lost [23].

The illustrated blunt wedge cut can clearly be described as a Mode I crack opening. The vertical displacement for the crack $v(x)$ can be expressed as

$$v(x) > \begin{cases} h(x) & for \;\; a_1 < |x| < l \\ 0 & for \;\; l \leq |x| < a_2 \end{cases} \tag{4.3}$$

Moreover, the authors discuss the impact of the knife sharpness, where for a sharp knife $l = a_2 = a$, which means that the knife edge and the crack tip are coinciding. This will contribute to singular tensile stresses and discontinuities in the displacement derivative, which will aggravate the modelling when trying to physically describe the phenomenon.

Very brittle materials, such as stone, behave a bit differently from other materials during sharp edge impact. A crushed zone appears in front of the edge resulting in an affected region next to the crack, denoted as chip, see Figure 4.6. This is alike the physical behaviour of paperboard being cut, where the sharp edged knife locally densifies the fibre structure permanently.

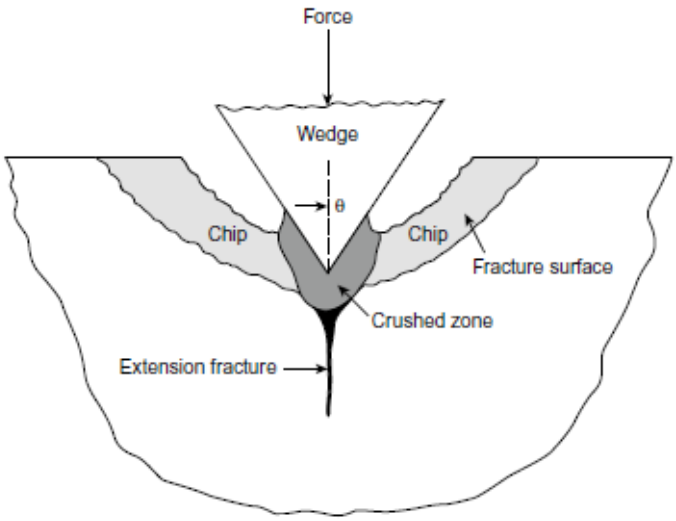

Figure 4.6: Illustration of the crushed-zone behaviour of brittle materials during sharp edge impact[1].

4.2 Modelling

When it comes to modelling of crack propagation there are several different techniques used in industrial applications. Analogously to what is mentioned earlier, different approaches are suitable for different cases. It is in general a good idea to keep the model relatively simple as long as the characteristics of interest are captured in the model.

In the following subsections some available modelling approaches are discussed. The technique that later was implemented is further explained.

4.2.1 Cohesive elements

A cohesive element is a kind of element used in finite element applications and enables a mathematical description of damage. Most models using cohesive elements relate the element stresses to the separation via a traction-separation law. Since the traction-separation law is free to increase and decrease the traction with increasing separation, damage can be described. A convenient way to represent the law is by using a curve. Two traction-separation laws are presented in Figure 4.8. One general curve with a

physically real shape and a simpler triangular shape, which is commonly used because of its simplicity. The traction-separation law is often defined by the cohesive strength, the fracture toughness and the shape of the curve.

Figure 4.7 shows an illustration of a cohesive element during loading.

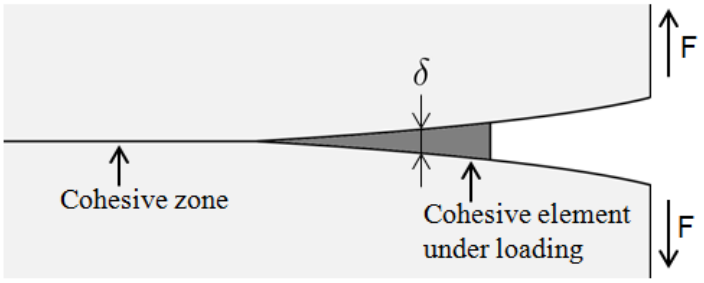

Figure 4.7: Illustration of a cohesive element subjected to loading, where F is the applied force and δ is the separation.

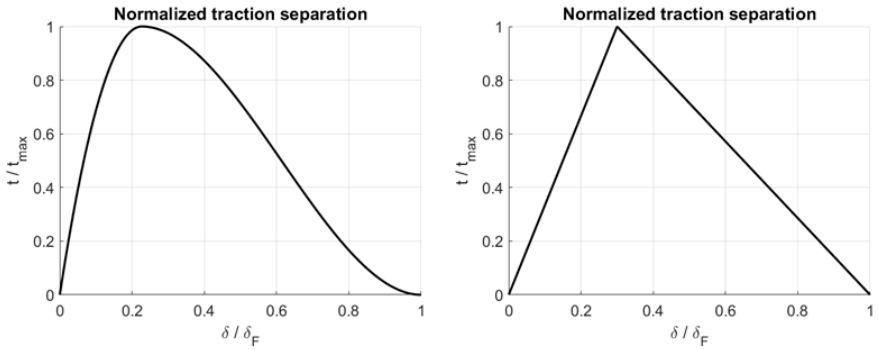

Figure 4.8: Curve representation of two different normalised traction separation laws.

If the traction-separation laws in Figure 4.8 are studied, it can be seen that the element can be loaded up to a certain cohesive strength before damage is initiated. If the element is further loaded, it starts to weaken. When the separation reaches the x-axis, the element is no longer durable enough to carry any load. At this point, the element is advantageously deleted from the model.

The advantage of using cohesive elements is the adaptability of the traction separation law. By calibration of the curve against real measurements, accurate fracture behaviour can be obtained. On the other hand it may be difficult to predict the fracture path and even in applications where the path may seem to be known, for example in Tetra Pak's

slitting application, this is not always the case. This is one of the weaknesses of using cohesive elements. Since the elements are implemented along a certain, predefined fracture path, deviations from this cannot be captured. This may be handled by implementing several different alternative paths, but this could instead lead to meshing difficulties.

4.2.2 Extended finite element method

The extended finite element method (XFEM) is, as the name indicates, a numerical method based on the finite element method (FEM). The extension enables local nodal enrichment functions that make it possible to handle discontinuities and large gradients, problems that really complicates the meshing with FEM. Modelling of crack propagation is a typical situation where such discontinuities and gradients arise, which makes XFEM a suitable and accurate method in order to handle these difficulties. A principle illustration of a XFEM analysis is shown in Figure 4.9. It may be seen that the crack propagates through the elements which greatly simplifies the meshing. This is a feature that is not possible to achieve in standard FEM, but it is in XFEM by proper use of the enrichment functions.

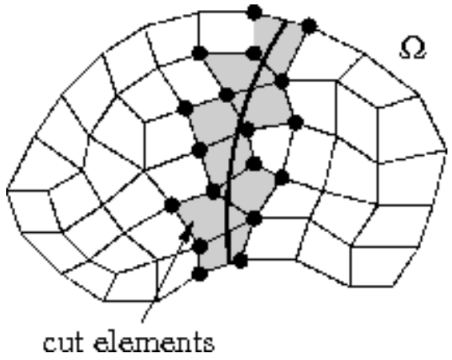

Figure 4.9: Principle illustration of a crack growth analysis with XFEM [10].

XFEM can handle process regions that are considered small in comparison to the crack and size of the specimen, as well as line regions described in Figure 4.4 [9]. Solution methods such as usage of cohesive elements, is implementable even here. What makes the cohesive elements in XFEM different compared to standard FEM, is that the crack is able to propagate through an element and not necessarily between two elements.

XFEM was developed in 1999, which makes it a relatively recent model [15]. Unfortunately, this implies that there today exists a lack of knowledge within the method and the use of enrichment functions, which aggravates its possibilities to be implemented in a conventional structural analysis software. XFEM has therefore not reached the same wide practical use as standard FEM. Despite this it has some obvious advantages when it comes to applications such as crack propagation and may be used with success if used properly.

4.2.3 Element deletion

Element deletion, in this thesis, refers to failure modelling methods where actual elements are deleted at a certain threshold value of a chosen property. This is either done immediately when the value is reached at all Gauss-points within an element or after a specific damage evolution.

This failure approach is easy to implement and understand and is in many applications sufficient to obtain the desired information from the simulation. This is one of the main reasons why it is widely used. While using this modelling method one should however pay attention and be well aware of the shortcomings of the method. The idea of the method is to remove elements from the model, which implies removal of actual mass, not only connections. In an inappropriate implemented model this may imply large leaps in the equilibrium path, resulting in inaccurate solutions. In an adequate model this influence may be reduced, mainly by using a sufficiently fine mesh in exposed regions.

Leaps in the equilibrium path may also lead to convergence difficulties when it comes to mathematically solving the implicit problem [9]. An explicit solver is therefore often used together with this approach. Explicit solvers do not necessarily follow the equilibrium path, which makes it important to use short time increments in order to keep the solver stable, close to equilibrium.

The stable time increment, using an explicit solver, is related to a characteristic element length, density and Young's modulus according to [9]

$$\Delta t \propto \sqrt{\frac{\rho}{E}}\, L_{min} \tag{4.4}$$

Smaller elements yield shorter stable time increments. Since a fine mesh is necessary in order to obtain an accurate failure appearance, the simulations take long time to perform. Sub-modelling and mass-scaling are two different ways of handle this problem. Mass scaling means that extra mass are added to certain elements, which increases the stable time increment. On the other hand, scaling the mass requires investigation of energy levels, e.g. the kinetic energy, to ensure that it does not contribute to inaccurate results.

Thus, even if this method is easy to implement and make it work, the facts stated above impose careful implementation and require a critical point of view when investigating the results.

The chosen modelling approach

Even if XFEM is a very interesting feature, element deletion was considered a good first choice of failure modelling approach. The reason was mainly the method's compatibility and the limited time available.

Ductile damage, a failure feature in Abaqus based on fracture strain, triaxiality and strain rate, was implemented. The model was however calibrated to make the failure independent of triaxiality and strain rate. This was based on the fact that the cutting speed was showed to not influence the cutting force and the triaxiality was never investigated. Furthermore, no damage evolution was implemented, i.e. the element was deleted instantly after reaching a certain strain value for all Gauss-points within the element.

One of the observations from the performed tomographic analysis showed a densification of fibres, which may be interpreted as a permanent compressive strain. The densification was however not quantified and calibration with respect to this quantity was therefore not possible.

More information about the implemented model can be found in the following chapter.

Chapter 5

Modelling in Abaqus

The modelling was divided into two different parts; Tensile testing and cutting testing. The tensile testing was used to validate the calibrated constitutive model that was based on experimental data, explained in Section 2.2.3. The calibrated constitutive model was thereafter used to describe the macroscopic effects during the cutting testing. Additional properties were during the cutting modelling required in order to describe the fracture behaviour. These properties are described further in Section 5.2.1.

5.1 Tensile tests

5.1.1 Procedure

All virtual tensile tests followed the same procedure. A displacement controlled setup was used for these tests. A sketch of the considered load case is shown in Figure 5.1. The constant rate of elongation was set to 7 mm/min for all tests.

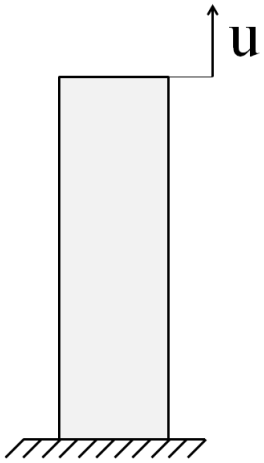

Figure 5.1: The considered load case during the virtual tensile tests. The prescribed displacement is denoted u.

The generated geometry and mesh that was used is shown in Figure 5.2. The mesh consists of hexahedron elements.

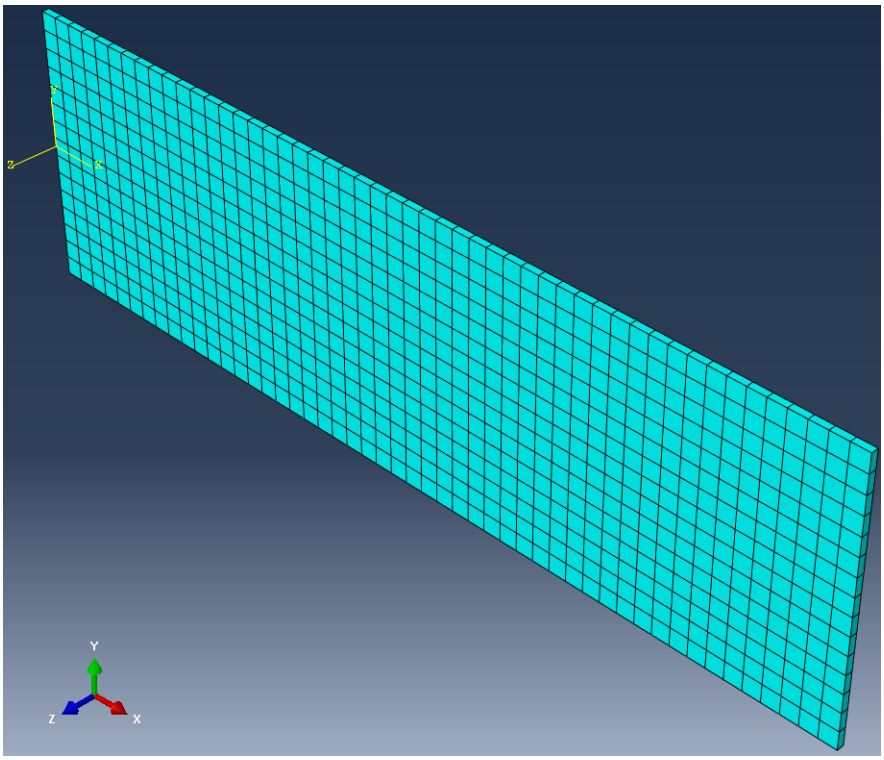

Figure 5.2: The geometry and used mesh during the virtual tensile tests. Hexahedron elements of the element length $L = 1$ mm and element thickness t, which is specified for each paperboard quality in Table 2.1, were used.

The test sample was assigned a Hill constitutive model, consisting of elastic and plastic data as well as potentials, previosly denoted in Section 3.2.1 as anisotropic yield stress ratios. Since the material is assumed to be orthotropic, the material orientation was assigned to the sample in order to capture the anisotropic characteristics. By doing this, Abaqus enables the user to rotate the configuration in order to perform tests in different directions and still capture the anisotropy of the material.

The measured force and displacement for each test were finally analysed and plotted using MATLAB.

5.1.2 Results

The virtual tensile tests performed in MD, 45° and CD for 260 mN paperboard are visualised in terms of von Mises stresses in Figure 5.3. These results are shown just to get a glimpse of how the stress is distributed. The test results for 30 mN, 80 mN and 150 mN are omitted, since their distributions were equivalent, only differing in magnitude.

The Hill calibration resulted in obtaining the Young's moduli for MD, CD and 45° together with three anisotropic yield stress ratios: R_{11}, R_{22} and R_{12}.

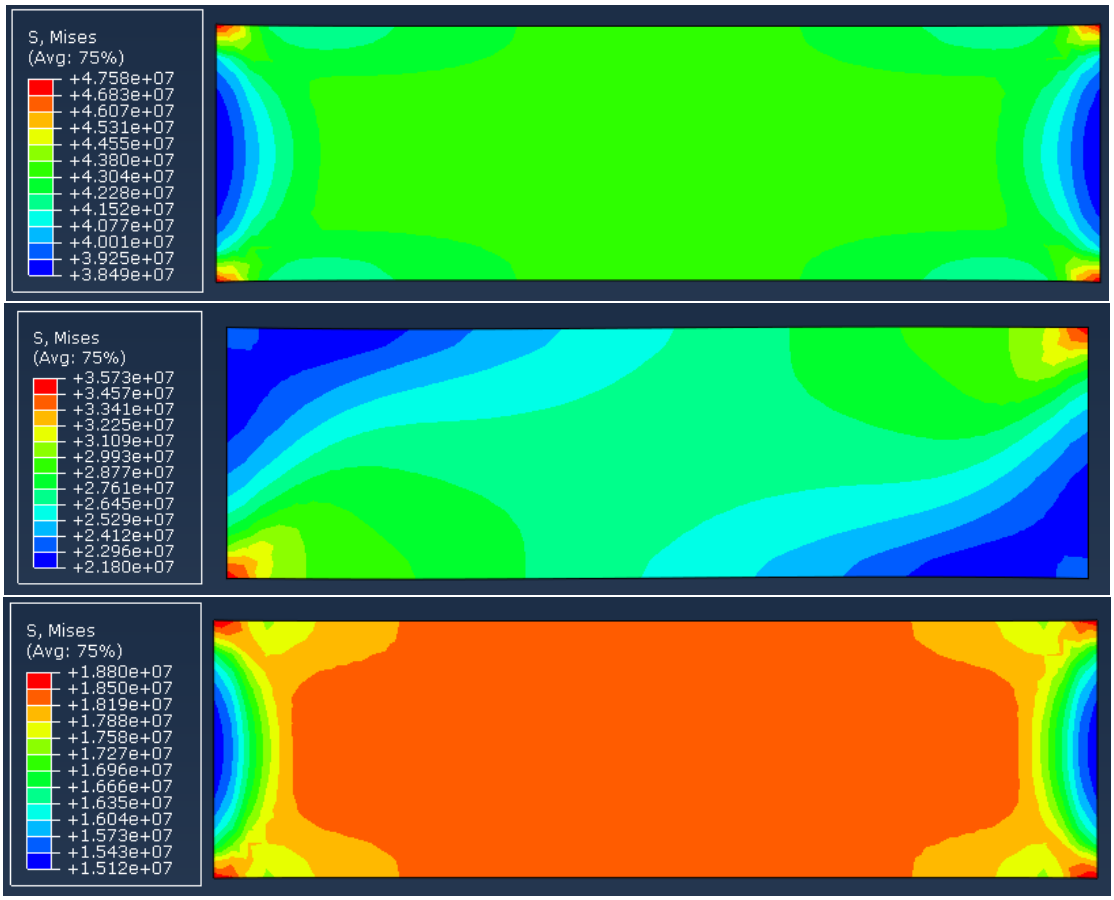

Figure 5.3: Contour plot of the von Mises stresses at approximately 3 % strain. The tests were carried out with 260 mN paperboard for MD (at the top), 45° (in the middle) and CD (at the bottom).

The results from the virtual tensile tests, together with the experimental tensile results, are presented in terms of force-displacement curves in Figure 5.4 - 5.7.

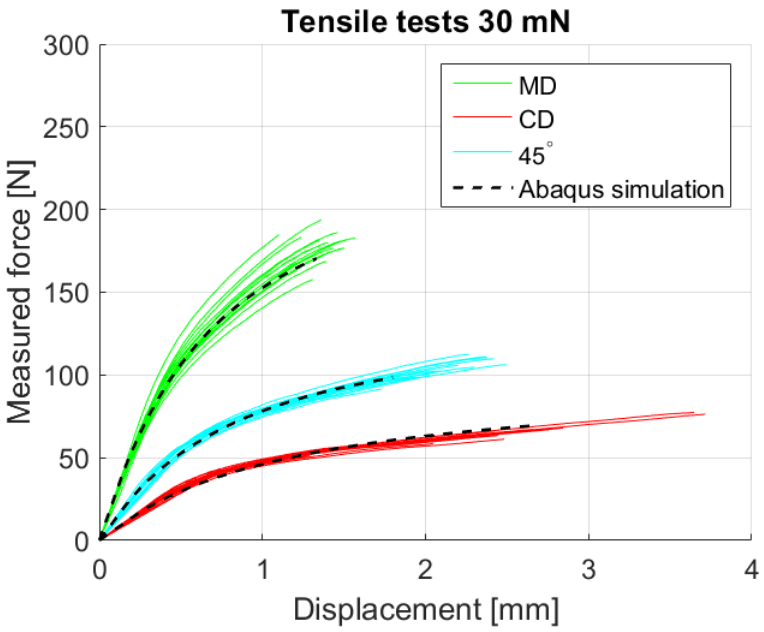

Figure 5.4: Results from experimental and virtual tensile tests carried out with 30 mN paperboard represented in a Force-Displacement curve.

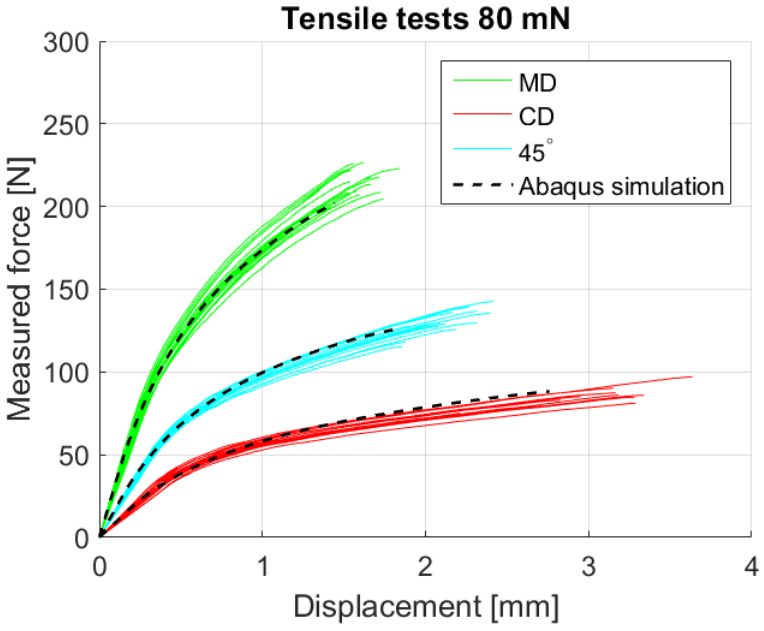

Figure 5.5: Results from experimental and virtual tensile tests carried out with 80 mN paperboard represented in a Force-Displacement curve.

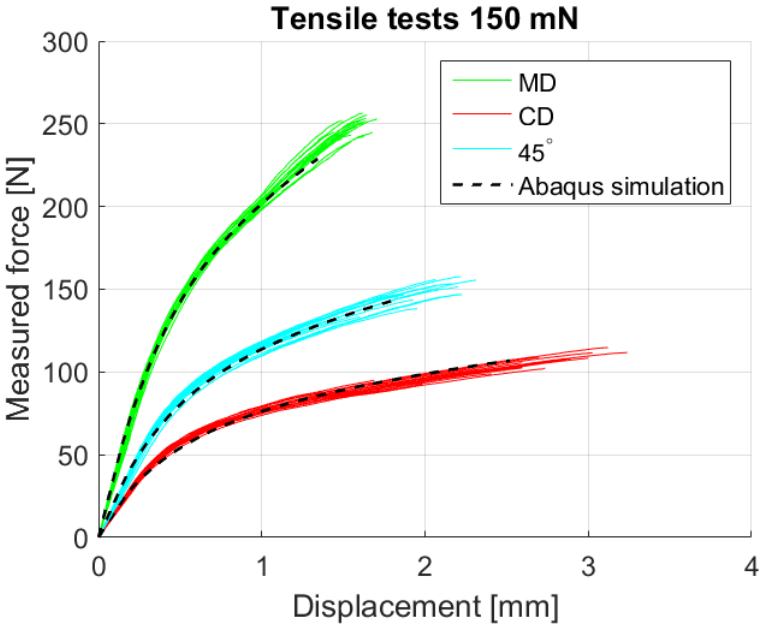

Figure 5.6: Results from experimental and virtual tensile tests carried out with 150 mN paperboard represented in a Force-Displacement curve.

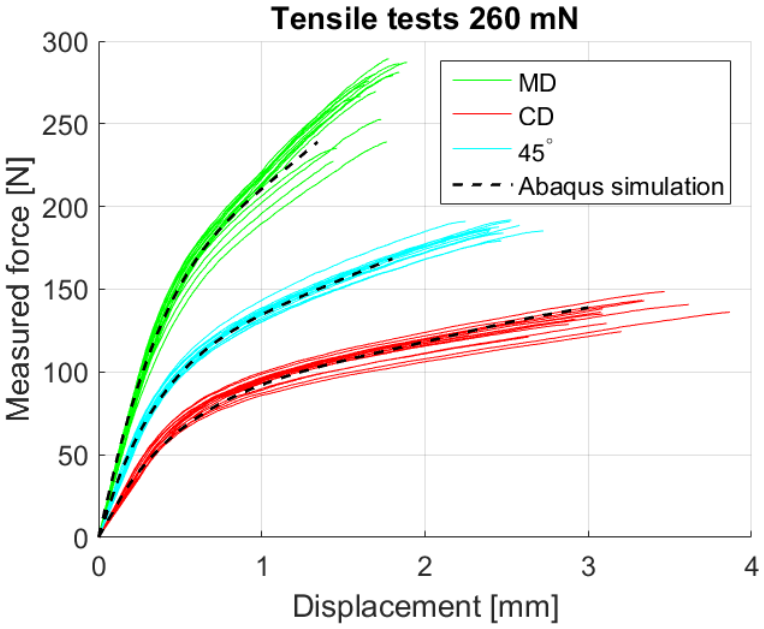

Figure 5.7: Results from experimental and virtual tensile tests carried out with 260 mN paperboard represented in a Force-Displacement curve.

5.2 Cutting tests

5.2.1 Procedure

The virtual cutting tests were set up to evaluate the responses of four different cutting parameters: Bending stiffness (80 mN and 260 mN), material orientation (MD and CD), cutting angle α (0° and 30°) and cutting angle β (0° and 45°). These cutting parameters were during the simulations varied one at a time, with the combination

Bending stiffness	Material orientation	Cutting angle α	Cutting angle β
260 mN	MD	0°	0°

used as a reference case. Additional parameters which were not considered or measured during the experimental tests, were also used in order to find an accurate simulation model. These parameters are presented later in this section, see Table 5.1.

The virtual cutting tests were set up using a displacement controlled setup according to Figure 5.8.

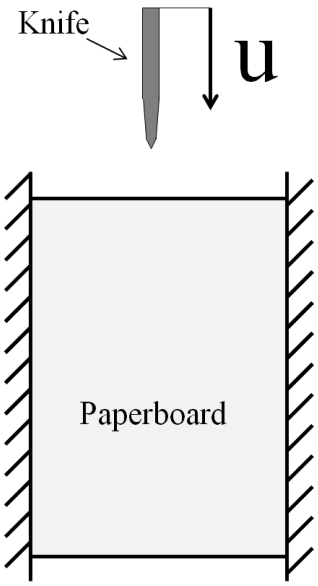

Figure 5.8: The considered load case during the virtual cutting tests. The prescribed displacement is denoted u.

The paperboard geometry was divided into five parts in order to enable different mesh refinements, according to Figure 5.9. Each part was connected by a tie constraint. The strip region enclosing the crack was the region where the most refined mesh was used. It is in this region elements, and thereby mass, are deleted and where loads are expected to be of greatest magnitude.

The generated geometry and mesh that was used for the paperboard is shown in Figure 5.9. The mesh was generated using hexahedrons.

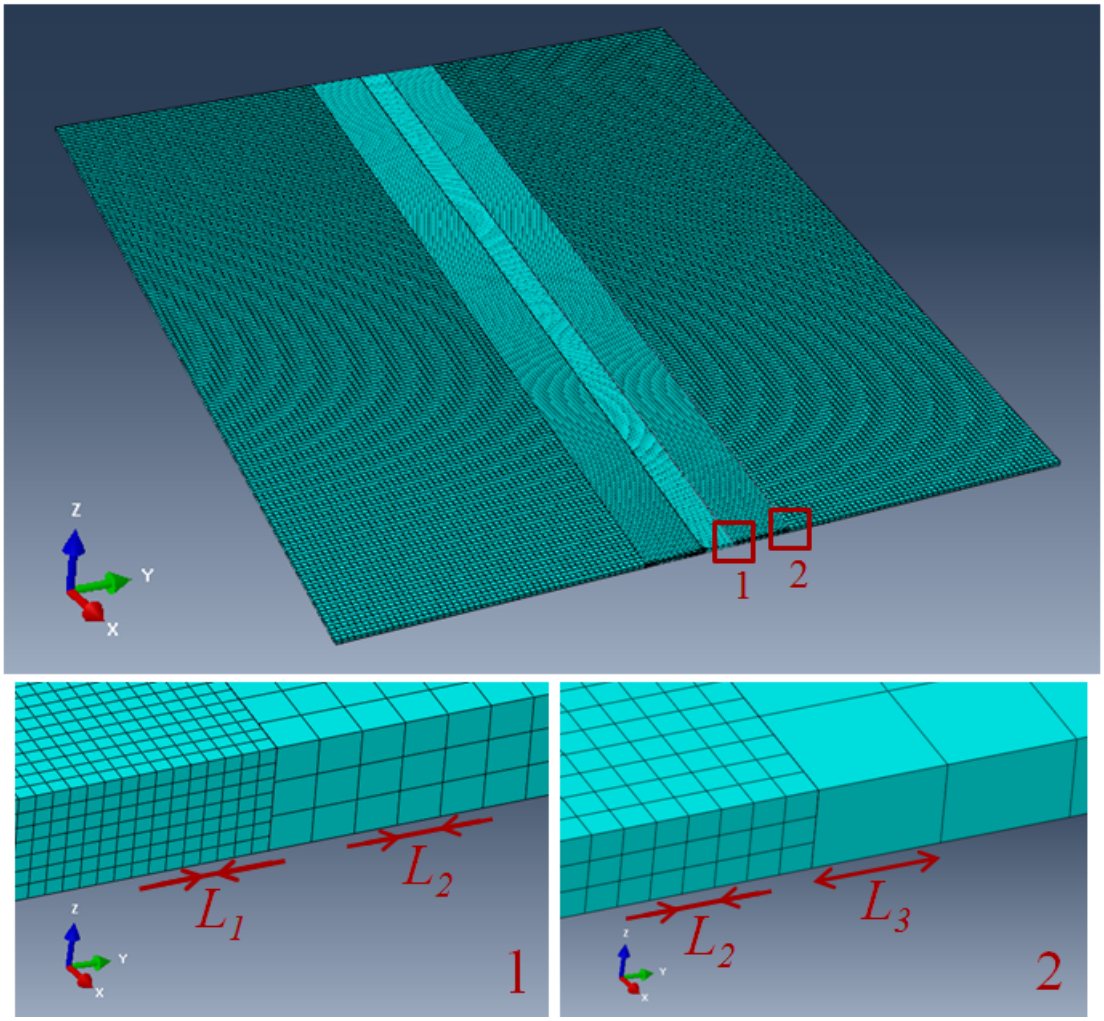

Figure 5.9: The paperboard geometry and used mesh during the virtual cutting tests. The approximate element sizes are: $L_1 = 0.04$ mm $< L_2 = 0.1$ mm $< L_3 = 0.4$ mm.

The generated geometry and mesh that was used for the knife is shown in Figure 5.10. A quad-dominated mesh was used.

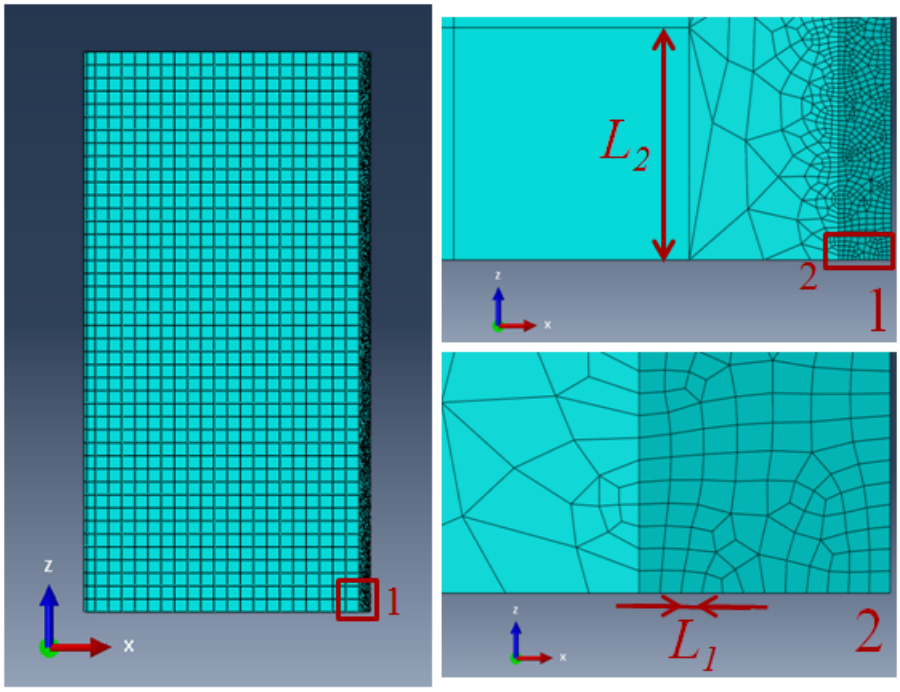

Figure 5.10: The knife geometry and used mesh during the virtual cutting tests. The approximate element sizes are: $L_1 = 0.02$ mm $< L_2 = 1.0$ mm.

The same calibrated Hill constitutive model as in the virtual tensile tests was used for the paperboard during the cutting tests, but here with an additional failure criterion according to Section 4.2.3. This criterion was chosen to only depend on a prescribed fracture strain. Furthermore, the knife was modelled as a rigid shell.

In order to enable contact between the cutting knife and the paperboard, the surface-to-node region based pressure-to-overclosure relation 'Hard Contact' was used. Here, the knife was assigned as the surface region and the paperboard cutting strip, shown in Figure 5.9, was assigned as the node region.

As previously discussed in Section 2.3.3, the magnitude of the cutting force is strongly dependent on the friction forces acting on the cut surfaces as well as the force required to "split" the fibres. With respect to the chosen modelling approach, this could be interpreted as a strong dependence of the coefficient of friction, μ, between the knife and the cut surfaces as well as the fracture strain, ε_f. Based on this, ε_f and μ were, together with the out-of-plane Poisson's ratios ν_{13} and ν_{23}, chosen as calibration parameters in order to capture the magnitude of the measured cutting force and the out-of-plane deformation. The considered calibration parameter space is shown in Table 5.1.

Table 5.1: The considered calibration parameter space.

Calibration parameter						
Fracture strain ε_f	0.01	0.1	0.2	0.4	0.6	0.8
Poisson's ratio ν_{13}/ν_{23}	0	0.2	0.4	0.8	1.6	
Coefficient of friction μ	0.1	0.2	0.3			

In order to find an accurate model, the calibration parameters in Table 5.1 were varied one at a time. A simulation was thereafter initiated and their respective impact on the simulated cutting force was evaluated.

Lastly, mass scaling was implemented in order to achieve a stable time increment of $1 \cdot 10^{-4}$ seconds.

5.2.2 Results

The final calibrated parameters for the cutting model were

Fracture strain ε_f	Poisson's ratio ν_{13}/ν_{23}	Coefficient of friction μ
0.8	0.4	0.2

The obtained results for the five different simulated setups may be seen in Figure 5.11 - 5.25. The figures show the stress distribution for each simulation, a force-displacement curve and an illustration of the out-of-plane deformation.

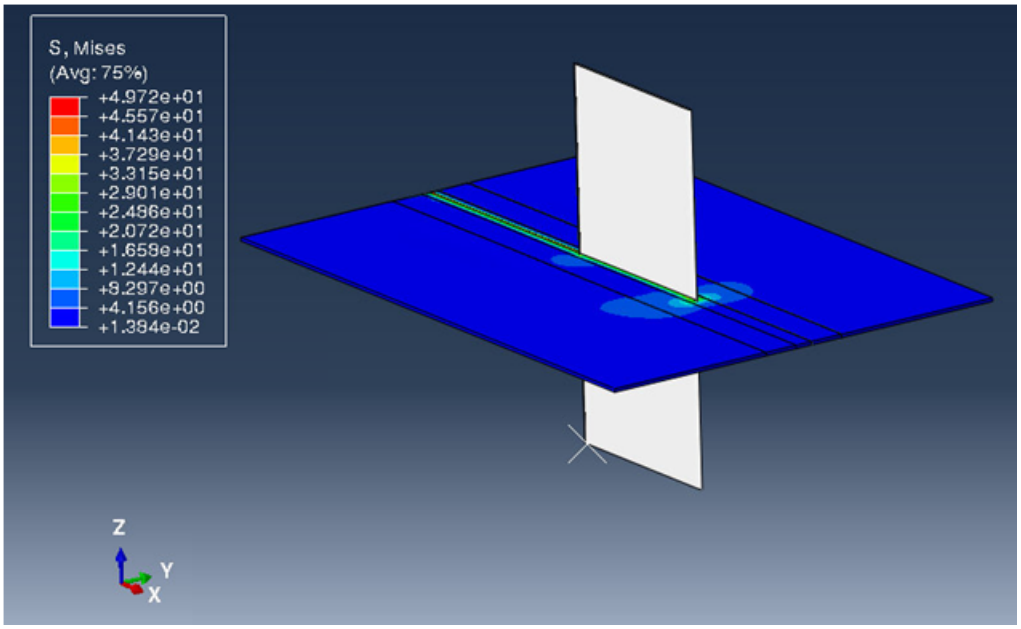

Figure 5.11: Illustration of the stress distribution and the general behaviour of the entire geometry. The simulation is performed with 260 mN paperboard, a cutting speed of 10 mm/s, MD as the cutting direction, the knife angles $\alpha = 0°$ and $\beta = 0°$.

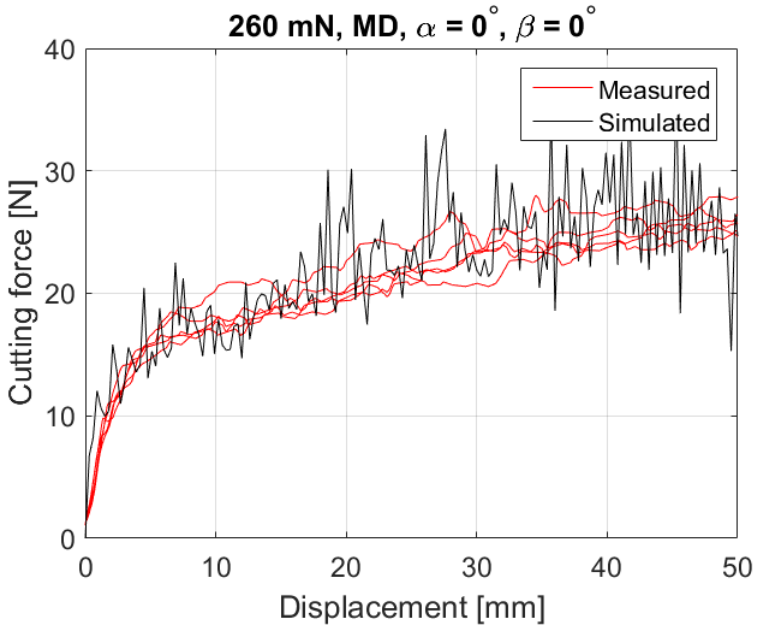

Figure 5.12: Comparison of the measured cutting force and the simulated cutting force with respect to displacement. The simulation is performed with 260 mN paperboard, a cutting speed of 10 mm/s, MD as the cutting direction, the knife angles $\alpha = 0°$ and $\beta = 0°$.

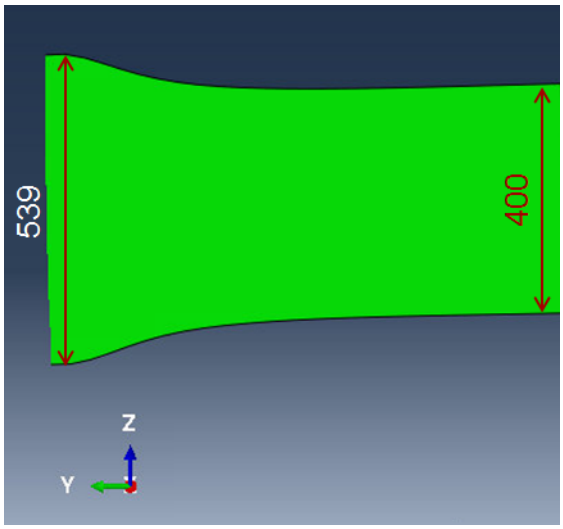

Figure 5.13: Illustration of the out-of-plane deformation from the simulated test. The simulation is performed with 260 mN paperboard, a cutting speed of 10 mm/s, MD as the cutting direction, the knife angles $\alpha = 0°$ and $\beta = 0°$.

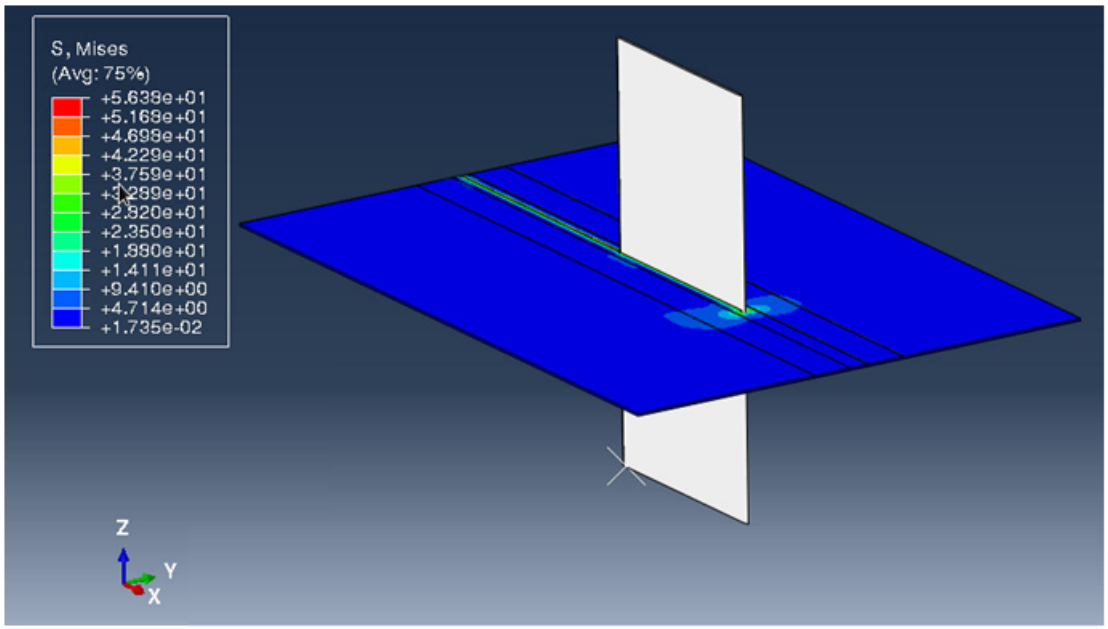

Figure 5.14: Illustration of the stress distribution and the general behaviour of the entire geometry. The simulation is performed with 80 mN paperboard, a cutting speed of 10 mm/s, MD as the cutting direction, the knife angles $\alpha = 0°$ and $\beta = 0°$.

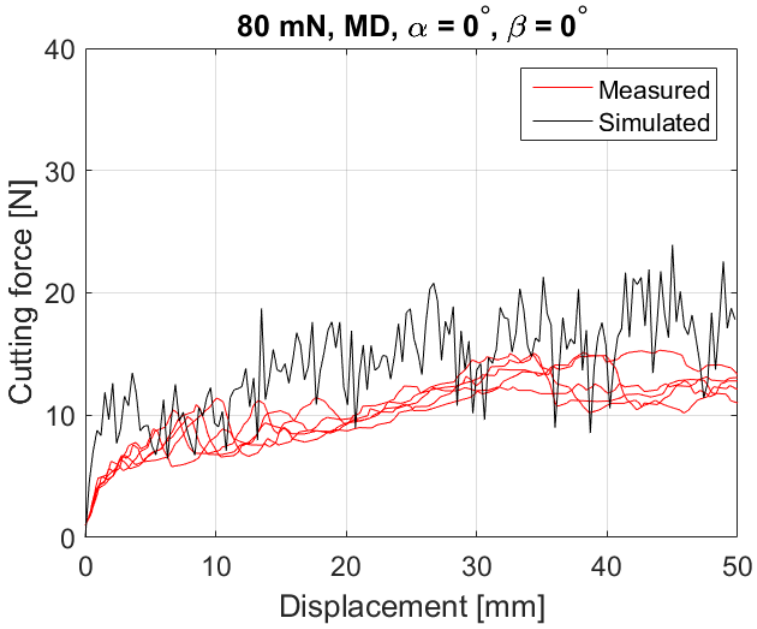

Figure 5.15: Comparison of the measured cutting force and the simulated cutting force with respect to displacement. The simulation is performed with 80 mN paperboard, a cutting speed of 10 mm/s, MD as the cutting direction, the knife angles $\alpha = 0°$ and $\beta = 0°$.

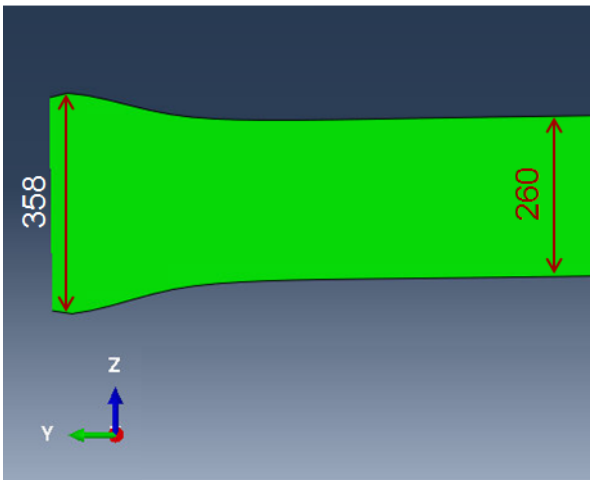

Figure 5.16: Illustration of the out-of-plane deformation from the simulated test. The simulation is performed with 80 mN paperboard, a cutting speed of 10 mm/s, MD as the cutting direction, the knife angles $\alpha = 0°$ and $\beta = 0°$.

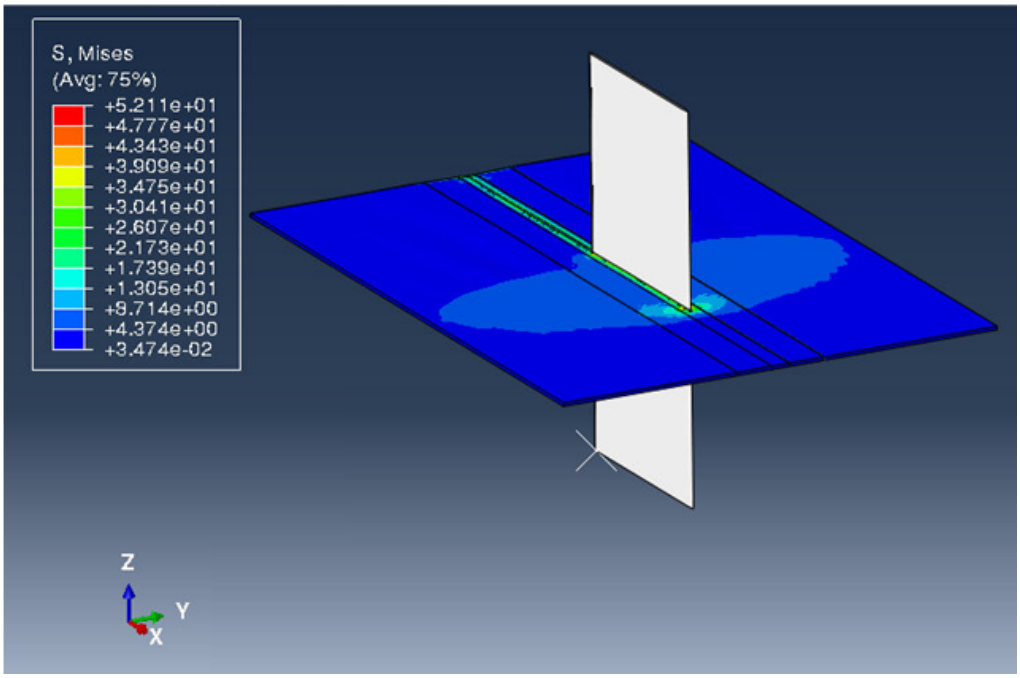

Figure 5.17: Illustration of the stress distribution and the general behaviour of the entire geometry. The simulation is performed with 260 mN paperboard, a cutting speed of 10 mm/s, CD as the cutting direction, the knife angles $\alpha = 0°$ and $\beta = 0°$.

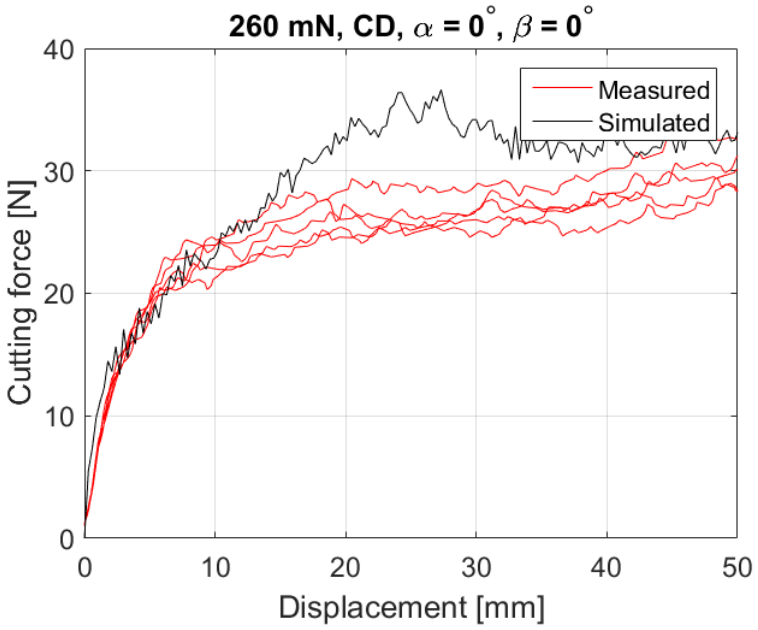

Figure 5.18: Comparison of the measured cutting force and the simulated cutting force with respect to displacement. The simulation is performed with 260 mN paperboard, a cutting speed of 10 mm/s, CD as the cutting direction, the knife angles $\alpha = 0°$ and $\beta = 0°$.

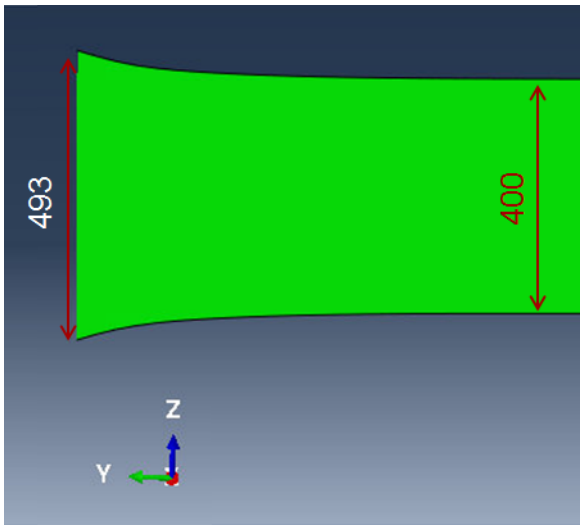

Figure 5.19: Illustration of the out-of-plane deformation from the simulated test. The simulation is performed with 260 mN paperboard, a cutting speed of 10 mm/s, CD as the cutting direction, the knife angles $\alpha = 0°$ and $\beta = 0°$.

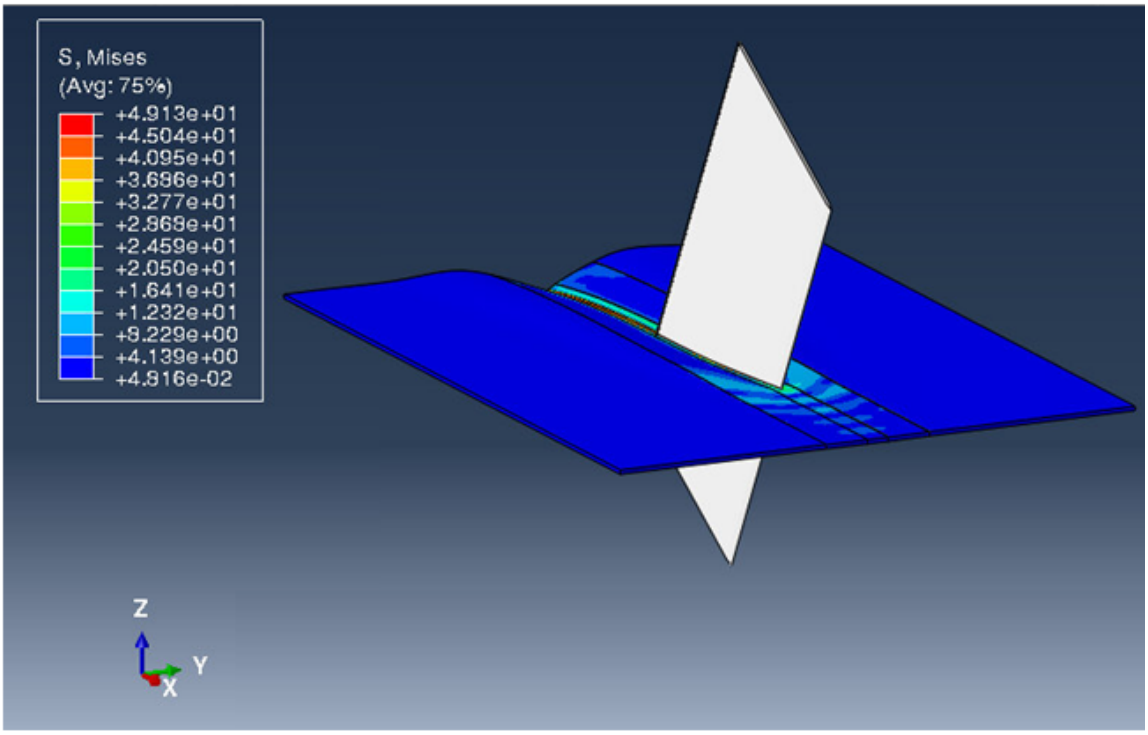

Figure 5.20: Illustration of the stress distribution and the general behaviour of the entire geometry. The simulation is performed with 260 mN paperboard, a cutting speed of 10 mm/s, MD as the cutting direction, the knife angles $\alpha = 30°$ and $\beta = 0°$.

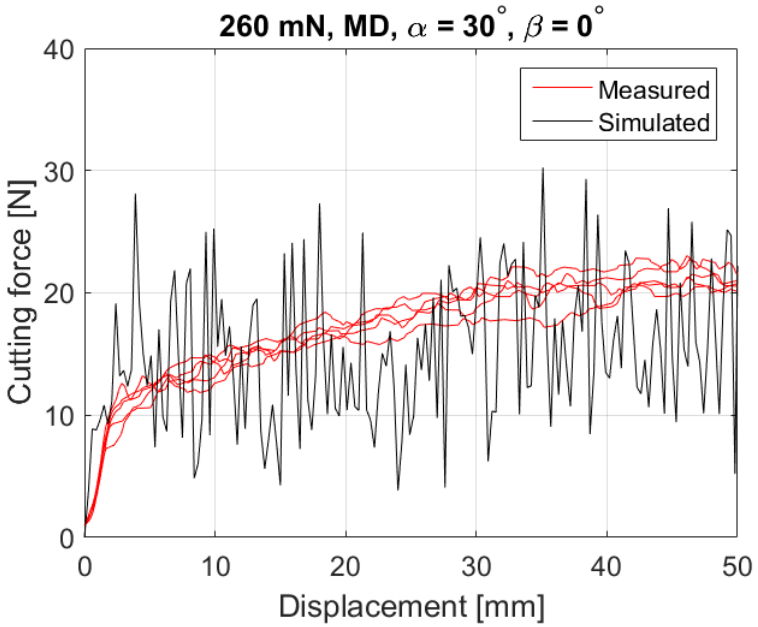

Figure 5.21: Comparison of the measured cutting force and the simulated cutting force with respect to displacement. The simulation is performed with 260 mN paperboard, a cutting speed of 10 mm/s, MD as the cutting direction, the knife angles $\alpha = 30°$ and $\beta = 0°$.

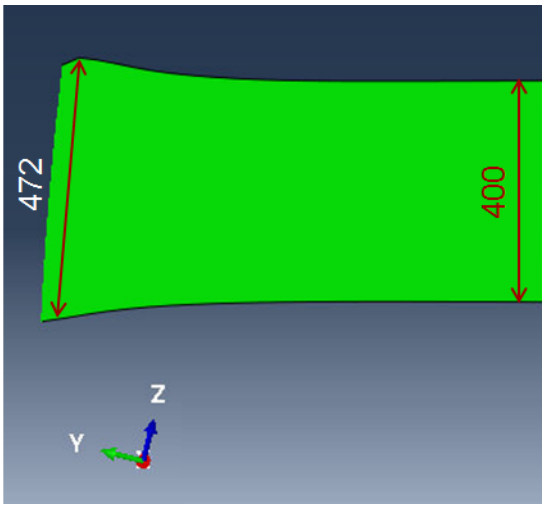

Figure 5.22: Illustration of the out-of-plane deformation from the simulated test. The simulation is performed with 260 mN paperboard, a cutting speed of 10 mm/s, MD as the cutting direction, the knife angles $\alpha = 30°$ and $\beta = 0°$.

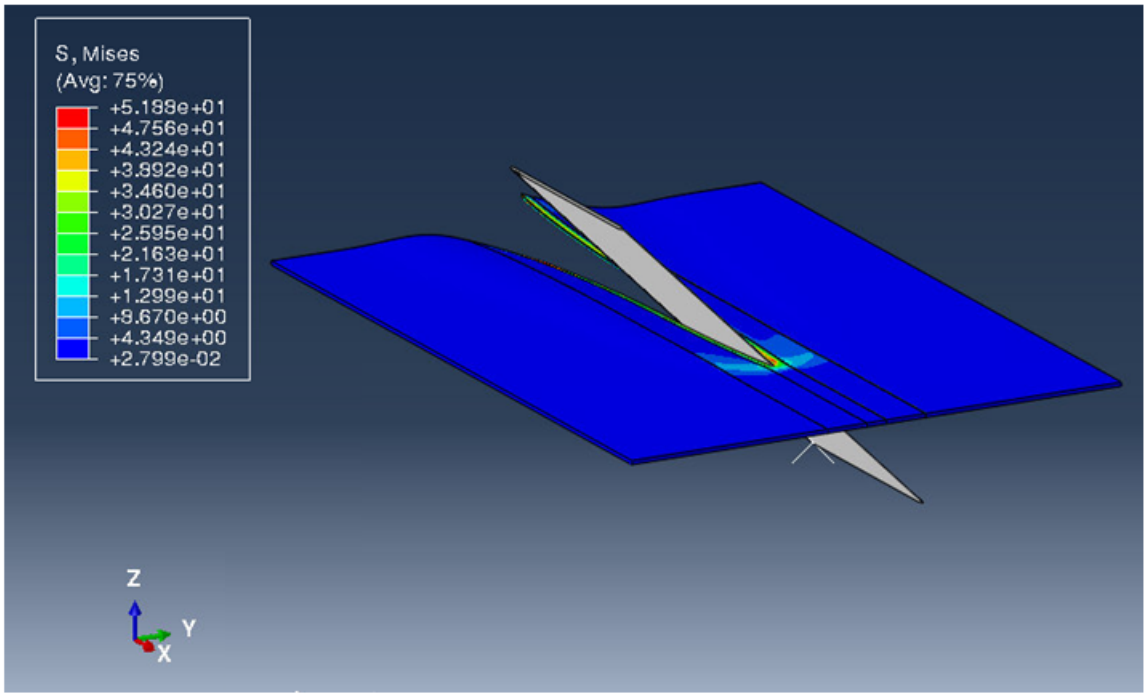

Figure 5.23: Illustration of the stress distribution and the general behaviour of the entire geometry. The simulation is performed with 260 mN paperboard, a cutting speed of 10 mm/s, MD as the cutting direction, the knife angles $\alpha = 0°$ and $\beta = 45°$.

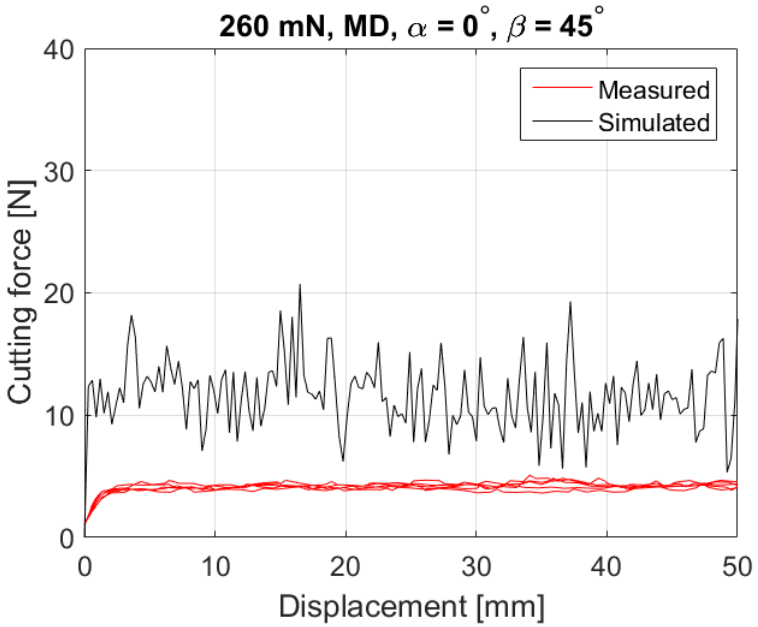

Figure 5.24: Comparison of the measured cutting force and the simulated cutting force with respect to displacement. The simulation is performed with 260 mN paperboard, a cutting speed of 10 mm/s, MD as the cutting direction, the knife angles $\alpha = 0°$ and $\beta = 45°$.

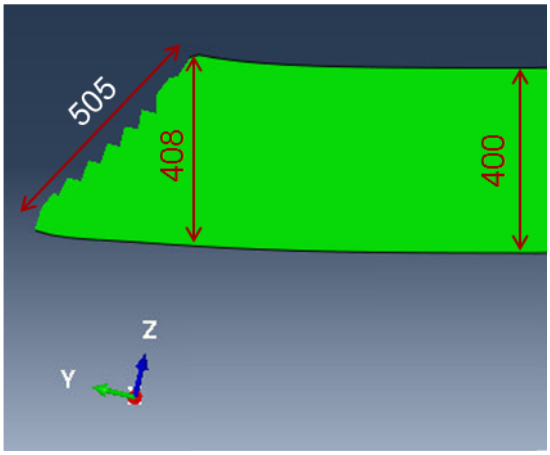

Figure 5.25: Illustration of the out-of-plane deformation from the simulated test. The simulation is performed with 260 mN paperboard, a cutting speed of 10 mm/s, MD as the cutting direction, the knife angles $\alpha = 0°$ and $\beta = 45°$.

The out-of-plane strain for each simulation test, is presented in Table 5.2.

Table 5.2: Out-of-plane strain for the simulated tests.

Simulation setup				Out-of-plane strain ε_3
260 mN,	MD,	$\alpha = 0°$,	$\beta = 0°$	0.35
80 mN,	MD,	$\alpha = 0°$,	$\beta = 0°$	0.38
260 mN,	CD,	$\alpha = 0°$,	$\beta = 0°$	0.23
260 mN,	MD,	$\alpha = 30°$,	$\beta = 0°$	0.18
260 mN,	MD,	$\alpha = 0°$,	$\beta = 45°$	0.02

5.2.3 Analysis

If the simulated results are investigated it can be found that the implemented model captures, at least indications of, most of the observed and measured responses. The impact of the knife angles, α and β, the bending stiffness and material direction on the cutting force, are all considered to be captured. This is probably because these dependencies are mainly caused by geometry; a material failure calibration would however, most likely, make these simulated dependencies fit even better to the measured ones.

The local out-of-plane phenomenon is also considered to be captured in the model. A distinct deformation is present for all simulation cases except for $\beta = 45°$, which, again, is desirable for this specific case. The model does however struggle to capture the macroscopic flexibility of the clamped paperboard sample, where the paperboard should ”recover more” from the macroscopic bending. This behaviour is particularly present in the cases for $\alpha = 0°$ and $\beta = 45°$, seen in Figure 5.20 and 5.23. This could probably be explained by the simplified Hill constitutive model which is used, together with the lack of out-of-plane data. This is further discussed in Section 6.3.

It is difficult to evaluate whether the magnitude of the out-of-plane strains in Table 5.2 is reasonable or not, since not all of the simulated setups were experimentally investigated. In accordance with previously mentioned issues, it is also difficult to determine what parameters that significantly affect the measured out-of-plane strain, except for the cutting angle β. An increase of β will decrease the measured out-of-plane-strain, which also was the case for the simulated tests. To be able to investigate the correspondence

between the measured and simulated out-of-plane strain, the measuring method needs to be improved. This is further discussed in Section 6.3.

Although the simulated responses follow the majority of the observed physical behaviour, some deviations from the measured response are still present. This indicates, for instance, that the relation between friction force and the force needed to split the crack, can be further calibrated. This can be seen in Figure 5.24, which clearly shows that the magnitude of the force needed to split the crack tip is to large. In order to improve the cutting model, the region of element deletion must be decreased and a more accurate investigation of the friction must be performed. Additionally, performing a calibration of the material behaviour based on measurements of the actual failure, would be preferable.

The simulated cutting force is oscillating. This is due to the element deletion and the assigned failure criterion. When elements are deleted, the knife alternates between being in contact in the paperboard crack tip and not being in contact, which creates a disturbance in the force. In order to achieve a more stable cutting force; an even finer mesh can be used or a damage evolution can be implemented to the failure criterion. Moreover, a sharper knife aggravates the crack tip contact and the element deletion even further, which is the case for an increased knife angle α.

As previously mentioned, a mesh study, together with an investigation of the virtual knife edge radius impact and the choice of contact formulation, should be performed.

Chapter 6

Discussion and conclusions

6.1 Summary of thesis outcome

Measurements and investigations regarding cutting and analysis of forced crack propagation, have not previously been performed at Tetra Pak®. Thus, this thesis contributes with new data as well as physical investigations and clarification of experimental observations. Furthermore, the thesis provides a new virtual cutting model, which is more adaptable than the previously used model.

6.2 Measurements discussion

In general the measurements are considered to be performed carefully, and the obtained results should be treated as accurate. Some observations have however contributed to some suspicions, when results where compared with earlier work. These suspicions are discussed in the item list below.

- **Low values of Young's modulus, compared to earlier work -** A probable cause is the clamping length that we chose (50 mm) for the tensile tests. ISO-standard suggests that one should use 100 mm. Our measurements are also based on the thickness measured according to packaging material lab standards, which may be different of the techniques earlier used. The measured paperboard are

probably also less stiff than the paperboard previously measured, and this is not wrong since the specification is the bending stiffness, not the Young's modulus.

- **Large standard deviations in measured Young's modulus -** When implementing the method that determined the Young's modulus for each test, a very short deformation interval was examined. This resulted in relatively large deviation between the different test. Looking at a larger interval may probably have resulted in more gathered results. However, the mean value of the results showed to present the measurements in a accurate way, and therefore no action was considered to be needed.

The physical phenomena that have been observed throughout the thesis have been discussed continuously in the report. These are considered to be clarified and thus no further discussion of these phenomena are needed.

Even if the results are reasonable and are considered to be accurate, there are some possible improvements and sources of errors. Below, these are listed

- Tensile tests should have been performed with 100 $\times$ 15 mm samples, instead of 50 $\times$ 15 mm. This would have made the comparison with earlier measurements fairer. The measured results with the used sample size are not wrong, just different and not measured according to standard.
- The measurements of the out-of-plane deformation were the least consistent. The measure technique could be more standardised and not as dependent of local effects as the measuring technique used in this thesis.
- Some test parameters, such as the clamping distance and cutting angles, were difficult to adjust in the cutting rig. This may contribute to deviations from the planned parameter setup. These possible deviations were never examined further, but the setup was set carefully and this impact is therefore considered to be small.
- In order to capture the responses in regression analyses accurately, more measurements are needed. The regression results were however investigated with a critical point of view, focusing on the main effects of the different parameters, rather than exactly representing the responses. The conclusions based on the regressions are thus considered to be well founded.

- The regression equation for the final experiments includes terms with large multicollinearity (VIF). This means that there are several terms that are predicting more or less the same response, which may effect the conclusions of single parameter responses. Critical thinking and physical reasoning sorted out the responses and the final conclusions are considered to be accurate and well founded.

6.3 Modelling discussion

The developed virtual model of the cutting rig is at an early stage. There is much work left to do before the model can be used in order to predict real responses and decisions can be based upon the simulations.

The model is, however, able to indicate several of the responses that were observed and measured during the experiments. For example, similar responses of the knife angles are obtained and the permanent out-of-plane deformation is possible to capture with an out-of-plane Poisson's ratio not equal to zero.

On the other hand, the simulated material direction dependence was not similar to the measured response. This indicates an inaccuracy in the calibration of the failure appearance, overestimating the force required to make the fibre rupture. In order to handle this miss in calibration, mainly two properties need to be further investigated. Firstly, a calibration against a failure theory is needed. This can for example be the strain or stress at failure. Secondly, the friction between the knife and the paperboard need more thorough investigation. The optimal situation would be to have full understanding of these two properties. If we were able to calibrate one of these, we would however be able to calibrate the second one through a reversed engineering approach. Another property contributing to underestimating the friction in comparison with the normal force acting on the knife edge, is the element deletion. Since actual elements are deleted and not forced to the side, the resulting normal force on the sides of the knife is lowered, in the extension decreasing the friction force. An element deletion criterion that is more limited to the process region would be of interest to use. This would however aggravate the adaptability of the model, since the crack path is aligned differently for different knife angle cases. As previously mentioned, deleting actual mass from the model is not preferable and leads to failure in fulfilling the energy balance.

The mesh dependency was not investigated further, which is of great importance in order to understand the inaccuracy of the model and to get information of crucial levels of mesh density. In models including element deletion this is of even greater interest, since an inaccurate mesh may greatly mislead the results and conclusions based on the model. Other properties that should be investigated further is the knife radius and the implemented contact formulation.

The implemented cutting model has some shortcomings. Firstly, on a macroscopic scale, the used Hill model overestimates the permanent bending of the paperboard. This may be a consequence of the fact that a Hill model does not make difference to loading in compression and tension. It would also be of interest to in a better way capture the permanent out-of-plane deformation, which is not captured in our in-plane calibrated Hill model.

There are however strengths with the used failure approach. The implemented model is very general, in terms of adaptability. There is no predefined cutting path, which allows simulation setups with different knife angles and deviations from a perfect, straight cutting path. The failure modelling approach is also simple and is, as previously motivated, analogous to the observed densification close to the crack.

The other discussed failure approaches do also have strengths and weaknesses. Using cohesive elements would make it easy to calibrate the traction separation law in a way, accurately representing the contact at the crack tip. Cohesive elements would on the other hand restrict the crack to propagate along a predefined crack path, making simulations with different knife angles difficult.

XFEM is considered to be the most interesting feature to aim for in the long run. XFEM neither restricts the crack to propagate along a predicted line, nor requires element deletion. The failure behaviour is instead captured by including intelligence in the element formulations by adding enrichment functions. However, implementing an XFEM model properly is an interesting task, but still time consuming and was therefore not possible to achieve within the given time frame.

6.4 Future work

This thesis built a foundation from which further development should be based, rather than actually solving any manufacturing problem. In order to take actual advantage of the outcome from this thesis, further work and development are needed. Proposals of future work are listed below, together with a short description of the reason why this is proposed and what this would contribute to.

- **Characterise cutting through full packaging material -** In order to understand and mimic the real cutting processes even further, one should consider full packaging material.
- **Perform tests with a blunt knife -** Tests with blunt knives are of great importance to investigate in order to determine the impact of the knife sharpness on paperboard failure. More blunt knives will probably result in reduced cut fineness and a different fibre impact.
- **Perform tests with higher cutting speeds -** The test equipment used during this thesis allowed a top cutting speed of 1000 mm/min. The cutting speed in real manufacturing processes is often much higher than that.
- **Perform more cutting tests -** More tests, more thoroughly covering the parameter space, are needed to verify the parameter responses.
- **Investigate the cut cross section with atomic microscopy -** This is of interest in order to see how fine the cut is on fibre-fibril level.
- **Further investigation of the tomography images -** Quantifying the observations from the tomographic analysis, for example the densificiation, would yield interesting data that can be further used in order to calibrate the virtual model.
- **Investigate tomographic images taken of samples with different cutting settings -** It would be of interest to see if there is any relation between the cutting force and the observations made in the tomography analysis, such as densification, cut fineness and out-of-plane deformation.
- **Improve the cutting rig -** Proposals of improvements are listed below

  - Include simple tools that enable measuring of the clamping distance and the knife angles while assembling the rig. This would really decrease the time needed for testing of different settings.
  - Enable more setting variations in the rig, such as shorter clamping distance and larger knife angles. It would also be of interest to introduce different pretensions in the paperboard and see if the cutting is affected.
  - Enable the usage of rotating knives in the rig in order to simulate the slitting process. Using razor blades are however also of interest since it is more alike other Tetra Pak cutting processes.
  - Make it possible to attach camera equipment to simplify the recording of the cutting process from different angles and at different length scales.

- **Standardise the measuring of the out-of-plane deformation -** To be able to fully understand this phenomenon, there must be a more consistent measuring method, covering a larger region than the procedure used during this thesis. Investigating the thickness along the entire specimen, or at least adding more measuring points per specimen, would be preferable.

- **Measuring the coefficient of friction -** The coefficient of friction between the paperboard and the knife showed to have a great impact. If the coefficient could be experimentally determined, one could more easily set up a more accurate simulation model.

- **Continue developing the cutting model -** This thesis is just the first step.

  - Perform: a mesh study, virtual investigation of the knife radius and investigation of the implemented contact formulation.
  - Calibration against more physical observations.
  - Include more intelligence into the fracture model, for example by using XFEM.
  - What is proven in this thesis, is that the Hill constitutive model does not capture the macroscopic paperboard behaviour accurately and is overestimating the permanent bending deformation. A yield criterion that captures the differences in compression versus tension would be preferable to use. The elasto-plastic continuum model developed by Borgqvist et al. [6] should be considered.

Bibliography

[1] Atkins, T. (2009). *The Science and Engineering of Cutting*. Butterworth-Heinemann, Amsterdam.

[2] Baum, G. A., Brennan, D. C., and Habeger, C. C. (1981). Orthotropic elastic constants of paper. *1981 Annual Meeting Proceedings*, 64:97–101. A Tappi Press publication.

[3] Blom, G., Enger, J., Englund, G., Grandell, J., and Holst, L. (2005). *Sannolikhetstoeri och statistikteori med tillämpningar*. Studentlitteratur, Lund.

[4] Borgqvist, E. (2010). Elasto-plasticty in fem interpreted as a dae system. Master's thesis, Lund University, Division of Solid Mechanics.

[5] Borgqvist, E. (2017). Introduction to Paperboard. Seminar, Tetra Pak Packaging Solutions AB, Base Materials.

[6] Borgqvist, E., Wallin, M., Ristinmaa, M., and Tryding, J. (2015). An anisotropic in-plane and out-of-plane elasto-plastic continuum model for paperboard. *Composite Structures*, 126:184–195.

[7] Carton Council (2017). Carton Facts. http://www.recyclecartons.ca/carton-facts/. Accessed 23 March 2017.

[8] D. Adams (2009). Mixed-mode fracture toughness of composites. http://www.compositesworld.com/articles/mixed-mode-fracture-toughness-of-composites. Accessed 23 March 2017.

[9] Dassault Systèmes (2014). *Abaqus User's Manual 6.14*.

[10] Fries, T.-P. (2017). The Extended Finite Element Method - Introduction. http://www.xfem.rwth-aachen.de/Background/Introduction/XFEM_Introduction.php. Accessed: 2017-05-22.

[11] Harrysson, A. and Ristinmaa, M. (2008). Large strain elasto-plastic model for paper and corrugated board. *International Journal of Solids and Structures*, 45:3334–3352.

[12] Instron (2015). 3300 Dual Column Universal Testing Systems. http://www.instron.se/sv-se/products/testing-systems/universal-testing-systems/electromechanical/3300/3360-dual-column. Accessed: 2017-05-29.

[13] Lekhnitskiy, S. G. (1968). *Anisotropic Plates*. Gordon and Breach Science Publishers Ltd.

[14] Minitab Inc. (2016). *Minitab 17 Support*.

[15] Moës, N., Dolbow, J., and Belytschko, T. (1999). A finite element method for crack growth without remeshing. *International Journal for Numerical Methods in Engineering*, 46:131–150.

[16] Mäkelä, P. (2002). On the fracture mechanics of paper. *Nordic Pulp and Paper Research*, 17:254–274.

[17] Nilsson, F. (2001). *Fracture Mechanics - from Theory to Applications*. Department of Solid Mechanics, KTH, Stockholm.

[18] Nygård, M. (2008). Experimental techniques for characterization of elastic-plastic properties in paperboard. *Nordic Pulp and Paper Research Journal*, 23:432–437.

[19] Ottosen, N. S. and Ristinmaa, M. (2005). *The Mechanics of Constitutive Modeling*. Elsevier, Lund.

[20] Ottosen, N. S., Ristinmaa, M., and Ljung, C. (2007). *Hållfasthetslära : Allmäna tillstånd*. Studentlitteratur, Lund.

[21] Scandinavian Pulp, Paper and Board Testing Committee (1995). Scan-p 29:95. http://www.pfi.no/Documents/Scan_test_methods/P/P_29-95.pdf. Accessed 19 May 2017.

[22] Stenberg, N. (2003). A model for the through-thickness elastic-plastic behaviour of paper. *International Journal of Solids and Structures*, 40:7483–7498.

[23] Ståhle, P., Spagnoli, A., and Terzano, M. (2017). On the fracture processes of cutting. *Italian Group of Fracture Conference*, 24:468–476.

[24] Tetra Pak (2017). Tetra Pak processing and packaging solutions for food and beverages. http://tetrapak.com. Accessed: 2017-05-21.

[25] Tetra Pak employees (2017). Internal communication.

[26] Tryding, J. (1996). *In-Plane Fracture of Paper*. PhD thesis, Lund University, Division of Structural Mechanics.

[27] Tryding, J. and Borgqvist, E. (2017). In-plane fracture and delamination. Seminar, Tetra Pak Packaging Solutions AB, Base Materials.

[28] Williams, J. G. and Patel, Y. (2016). Fundamentals of cutting. *Interface focus*, 6:1–6.

[29] Xia, Q. S., Boyce, M. C., and Parks, D. M. (2002). A constitutive model for the anisotropic elastic-plastic deformation of paper and paperboard. *International Journal of Solids and Structures*, 39:4053–4071.

[30] Zeiss (2016). ZEISS Xradia 520 Versa. //www.zeiss.com/content/dam/Microscopy/us/download/pdf/Products/xradia520versa/xradia-520-versa-product-information.pdf. Accessed: 2017-05-29.

Appendix A

Plastic data

30 mN Paperboard

Table A.1: 30 mN paperboard plastic modelling data - Part 1.

Stress [MPa]	Strain [-]	Stress [MPa]	Strain [-]	Stress [MPa]	Strain [-]
15.01875145	0	35.16900184	0.0018	43.06056393	0.0036
17.91641175	0.0001	35.73206634	0.0019	43.40071484	0.0037
20.04637728	0.0002	36.274811	0.002	43.73368884	0.0038
21.78595798	0.0003	36.79874474	0.0021	44.05979276	0.0039
23.27833227	0.0004	37.30520563	0.0022	44.37931409	0.004
24.59622555	0.0005	37.79538676	0.0023	44.6925226	0.0041
25.78258463	0.0006	38.27035728	0.0024	44.99967179	0.0042
26.86527594	0.0007	38.73107959	0.0025	45.30100023	0.0043
27.86359498	0.0008	39.17842371	0.0026	45.59673274	0.0044
28.79155551	0.0009	39.61317917	0.0027	45.88708143	0.0045
29.65971481	0.001	40.03606499	0.0028	46.17224669	0.0046
30.4762602	0.0011	40.44773819	0.0029	46.45241801	0.0047
31.24769244	0.0012	40.84880099	0.003	46.72777483	0.0048
31.97927497	0.0013	41.23980695	0.0031	46.99848719	0.0049
32.67534008	0.0014	41.62126626	0.0032	47.26471643	0.005
33.33950416	0.0015	41.99365035	0.0033	47.52661573	0.0051
33.97482288	0.0016	42.35739585	0.0034	47.78433069	0.0052
34.58390567	0.0017	42.71290805	0.0035	48.03799982	0.0053

Table A.2: 30 mN paperboard plastic modelling data - Part 2.

Stress [MPa]	Strain [-]	Stress [MPa]	Strain [-]	Stress [MPa]	Strain [-]
48.28775498	0.0054	54.76507454	0.0086	59.42599296	0.0118
48.5337218	0.0055	54.93224273	0.0087	59.55174409	0.0119
48.77602005	0.0056	55.09778629	0.0088	59.67641533	0.012
49.01476404	0.0057	55.26173622	0.0089	59.80001262	0.0121
49.25006287	0.0058	55.42412234	0.009	59.9225414	0.0122
49.48202079	0.0059	55.5849733	0.0091	60.04400661	0.0123
49.71073746	0.006	55.74431664	0.0092	60.16441277	0.0124
49.93630819	0.0061	55.90217882	0.0093	60.2837639	0.0125
50.15882421	0.0062	56.05858523	0.0094	60.40206359	0.0126
50.37837284	0.0063	56.21356027	0.0095	60.51931499	0.0127
50.59503777	0.0064	56.36712734	0.0096	60.63552083	0.0128
50.80889917	0.0065	56.51930887	0.0097	60.75068343	0.0129
51.02003392	0.0066	56.67012641	0.0098	60.86480468	0.013
51.22851576	0.0067	56.81960055	0.0099	60.97788611	0.0131
51.43441546	0.0068	56.96775106	0.01	61.08992884	0.0132
51.63780093	0.0069	57.11459683	0.0101	61.20093364	0.0133
51.83873737	0.007	57.26015594	0.0102	61.31090089	0.0134
52.03728743	0.0071	57.40444566	0.0103	61.41983063	0.0135
52.23351128	0.0072	57.54748248	0.0104	61.52772255	0.0136
52.42746674	0.0073	57.68928215	0.0105	61.63457601	0.0137
52.6192094	0.0074	57.82985965	0.0106	61.74039004	0.0138
52.80879268	0.0075	57.96922927	0.0107	61.84516334	0.0139
52.99626797	0.0076	58.10740459	0.0108	61.94889432	0.014
53.18168467	0.0077	58.2443985	0.0109	62.05158109	0.0141
53.36509031	0.0078	58.38022325	0.011	62.15322145	0.0142
53.54653061	0.0079	58.51489041	0.0111	62.25381293	0.0143
53.72604953	0.008	58.64841095	0.0112	62.35335278	0.0144
53.90368939	0.0081	58.7807952	0.0113	62.45183801	0.0145
54.0794909	0.0082	58.9120529	0.0114	62.54926534	0.0146
54.2534932	0.0083	59.04219323	0.0115	62.64563127	0.0147
54.42573398	0.0084	59.17122475	0.0116	62.74093203	0.0148
54.59624947	0.0085	59.29915549	0.0117	62.83516365	0.0149

Table A.3: 30 mN paperboard plastic modelling data - Part 3.

Stress [MPa]	Strain [-]	Stress [MPa]	Strain [-]	Stress [MPa]	Strain [-]
62.92832192	0.015	65.30886473	0.0182	66.52496646	0.0214
63.02040243	0.0151	65.36325478	0.0183	66.55643753	0.0215
63.11140054	0.0152	65.416352	0.0184	66.58790859	0.0216
63.20131144	0.0153	65.4681492	0.0185	66.61937966	0.0217
63.29013011	0.0154	65.51863923	0.0186	66.65085072	0.0218
63.37785135	0.0155	65.56781498	0.0187	66.68232178	0.0219
63.46446981	0.0156	65.61566938	0.0188	66.71379285	0.022
63.54997994	0.0157	65.66219542	0.0189	66.74526391	0.0221
63.63437605	0.0158	65.70738615	0.019	66.77673498	0.0222
63.71765231	0.0159	65.75123467	0.0191	66.80820604	0.0223
63.79980272	0.016	65.79373416	0.0192	66.83967711	0.0224
63.88082119	0.0161	65.83487786	0.0193	66.87114817	0.0225
63.96070144	0.0162	65.87465909	0.0194	66.90261923	0.0226
64.03943714	0.0163	65.91307126	0.0195	66.9340903	0.0227
64.1170218	0.0164	65.95010786	0.0196	66.96556136	0.0228
64.19344884	0.0165	65.98576247	0.0197	66.99703243	0.0229
64.2687116	0.0166	66.02002876	0.0198	67.02850349	0.023
64.3428033	0.0167	66.0529005	0.0199	67.05997455	0.0231
64.4157171	0.0168	66.08437157	0.02	67.09144562	0.0232
64.48744609	0.0169	66.11584263	0.0201	67.12291668	0.0233
64.55798327	0.017	66.1473137	0.0202	67.15438775	0.0234
64.62732161	0.0171	66.17878476	0.0203	67.18585881	0.0235
64.695454	0.0172	66.21025582	0.0204	67.21732987	0.0236
64.7623733	0.0173	66.24172689	0.0205	67.24880094	0.0237
64.82807232	0.0174	66.27319795	0.0206	67.280272	0.0238
64.89254384	0.0175	66.30466902	0.0207	67.31174307	0.0239
64.95578063	0.0176	66.33614008	0.0208	67.34321413	0.024
65.01777543	0.0177	66.36761114	0.0209	67.37468519	0.0241
65.07852095	0.0178	66.39908221	0.021	67.40615626	0.0242
65.13800991	0.0179	66.43055327	0.0211	67.43762732	0.0243
65.19623505	0.018	66.46202434	0.0212	67.46909839	0.0244
65.25318907	0.0181	66.4934954	0.0213	67.50056945	0.0245

Table A.4: 30 mN paperboard plastic modelling data - Part 4.

Stress [MPa]	Strain [-]	Stress [MPa]	Strain [-]	Stress [MPa]	Strain [-]
67.53204052	0.0246	68.12999073	0.0265	68.72794095	0.0284
67.56351158	0.0247	68.1614618	0.0266	68.75941201	0.0285
67.59498264	0.0248	68.19293286	0.0267	68.79088308	0.0286
67.62645371	0.0249	68.22440392	0.0268	68.82235414	0.0287
67.65792477	0.025	68.25587499	0.0269	68.85382521	0.0288
67.68939584	0.0251	68.28734605	0.027	68.88529627	0.0289
67.7208669	0.0252	68.31881712	0.0271	68.91676733	0.029
67.75233796	0.0253	68.35028818	0.0272	68.9482384	0.0291
67.78380903	0.0254	68.38175925	0.0273	68.97970946	0.0292
67.81528009	0.0255	68.41323031	0.0274	69.01118053	0.0293
67.84675116	0.0256	68.44470137	0.0275	69.04265159	0.0294
67.87822222	0.0257	68.47617244	0.0276	69.07412266	0.0295
67.90969328	0.0258	68.5076435	0.0277	69.10559372	0.0296
67.94116435	0.0259	68.53911457	0.0278	69.13706478	0.0297
67.97263541	0.026	68.57058563	0.0279	69.16853585	0.0298
68.00410648	0.0261	68.60205669	0.028	69.20000691	0.0299
68.03557754	0.0262	68.63352776	0.0281	69.23147798	0.03
68.0670486	0.0263	68.66499882	0.0282		
68.09851967	0.0264	68.69646989	0.0283		

80 mN Paperboard

Table A.5: 80 mN paperboard plastic modelling data - Part 1.

Stress [MPa]	Strain [-]	Stress [MPa]	Strain [-]	Stress [MPa]	Strain [-]
12.59176188	0	33.11437393	0.0031	40.23096447	0.0062
14.82178402	0.0001	33.41470528	0.0032	40.41063729	0.0063
16.48139293	0.0002	33.70805535	0.0033	40.5883009	0.0064
17.84267327	0.0003	33.99477302	0.0034	40.76401995	0.0065
19.01277516	0.0004	34.27518234	0.0035	40.93785638	0.0066
20.04705403	0.0005	34.54958487	0.0036	41.10986956	0.0067
20.97852751	0.0006	34.81826181	0.0037	41.28011644	0.0068
21.8287626	0.0007	35.08147585	0.0038	41.44865158	0.0069
22.61276434	0.0008	35.33947283	0.0039	41.61552737	0.007
23.34146986	0.0009	35.59248322	0.004	41.78079402	0.0071
24.02314196	0.001	35.84072335	0.0041	41.94449972	0.0072
24.66420318	0.0011	36.08439665	0.0042	42.10669069	0.0073
25.26976271	0.0012	36.32369466	0.0043	42.26741129	0.0074
25.84396384	0.0013	36.55879796	0.0044	42.42670408	0.0075
26.39022158	0.0014	36.78987702	0.0045	42.58460986	0.0076
26.91139003	0.0015	37.01709294	0.0046	42.7411678	0.0077
27.4098833	0.0016	37.24059816	0.0047	42.89641545	0.0078
27.88776495	0.0017	37.46053708	0.0048	43.05038882	0.0079
28.34681525	0.0018	37.67704661	0.0049	43.20312243	0.008
28.78858277	0.0019	37.89025668	0.005	43.35464936	0.0081
29.21442448	0.002	38.10029075	0.0051	43.5050013	0.0082
29.62553733	0.0021	38.30726615	0.0052	43.65420861	0.0083
30.02298343	0.0022	38.51129459	0.0053	43.80230033	0.0084
30.40771045	0.0023	38.71248241	0.0054	43.94930425	0.0085
30.78056806	0.0024	38.91093095	0.0055	44.09524694	0.0086
31.1423216	0.0025	39.10673689	0.0056	44.24015378	0.0087
31.49366331	0.0026	39.29999246	0.0057	44.384049	0.0088
31.83522172	0.0027	39.49078574	0.0058	44.52695571	0.0089
32.16756959	0.0028	39.67920087	0.0059	44.66889594	0.009
32.49123054	0.0029	39.8653183	0.006	44.80989064	0.0091
32.80668477	0.003	40.04921496	0.0061	44.94995976	0.0092

Table A.6: 80 mN paperboard plastic modelling data - Part 2.

Stress [MPa]	Strain [-]	Stress [MPa]	Strain [-]	Stress [MPa]	Strain [-]
45.08912222	0.0093	49.13171581	0.0125	52.38478486	0.0157
45.22739596	0.0094	49.24611887	0.0126	52.47083814	0.0158
45.36479797	0.0095	49.35978892	0.0127	52.55579049	0.0159
45.50134432	0.0096	49.47272007	0.0128	52.6396268	0.016
45.63705013	0.0097	49.58490598	0.0129	52.72233195	0.0161
45.77192965	0.0098	49.69633979	0.013	52.80389077	0.0162
45.90599625	0.0099	49.8070142	0.0131	52.88428804	0.0163
46.03926246	0.01	49.91692146	0.0132	52.96350857	0.0164
46.17173995	0.0101	50.02605337	0.0133	53.04153714	0.0165
46.30343958	0.0102	50.13440128	0.0134	53.11835858	0.0166
46.4343714	0.0103	50.24195616	0.0135	53.19395774	0.0167
46.56454468	0.0104	50.34870856	0.0136	53.2683195	0.0168
46.6939679	0.0105	50.45464863	0.0137	53.34142884	0.0169
46.82264881	0.0106	50.55976614	0.0138	53.41327077	0.017
46.95059439	0.0107	50.66405051	0.0139	53.48383042	0.0171
47.07781088	0.0108	50.76749079	0.014	53.55309301	0.0172
47.20430385	0.0109	50.87007569	0.0141	53.62104388	0.0173
47.3300781	0.011	50.9717936	0.0142	53.68766849	0.0174
47.45513779	0.0111	51.0726326	0.0143	53.75295243	0.0175
47.57948638	0.0112	51.17258045	0.0144	53.81688147	0.0176
47.70312665	0.0113	51.27162463	0.0145	53.87944152	0.0177
47.82606074	0.0114	51.36975238	0.0146	53.94061867	0.0178
47.94829014	0.0115	51.46695062	0.0147	54.00039918	0.0179
48.06981572	0.0116	51.56320609	0.0148	54.05876955	0.018
48.1906377	0.0117	51.65850526	0.0149	54.11571643	0.0181
48.3107557	0.0118	51.75283438	0.015	54.17122673	0.0182
48.43016876	0.0119	51.84617953	0.0151	54.22528757	0.0183
48.54887531	0.012	51.93852659	0.0152	54.2778863	0.0184
48.6668732	0.0121	52.02986124	0.0153	54.32901052	0.0185
48.78415973	0.0122	52.12016906	0.0154	54.37864809	0.0186
48.90073164	0.0123	52.20943543	0.0155	54.42678712	0.0187
49.01658512	0.0124	52.29764564	0.0156	54.47341599	0.0188

Table A.7: 80 mN paperboard plastic modelling data - Part 3.

Stress [MPa]	Strain [-]	Stress [MPa]	Strain [-]	Stress [MPa]	Strain [-]
54.51852336	0.0189	55.49318575	0.0221	56.37981397	0.0253
54.56209817	0.019	55.52089289	0.0222	56.4075211	0.0254
54.60412965	0.0191	55.54860002	0.0223	56.43522823	0.0255
54.64460733	0.0192	55.57630715	0.0224	56.46293536	0.0256
54.68352103	0.0193	55.60401428	0.0225	56.4906425	0.0257
54.72086087	0.0194	55.63172141	0.0226	56.51834963	0.0258
54.75661731	0.0195	55.65942854	0.0227	56.54605676	0.0259
54.79078109	0.0196	55.68713568	0.0228	56.57376389	0.026
54.82334329	0.0197	55.71484281	0.0229	56.60147102	0.0261
54.85429531	0.0198	55.74254994	0.023	56.62917815	0.0262
54.88362886	0.0199	55.77025707	0.0231	56.65688529	0.0263
54.91133599	0.02	55.7979642	0.0232	56.68459242	0.0264
54.93904312	0.0201	55.82567133	0.0233	56.71229955	0.0265
54.96675025	0.0202	55.85337847	0.0234	56.74000668	0.0266
54.99445738	0.0203	55.8810856	0.0235	56.76771381	0.0267
55.02216451	0.0204	55.90879273	0.0236	56.79542094	0.0268
55.04987165	0.0205	55.93649986	0.0237	56.82312808	0.0269
55.07757878	0.0206	55.96420699	0.0238	56.85083521	0.027
55.10528591	0.0207	55.99191412	0.0239	56.87854234	0.0271
55.13299304	0.0208	56.01962126	0.024	56.90624947	0.0272
55.16070017	0.0209	56.04732839	0.0241	56.9339566	0.0273
55.1884073	0.021	56.07503552	0.0242	56.96166373	0.0274
55.21611444	0.0211	56.10274265	0.0243	56.98937087	0.0275
55.24382157	0.0212	56.13044978	0.0244	57.017078	0.0276
55.2715287	0.0213	56.15815691	0.0245	57.04478513	0.0277
55.29923583	0.0214	56.18586405	0.0246	57.07249226	0.0278
55.32694296	0.0215	56.21357118	0.0247	57.10019939	0.0279
55.35465009	0.0216	56.24127831	0.0248	57.12790653	0.028
55.38235723	0.0217	56.26898544	0.0249	57.15561366	0.0281
55.41006436	0.0218	56.29669257	0.025	57.18332079	0.0282
55.43777149	0.0219	56.32439971	0.0251	57.21102792	0.0283
55.46547862	0.022	56.35210684	0.0252	57.23873505	0.0284

Table A.8: 80 mN paperboard plastic modelling data - Part 4.

Stress [MPa]	Strain [-]	Stress [MPa]	Strain [-]	Stress [MPa]	Strain [-]
57.26644218	0.0285	57.43268497	0.0291	57.57122063	0.0296
57.29414932	0.0286	57.46039211	0.0292	57.59892776	0.0297
57.32185645	0.0287	57.48809924	0.0293	57.6266349	0.0298
57.34956358	0.0288	57.51580637	0.0294	57.65434203	0.0299
57.37727071	0.0289	57.5435135	0.0295	57.68204916	0.03
57.40497784	0.029				

150 mN Paperboard

Table A.9: 150 mN paperboard plastic modelling data - Part 1.

Stress [MPa]	Strain [-]	Stress [MPa]	Strain [-]	Stress [MPa]	Strain [-]
11.67100672	0	25.19407072	0.0016	30.66334198	0.0032
13.69968164	0.0001	25.62998275	0.0017	30.92997846	0.0033
15.21356082	0.0002	26.04863034	0.0018	31.19052758	0.0034
16.45650534	0.0003	26.45143116	0.0019	31.44528677	0.0035
17.52533748	0.0004	26.83962766	0.002	31.69453285	0.0036
18.47026865	0.0005	27.21431596	0.0021	31.93852403	0.0037
19.32131661	0.0006	27.57646887	0.0022	32.17750158	0.0038
20.09811886	0.0007	27.92695448	0.0023	32.41169136	0.0039
20.81435313	0.0008	28.26655126	0.0024	32.64130514	0.004
21.47999741	0.0009	28.59596047	0.0025	32.86654178	0.0041
22.10259482	0.001	28.91581653	0.0026	33.08758834	0.0042
22.68801168	0.0011	29.22669554	0.0027	33.30462099	0.0043
23.2409167	0.0012	29.52912253	0.0028	33.51780591	0.0044
23.76509741	0.0013	29.82357759	0.0029	33.72729999	0.0045
24.26367658	0.0014	30.11050106	0.003	33.93325162	0.0046
24.73926478	0.0015	30.390298	0.0031	34.13580123	0.0047

Table A.10: 150 mN paperboard plastic modelling data - Part 2.

Stress [MPa]	Strain [-]	Stress [MPa]	Strain [-]	Stress [MPa]	Strain [-]
34.33508193	0.0048	39.53064045	0.008	43.52164741	0.0112
34.53121997	0.0049	39.66783344	0.0081	43.63594672	0.0113
34.72433526	0.005	39.80399421	0.0082	43.74973097	0.0114
34.91454176	0.0051	39.93915261	0.0083	43.86300494	0.0115
35.10194791	0.0052	40.07333732	0.0084	43.97577283	0.0116
35.28665694	0.0053	40.20657593	0.0085	44.08803829	0.0117
35.46876726	0.0054	40.33889495	0.0086	44.19980445	0.0118
35.64837271	0.0055	40.47031985	0.0087	44.3110739	0.0119
35.82556284	0.0056	40.6008751	0.0088	44.4218487	0.012
36.00042322	0.0057	40.73058418	0.0089	44.53213041	0.0121
36.17303559	0.0058	40.85946964	0.009	44.64192007	0.0122
36.34347817	0.0059	40.98755308	0.0091	44.75121823	0.0123
36.51182577	0.006	41.11485523	0.0092	44.86002494	0.0124
36.67815004	0.0061	41.24139592	0.0093	44.96833977	0.0125
36.84251963	0.0062	41.36719416	0.0094	45.07616181	0.0126
37.00500032	0.0063	41.49226809	0.0095	45.18348967	0.0127
37.16565519	0.0064	41.61663507	0.0096	45.29032152	0.0128
37.32454478	0.0065	41.74031167	0.0097	45.39665505	0.0129
37.48172715	0.0066	41.86331367	0.0098	45.50248751	0.013
37.63725808	0.0067	41.98565611	0.0099	45.6078157	0.0131
37.79119114	0.0068	42.10735328	0.01	45.71263601	0.0132
37.94357777	0.0069	42.22841876	0.0101	45.81694437	0.0133
38.09446743	0.007	42.34886541	0.0102	45.92073632	0.0134
38.24390766	0.0071	42.4687054	0.0103	46.02400696	0.0135
38.39194416	0.0072	42.58795023	0.0104	46.12675101	0.0136
38.53862088	0.0073	42.70661073	0.0105	46.22896276	0.0137
38.6839801	0.0074	42.82469705	0.0106	46.33063616	0.0138
38.82806249	0.0075	42.94221873	0.0107	46.43176473	0.0139
38.97090716	0.0076	43.05918467	0.0108	46.53234164	0.014
39.11255175	0.0077	43.17560315	0.0109	46.6323597	0.0141
39.25303249	0.0078	43.29148181	0.011	46.73181135	0.0142
39.39238421	0.0079	43.40682775	0.0111	46.83068867	0.0143

Table A.11: 150 mN paperboard plastic modelling data - Part 3.

Stress [MPa]	Strain [-]	Stress [MPa]	Strain [-]	Stress [MPa]	Strain [-]
46.92898344	0.0144	49.72258125	0.0176	52.26220484	0.0208
47.02668706	0.0145	49.80194448	0.0177	52.34156807	0.0209
47.12379065	0.0146	49.88130772	0.0178	52.42093131	0.021
47.22028499	0.0147	49.96067096	0.0179	52.50029455	0.0211
47.31616056	0.0148	50.0400342	0.018	52.57965778	0.0212
47.41140754	0.0149	50.11939743	0.0181	52.65902102	0.0213
47.50601585	0.015	50.19876067	0.0182	52.73838426	0.0214
47.59997509	0.0151	50.27812391	0.0183	52.81774749	0.0215
47.69327465	0.0152	50.35748714	0.0184	52.89711073	0.0216
47.7859036	0.0153	50.43685038	0.0185	52.97647397	0.0217
47.87785082	0.0154	50.51621362	0.0186	53.05583721	0.0218
47.96910491	0.0155	50.59557686	0.0187	53.13520044	0.0219
48.05965427	0.0156	50.67494009	0.0188	53.21456368	0.022
48.14948708	0.0157	50.75430333	0.0189	53.29392692	0.0221
48.23859131	0.0158	50.83366657	0.019	53.37329015	0.0222
48.32695474	0.0159	50.9130298	0.0191	53.45265339	0.0223
48.41456496	0.016	50.99239304	0.0192	53.53201663	0.0224
48.50140938	0.0161	51.07175628	0.0193	53.61137987	0.0225
48.58747528	0.0162	51.15111952	0.0194	53.6907431	0.0226
48.67274975	0.0163	51.23048275	0.0195	53.77010634	0.0227
48.75721977	0.0164	51.30984599	0.0196	53.84946958	0.0228
48.84087217	0.0165	51.38920923	0.0197	53.92883281	0.0229
48.92369368	0.0166	51.46857246	0.0198	54.00819605	0.023
49.00567092	0.0167	51.5479357	0.0199	54.08755929	0.0231
49.08679041	0.0168	51.62729894	0.02	54.16692253	0.0232
49.16703859	0.0169	51.70666218	0.0201	54.24628576	0.0233
49.24640183	0.017	51.78602541	0.0202	54.325649	0.0234
49.32576506	0.0171	51.86538865	0.0203	54.40501224	0.0235
49.4051283	0.0172	51.94475189	0.0204	54.48437547	0.0236
49.48449154	0.0173	52.02411512	0.0205	54.56373871	0.0237
49.56385477	0.0174	52.10347836	0.0206	54.64310195	0.0238
49.64321801	0.0175	52.1828416	0.0207	54.72246519	0.0239

Table A.12: 150 mN paperboard plastic modelling data - Part 4.

Stress [MPa]	Strain [-]	Stress [MPa]	Strain [-]	Stress [MPa]	Strain [-]
54.80182842	0.024	56.4684564	0.0261	58.13508438	0.0282
54.88119166	0.0241	56.54781964	0.0262	58.21444762	0.0283
54.9605549	0.0242	56.62718288	0.0263	58.29381085	0.0284
55.03991813	0.0243	56.70654611	0.0264	58.37317409	0.0285
55.11928137	0.0244	56.78590935	0.0265	58.45253733	0.0286
55.19864461	0.0245	56.86527259	0.0266	58.53190057	0.0287
55.27800784	0.0246	56.94463582	0.0267	58.6112638	0.0288
55.35737108	0.0247	57.02399906	0.0268	58.69062704	0.0289
55.43673432	0.0248	57.1033623	0.0269	58.76999028	0.029
55.51609756	0.0249	57.18272554	0.027	58.84935351	0.0291
55.59546079	0.025	57.26208877	0.0271	58.92871675	0.0292
55.67482403	0.0251	57.34145201	0.0272	59.00807999	0.0293
55.75418727	0.0252	57.42081525	0.0273	59.08744323	0.0294
55.8335505	0.0253	57.50017848	0.0274	59.16680646	0.0295
55.91291374	0.0254	57.57954172	0.0275	59.2461697	0.0296
55.99227698	0.0255	57.65890496	0.0276	59.32553294	0.0297
56.07164022	0.0256	57.7382682	0.0277	59.40489617	0.0298
56.15100345	0.0257	57.81763143	0.0278	59.48425941	0.0299
56.23036669	0.0258	57.89699467	0.0279	59.56362265	0.03
56.30972993	0.0259	57.97635791	0.028		
56.38909316	0.026	58.05572114	0.0281		

260 mN Paperboard

Table A.13: 260 mN paperboard plastic modelling data - Part 1.

Stress [MPa]	Strain [-]	Stress [MPa]	Strain [-]	Stress [MPa]	Strain [-]
8.600144006	0	26.54644891	0.0031	31.77653045	0.0062
10.91798034	0.0001	26.77807312	0.0032	31.90187374	0.0063
12.4977138	0.0002	27.00342718	0.0033	32.02556075	0.0064
13.74868873	0.0003	27.22282961	0.0034	32.14765591	0.0065
14.80200108	0.0004	27.43657629	0.0035	32.26822136	0.0066
15.71973849	0.0005	27.64494267	0.0036	32.38731711	0.0067
16.53713333	0.0006	27.84818573	0.0037	32.50500112	0.0068
17.27645867	0.0007	28.04654571	0.0038	32.62132938	0.0069
17.95285519	0.0008	28.24024759	0.0039	32.73635608	0.007
18.57716882	0.0009	28.42950246	0.004	32.85013362	0.0071
19.15748366	0.001	28.61450869	0.0041	32.96271274	0.0072
19.70001602	0.0011	28.79545307	0.0042	33.07414258	0.0073
20.20966764	0.0012	28.97251166	0.0043	33.18447077	0.0074
20.69038463	0.0013	29.14585073	0.0044	33.29374347	0.0075
21.14539948	0.0014	29.3156275	0.0045	33.40200546	0.0076
21.57739959	0.0015	29.48199082	0.0046	33.50930019	0.0077
21.98864782	0.0016	29.64508184	0.0047	33.61566984	0.0078
22.38107088	0.0017	29.80503453	0.0048	33.72115536	0.0079
22.75632532	0.0018	29.96197622	0.0049	33.82579653	0.008
23.11584781	0.0019	30.11602809	0.005	33.92963201	0.0081
23.46089396	0.002	30.26730554	0.0051	34.03269939	0.0082
23.79256877	0.0021	30.41591866	0.0052	34.1350352	0.0083
24.11185082	0.0022	30.5619725	0.0053	34.23667496	0.0084
24.41961167	0.0023	30.70556746	0.0054	34.33765326	0.0085
24.71663158	0.0024	30.84679957	0.0055	34.43800373	0.0086
25.00361242	0.0025	30.98576077	0.0056	34.53775909	0.0087
25.2811883	0.0026	31.12253912	0.0057	34.63695121	0.0088
25.54993443	0.0027	31.25721912	0.0058	34.7356111	0.0089
25.81037454	0.0028	31.38988186	0.0059	34.83376895	0.009
26.06298715	0.0029	31.52060521	0.006	34.93145417	0.0091
26.30821085	0.003	31.64946406	0.0061	35.02869538	0.0092

Table A.14: 260 mN paperboard plastic modelling data - Part 2.

Stress [MPa]	Strain [-]	Stress [MPa]	Strain [-]	Stress [MPa]	Strain [-]
35.12552045	0.0093	38.13652252	0.0125	41.24225003	0.0157
35.22195652	0.0094	38.23102335	0.0126	41.341112	0.0158
35.31803002	0.0095	38.32567978	0.0127	41.43994596	0.0159
35.41376668	0.0096	38.42049795	0.0128	41.53873197	0.016
35.50919152	0.0097	38.51548336	0.0129	41.63744919	0.0161
35.60432893	0.0098	38.61064081	0.013	41.73607588	0.0162
35.69920262	0.0099	38.70597443	0.0131	41.83458939	0.0163
35.79383566	0.01	38.80148765	0.0132	41.93296621	0.0164
35.88825048	0.0101	38.8971832	0.0133	42.03118193	0.0165
35.98246889	0.0102	38.99306309	0.0134	42.12921129	0.0166
36.07651209	0.0103	39.08912861	0.0135	42.22702815	0.0167
36.17040065	0.0104	39.18538031	0.0136	42.32460558	0.0168
36.26415456	0.0105	39.281818	0.0137	42.42191579	0.0169
36.35779321	0.0106	39.37844072	0.0138	42.51893021	0.017
36.45133538	0.0107	39.47524674	0.0139	42.61561948	0.0171
36.54479928	0.0108	39.57223358	0.014	42.71195348	0.0172
36.63820253	0.0109	39.66939792	0.0141	42.80790139	0.0173
36.73156217	0.011	39.76673567	0.0142	42.90343163	0.0174
36.82489464	0.0111	39.86424192	0.0143	42.998512	0.0175
36.91821583	0.0112	39.96191093	0.0144	43.0931096	0.0176
37.01154103	0.0113	40.05973613	0.0145	43.18719095	0.0177
37.10488495	0.0114	40.15771009	0.0146	43.28072199	0.0178
37.19826173	0.0115	40.25582456	0.0147	43.37366809	0.0179
37.2916849	0.0116	40.35407039	0.0148	43.46599414	0.018
37.38516743	0.0117	40.45243759	0.0149	43.55766455	0.0181
37.47872169	0.0118	40.55091525	0.015	43.6486433	0.0182
37.57235944	0.0119	40.64949162	0.0151	43.73889401	0.0183
37.66609187	0.012	40.74815403	0.0152	43.82837992	0.0184
37.75992954	0.0121	40.8468889	0.0153	43.91706401	0.0185
37.85388241	0.0122	40.94568177	0.0154	44.004909	0.0186
37.94795983	0.0123	41.04451726	0.0155	44.0918774	0.0187
38.0421705	0.0124	41.14337908	0.0156	44.17793158	0.0188

Table A.15: 260 mN paperboard plastic modelling data - Part 3.

Stress [MPa]	Strain [-]	Stress [MPa]	Strain [-]	Stress [MPa]	Strain [-]
44.26303381	0.0189	46.64095816	0.0221	48.9501008	0.0253
44.34714628	0.019	46.71311887	0.0222	49.0222615	0.0254
44.43023121	0.0191	46.78527958	0.0223	49.09442221	0.0255
44.51225085	0.0192	46.85744029	0.0224	49.16658292	0.0256
44.59316755	0.0193	46.92960099	0.0225	49.23874363	0.0257
44.6729438	0.0194	47.0017617	0.0226	49.31090433	0.0258
44.75154231	0.0195	47.07392241	0.0227	49.38306504	0.0259
44.82892602	0.0196	47.14608312	0.0228	49.45522575	0.026
44.90505817	0.0197	47.21824382	0.0229	49.52738645	0.0261
44.97990237	0.0198	47.29040453	0.023	49.59954716	0.0262
45.0534226	0.0199	47.36256524	0.0231	49.67170787	0.0263
45.12558331	0.02	47.43472594	0.0232	49.74386858	0.0264
45.19774402	0.0201	47.50688665	0.0233	49.81602928	0.0265
45.26990473	0.0202	47.57904736	0.0234	49.88818999	0.0266
45.34206543	0.0203	47.65120807	0.0235	49.9603507	0.0267
45.41422614	0.0204	47.72336877	0.0236	50.03251141	0.0268
45.48638685	0.0205	47.79552948	0.0237	50.10467211	0.0269
45.55854756	0.0206	47.86769019	0.0238	50.17683282	0.027
45.63070826	0.0207	47.93985089	0.0239	50.24899353	0.0271
45.70286897	0.0208	48.0120116	0.024	50.32115423	0.0272
45.77502968	0.0209	48.08417231	0.0241	50.39331494	0.0273
45.84719038	0.021	48.15633302	0.0242	50.46547565	0.0274
45.91935109	0.0211	48.22849372	0.0243	50.53763636	0.0275
45.9915118	0.0212	48.30065443	0.0244	50.60979706	0.0276
46.06367251	0.0213	48.37281514	0.0245	50.68195777	0.0277
46.13583321	0.0214	48.44497585	0.0246	50.75411848	0.0278
46.20799392	0.0215	48.51713655	0.0247	50.82627919	0.0279
46.28015463	0.0216	48.58929726	0.0248	50.89843989	0.028
46.35231534	0.0217	48.66145797	0.0249	50.9706006	0.0281
46.42447604	0.0218	48.73361867	0.025	51.04276131	0.0282
46.49663675	0.0219	48.80577938	0.0251	51.11492201	0.0283
46.56879746	0.022	48.87794009	0.0252	51.18708272	0.0284

Table A.16: 260 mN paperboard plastic modelling data - Part 4.

Stress [MPa]	Strain [-]	Stress [MPa]	Strain [-]	Stress [MPa]	Strain [-]
51.25924343	0.0285	51.69220767	0.0291	52.12517192	0.0297
51.33140414	0.0286	51.76436838	0.0292	52.19733262	0.0298
51.40356484	0.0287	51.83652909	0.0293	52.26949333	0.0299
51.47572555	0.0288	51.90868979	0.0294	52.34165404	0.03
51.54788626	0.0289	51.9808505	0.0295		
51.62004697	0.029	52.05301121	0.0296		

Appendix B

Mean results - Screening tests

Table B.1: Mean values of the measured responses from the screening tests.

Test	Measured force	Out-of-plane strain	Test	Measured force	Out-of-plane strain	Test	Measured force	Out-of-plane strain
1.1	14.58	0.64	5.3	13.80	0.82	10.2	12.81	0.92
1.2	14.16	0.87	6.1	12.55	0.96	10.3	14.49	0.87
1.3	14.32	0.77	6.2	13.00	0.76	11.1	8.10	0.62
2.1	6.88	0.32	6.3	13.95	0.48	11.2	9.63	0.62
2.2	6.65	0.84	7.1	13.74	0.75	11.3	8.86	0.63
2.3	7.49	0.49	7.2	13.60	0.78	12.1	8.74	0.54
3.1	10.64	0.99	7.3	13.83	0.73	12.2	8.20	0.59
3.2	10.46	0.42	8.1	16.42	0.66	12.3	8.30	0.64
3.3	10.90	0.29	8.2	16.93	0.32	13.1	14.21	1.00
4.1	24.90	0.35	8.3	16.16	0.35	13.2	14.12	1.13
4.2	21.14	0.64	9.1	15.72	0.72	13.3	14.57	1.05
4.3	21.71	0.44	9.2	15.50	0.82	14.1	2.98	0.05
5.1	14.57	0.85	9.3	15.26	0.72	14.2	2.91	0.17
5.2	15.01	0.59	10.1	11.58	0.96	14.3	2.99	-

Appendix C

Statistics - Screening experiments

- Out-of-plane deformation is missing
- Information about the procedure

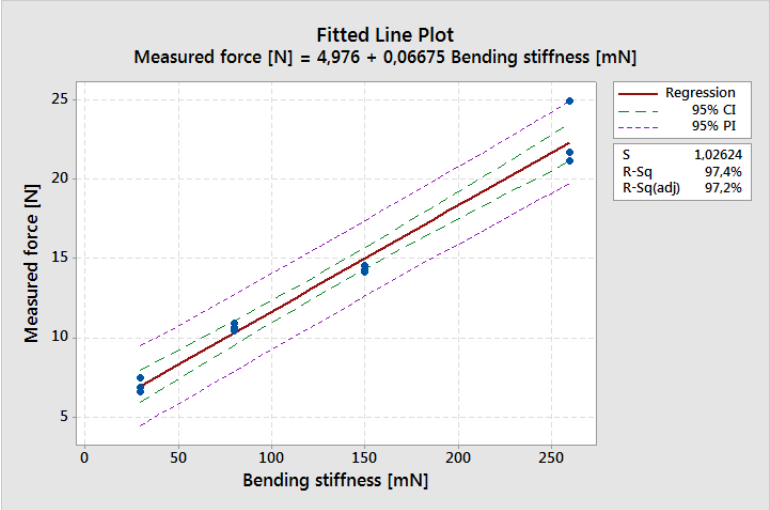

Figure C.1: Results obtained from regression analysis. Bending stiffness.

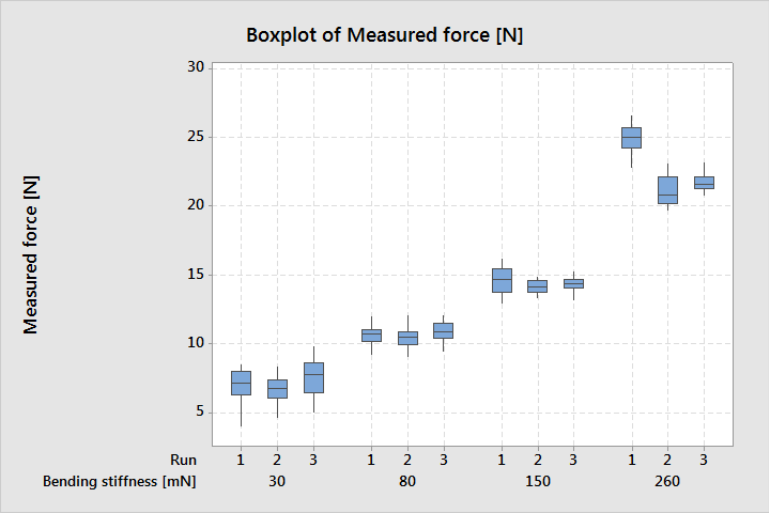

Figure C.2: Results obtained from regression analysis. Bending stiffness.

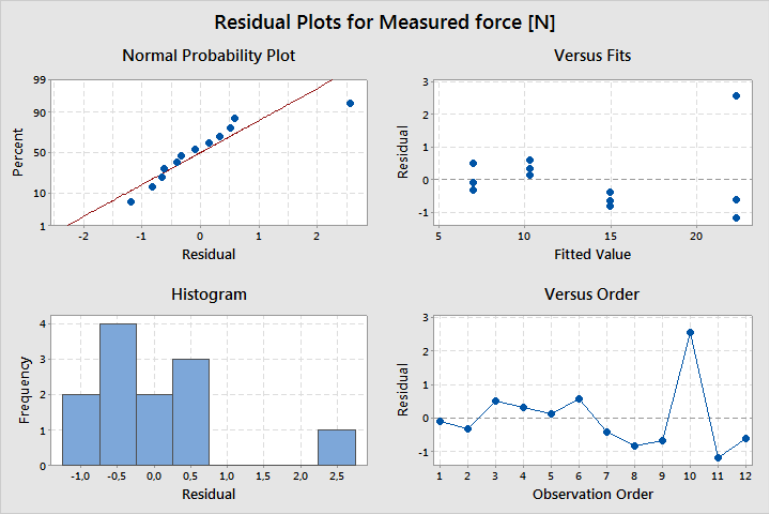

Figure C.3: Results obtained from regression analysis. Bending stiffness.

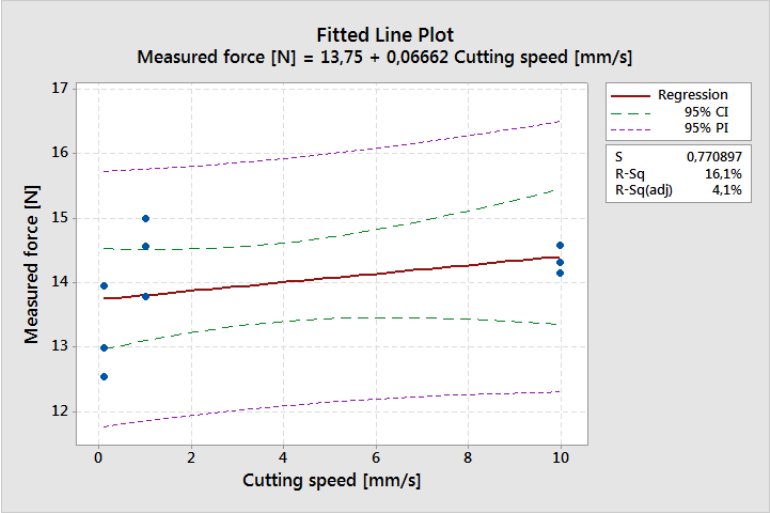

Figure C.4: Results obtained from regression analysis. Cutting speed.

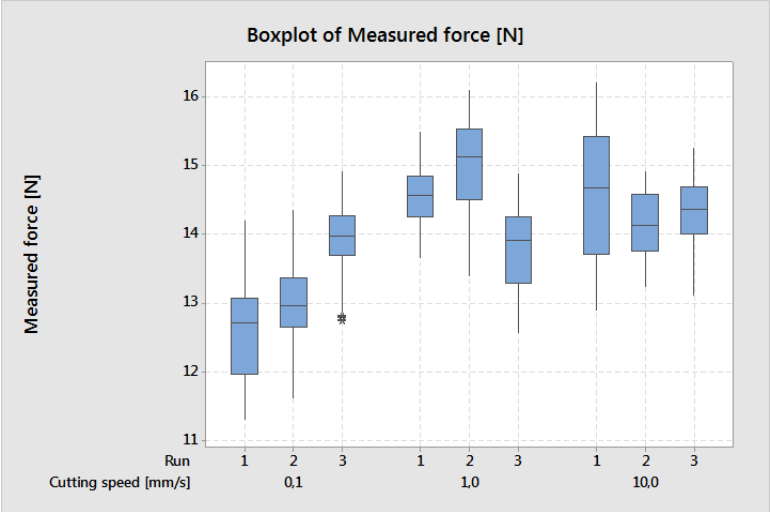

Figure C.5: Results obtained from regression analysis. Cutting speed.

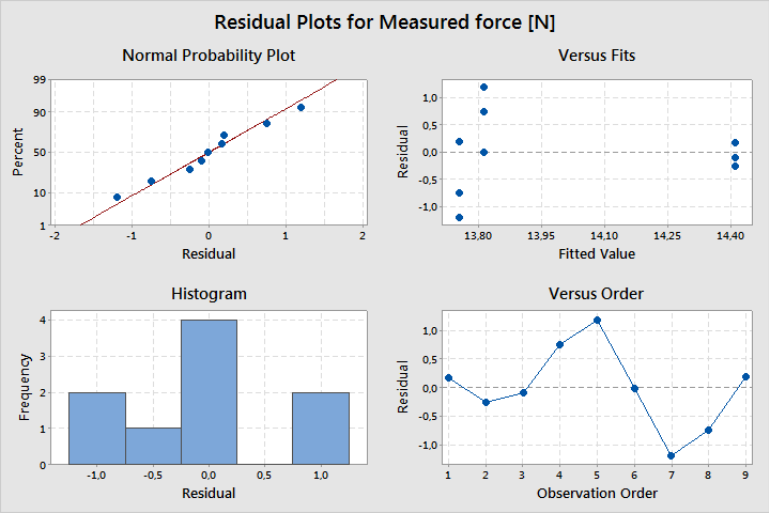

Figure C.6: Results obtained from regression analysis. Cutting speed.

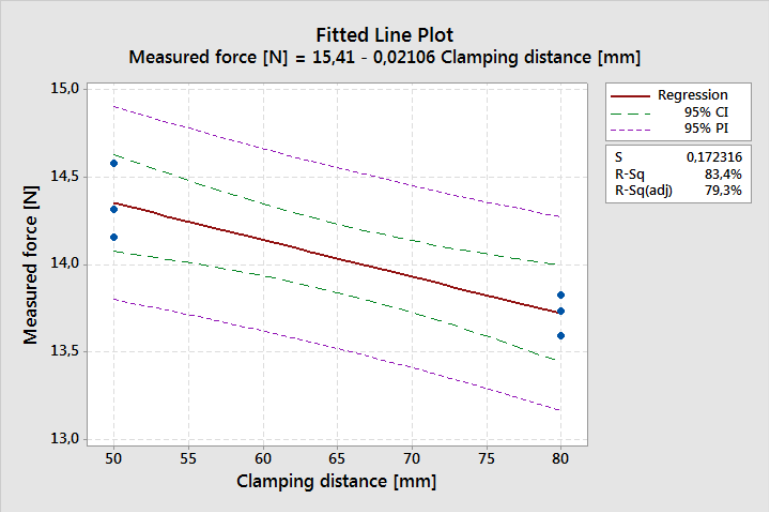

Figure C.7: Results obtained from regression analysis. Clamping distance.

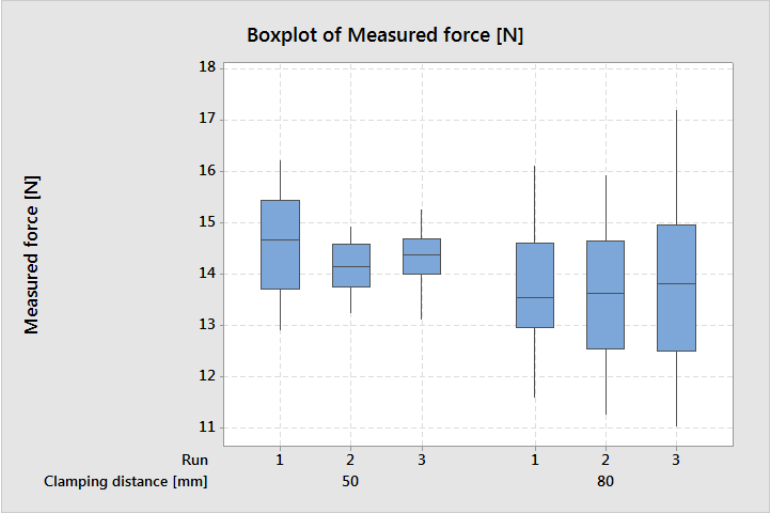

Figure C.8: Results obtained from regression analysis. Clamping distance.

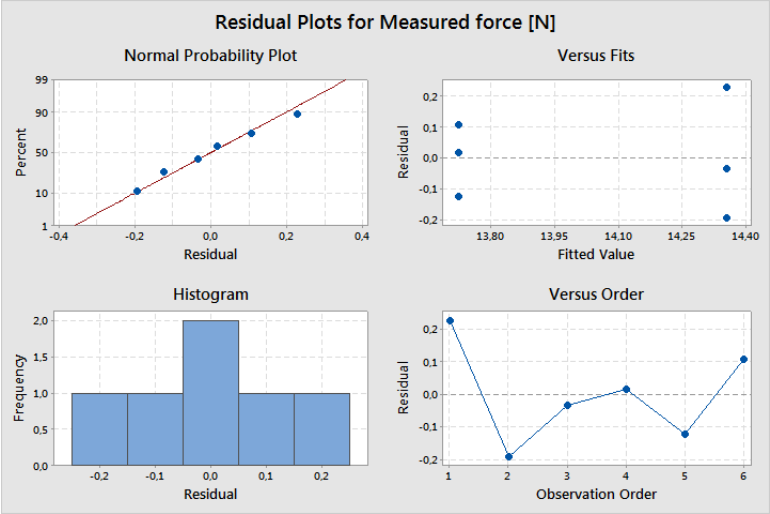

Figure C.9: Results obtained from regression analysis. Clamping distance.

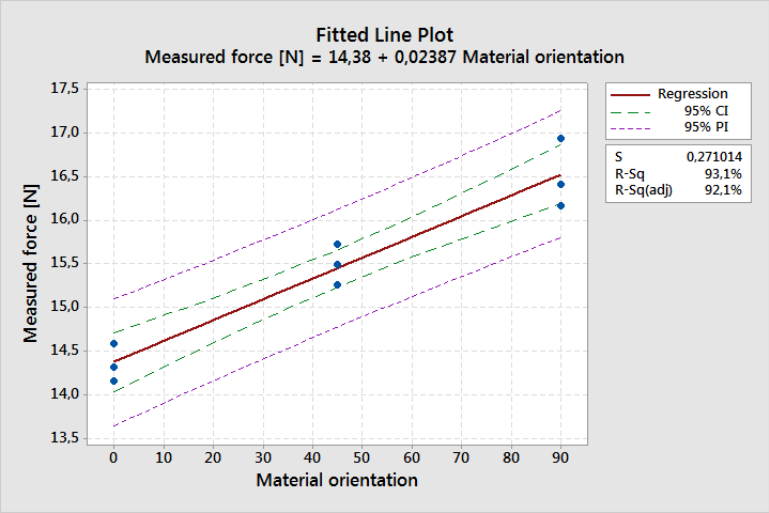

Figure C.10: Results obtained from regression analysis. Material orientation.

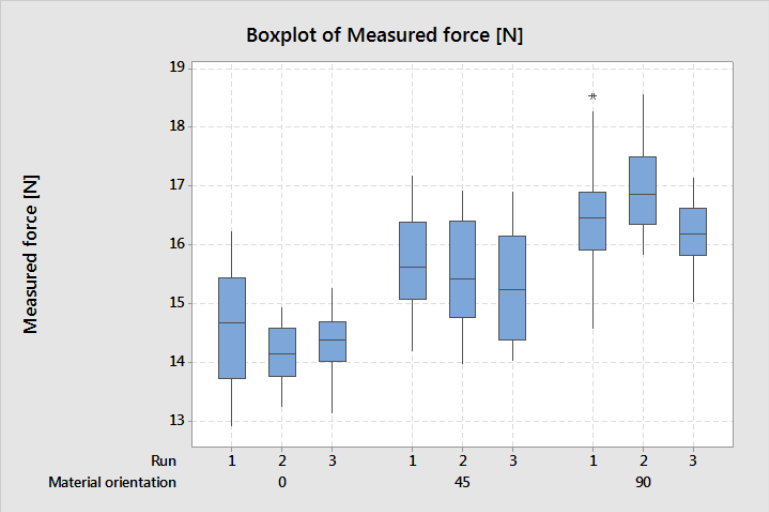

Figure C.11: Results obtained from regression analysis. Material orientation.

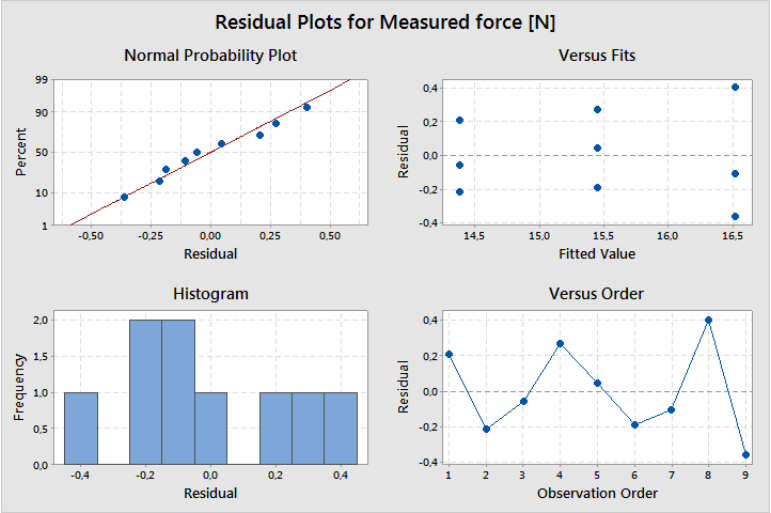

Figure C.12: Results obtained from regression analysis. Material orientation.

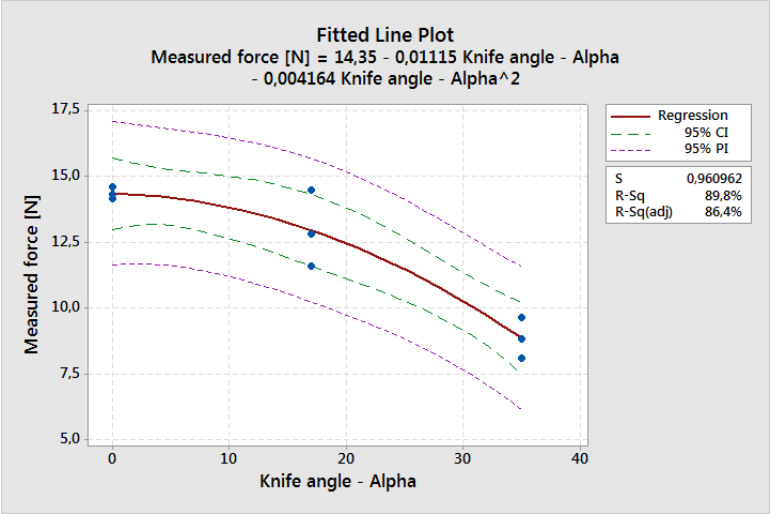

Figure C.13: Results obtained from regression analysis. Knife angle - α.

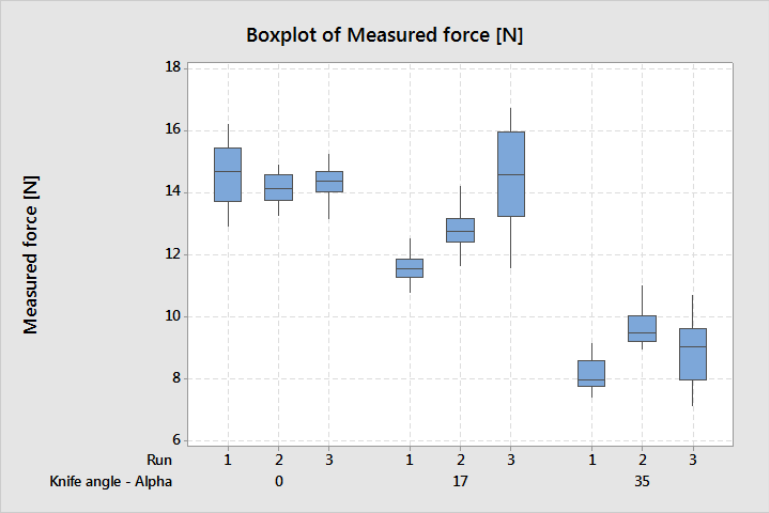

Figure C.14: Results obtained from regression analysis. Knife angle - α.

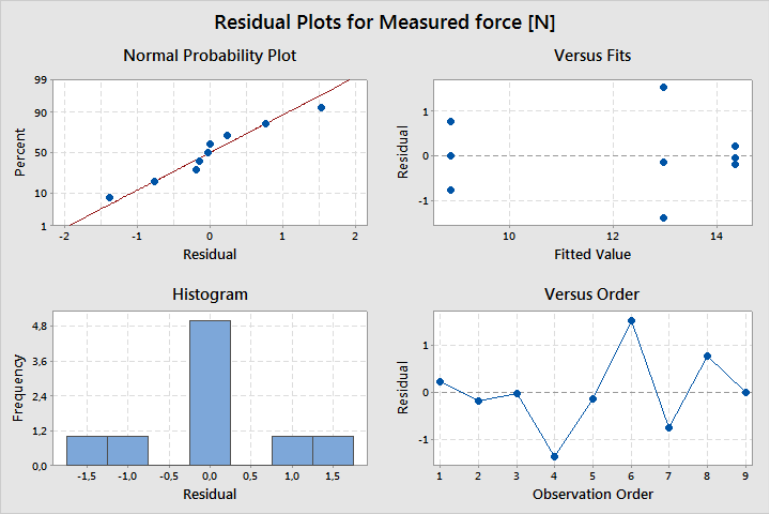

Figure C.15: Results obtained from regression analysis. Knife angle - α.

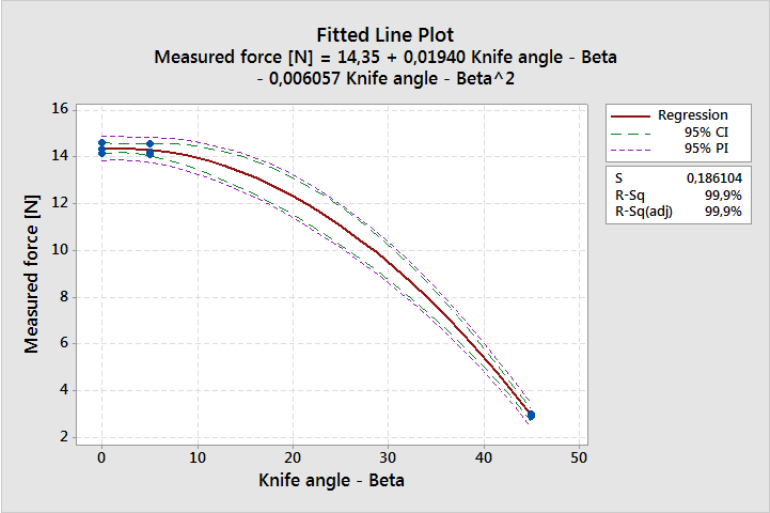

Figure C.16: Results obtained from regression analysis. Knife angle - β.

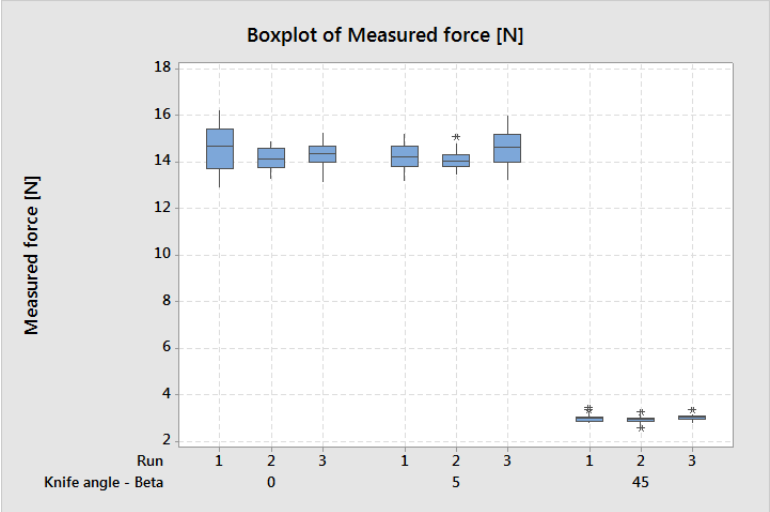

Figure C.17: Results obtained from regression analysis. Knife angle - β.

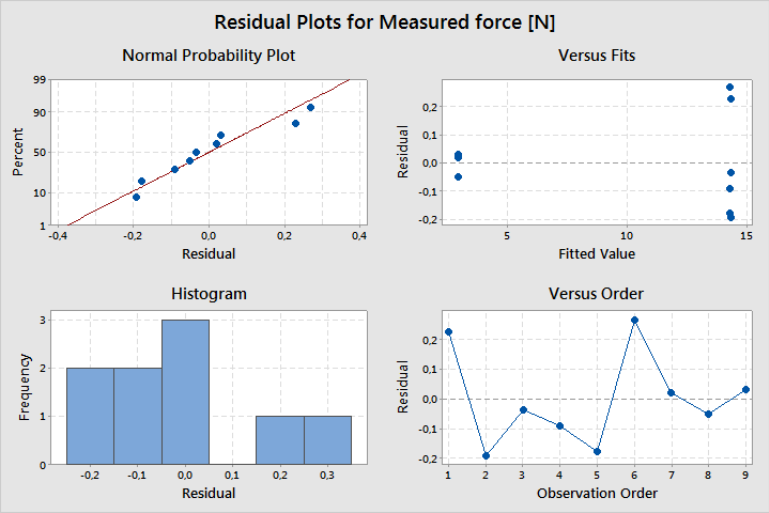

Figure C.18: Results obtained from regression analysis. Knife angle - β.

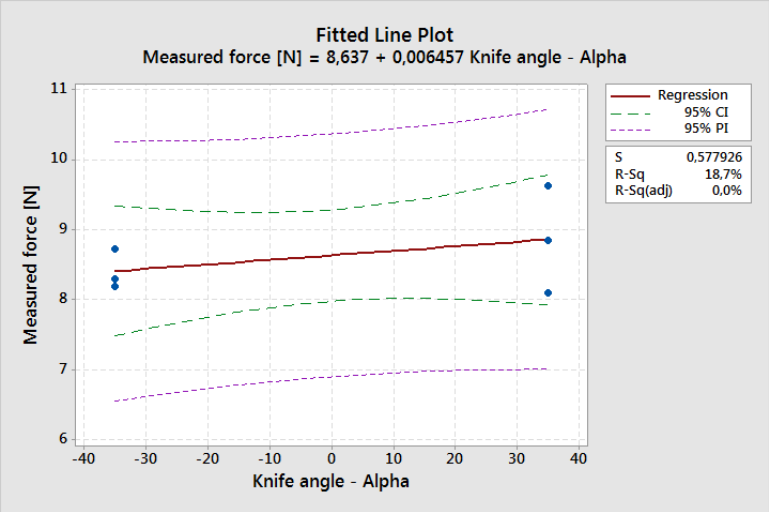

Figure C.19: Results obtained from regression analysis. Clay coating.

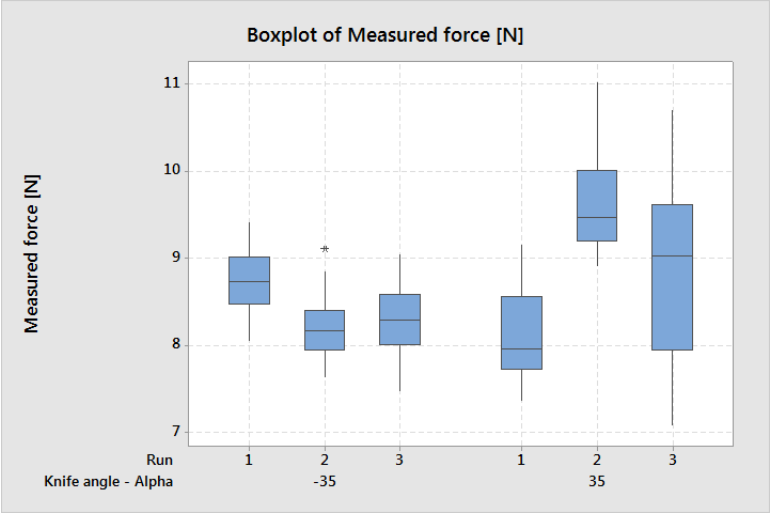

Figure C.20: Results obtained from regression analysis. Clay coating.

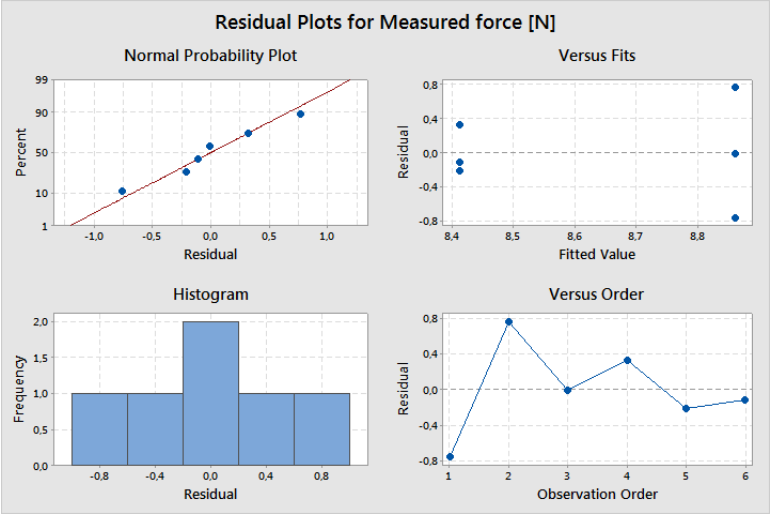

Figure C.21: Results obtained from regression analysis. Clay coating.

Appendix D

Measured results - Final experiments

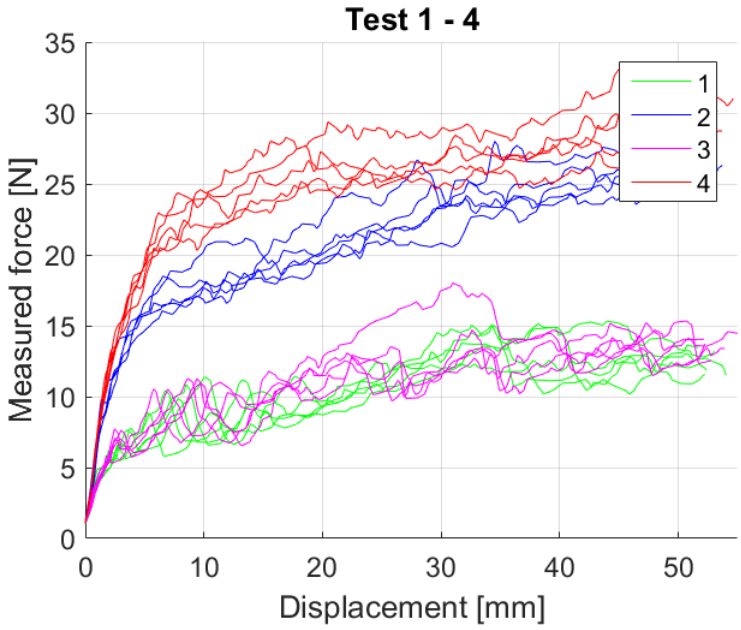

Figure D.1: Results from the final cutting tests represented in a force-displacement curve. Here are test 1 to 4 illustrated. Specific parameter data for each test setup can be found in Table 2.7.

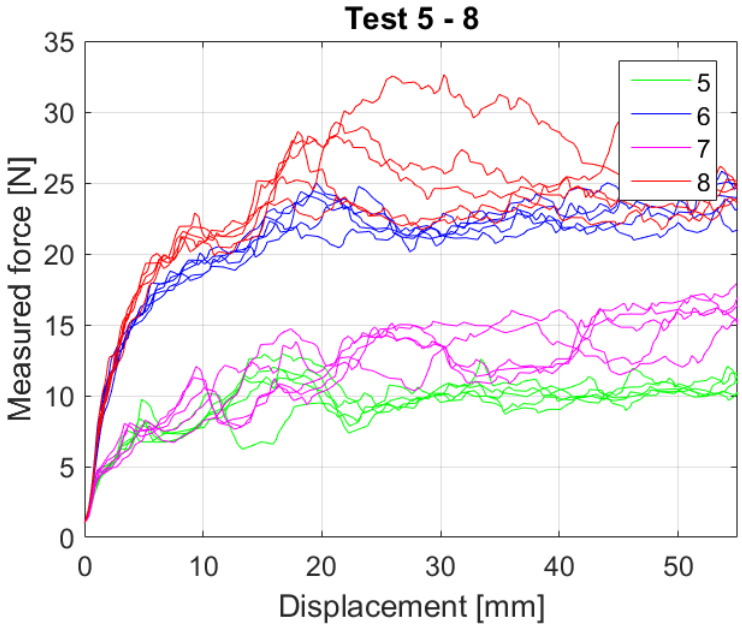

Figure D.2: Results from the final cutting tests represented in a force-displacement curve. Here are test 5 to 8 illustrated. Specific parameter data for each test setup can be found in Table 2.7.

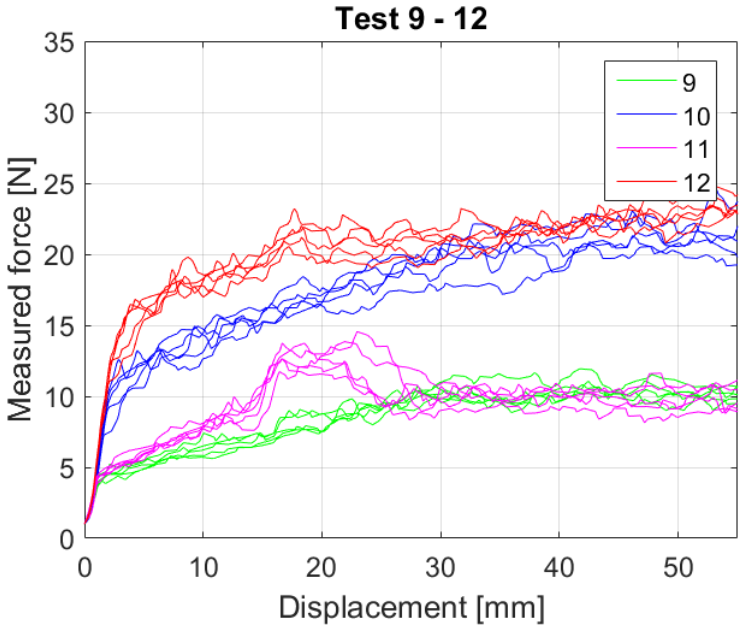

Figure D.3: Results from the final cutting tests represented in a force-displacement curve. Here are test 9 to 12 illustrated. Specific parameter data for each test setup can be found in Table 2.7.

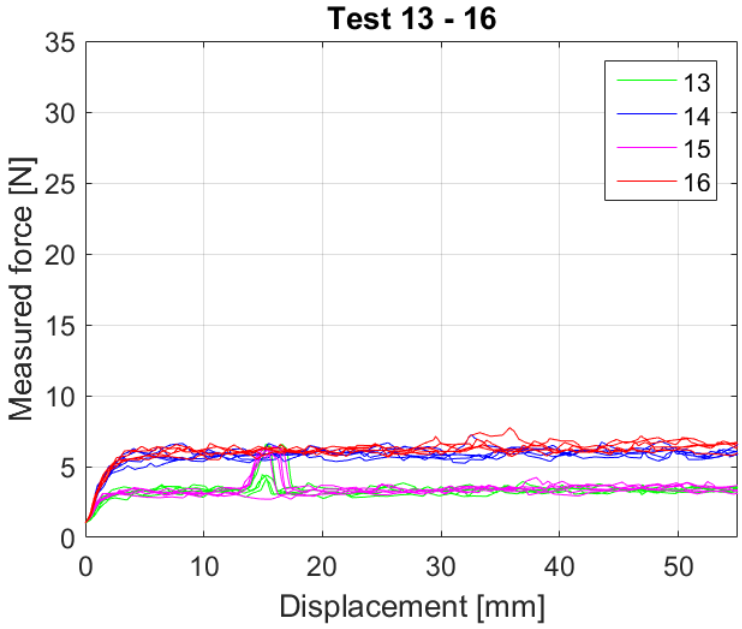

Figure D.4: Results from the final cutting tests represented in a force-displacement curve. Here are test 13 to 16 illustrated. Specific parameter data for each test setup can be found in Table 2.7.

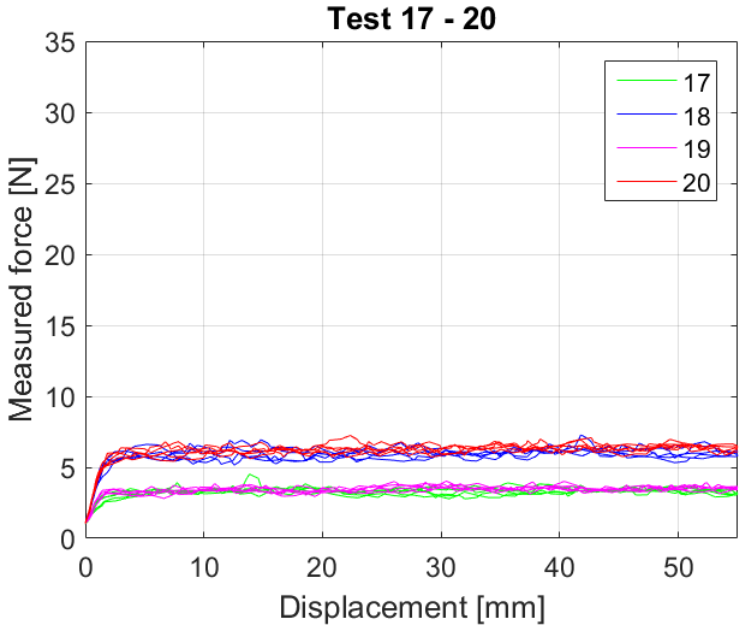

Figure D.5: Results from the final cutting tests represented in a force-displacement curve. Here are test 17 to 20 illustrated. Specific parameter data for each test setup can be found in Table 2.7.

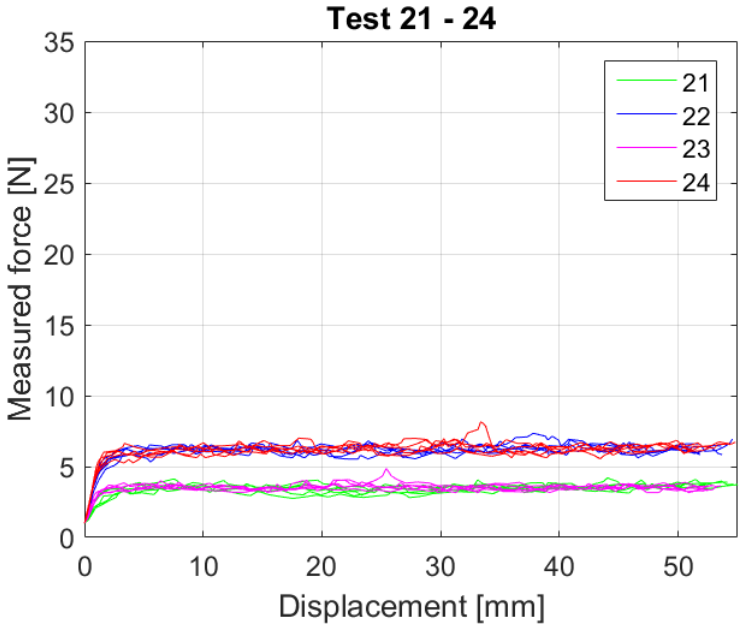

Figure D.6: Results from the final cutting tests represented in a force-displacement curve. Here are test 21 to 24 illustrated. Specific parameter data for each test setup can be found in Table 2.7.

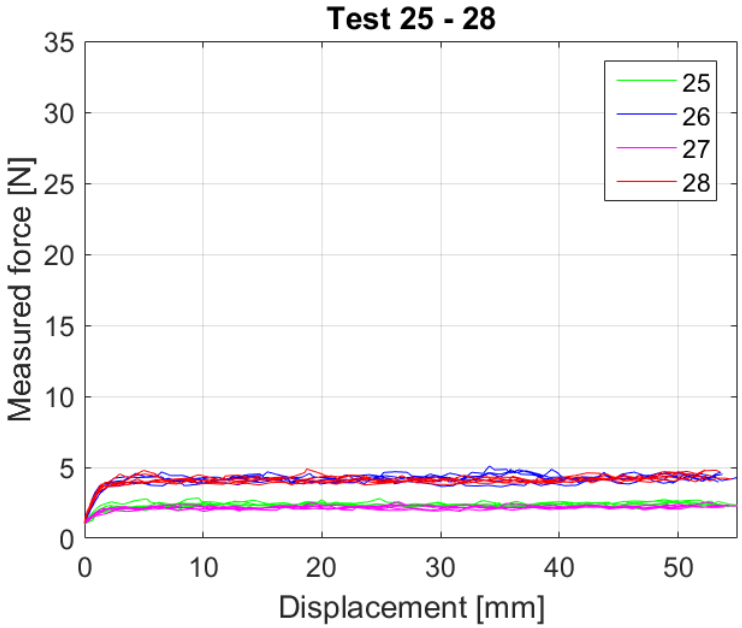

Figure D.7: Results from the final cutting tests represented in a force-displacement curve. Here are test 25 to 28 illustrated. Specific parameter data for each test setup can be found in Table 2.7.

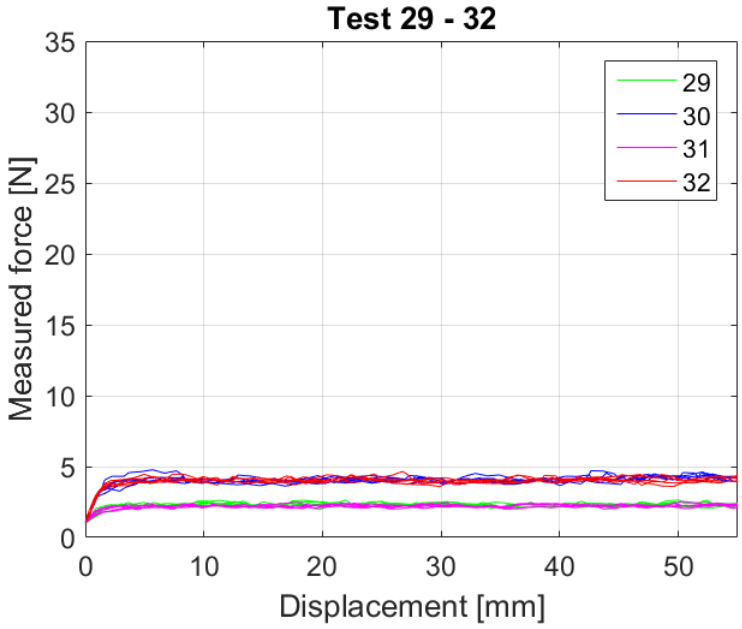

Figure D.8: Results from the final cutting tests represented in a force-displacement curve. Here are test 29 to 32 illustrated. Specific parameter data for each test setup can be found in Table 2.7.

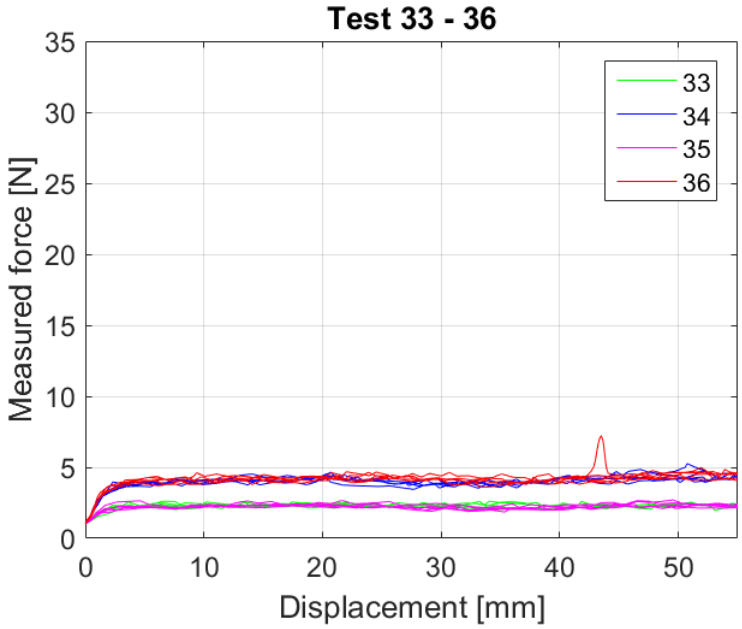

Figure D.9: Results from the final cutting tests represented in a force-displacement curve. Here are test 33 to 36 illustrated. Specific parameter data for each test setup can be found in Table 2.7.

Appendix E

Mean results - Final Experiments

Table E.1: Mean values of the measured responses from the final experiments - Part 1.

Test	Measured force	Test	Measured force	Test	Measured force	Test	Measured force	Test	Measured force
1.1	12.18	3.1	13.29	5.1	10.11	7.1	13.60	9.1	10.13
1.2	13.97	3.2	12.13	5.2	10.28	7.2	13.62	9.2	10.11
1.3	12.25	3.3	12.39	5.3	10.10	7.3	14.04	9.3	9.92
1.4	12.80	3.4	13.25	5.4	10.11	7.4	13.66	9.4	9.76
1.5	12.86	3.5	14.65	5.5	10.69	7.5	13.95	9.5	11.21
2.1	24.77	4.1	28.55	6.1	23.68	8.1	26.69	10.1	19.08
2.2	24.16	4.2	30.45	6.2	21.89	8.2	22.71	10.2	20.50
2.3	24.17	4.3	26.19	6.3	21.90	8.3	23.79	10.3	20.96
2.4	26.41	4.4	27.75	6.4	22.99	8.4	28.78	10.4	20.17
2.5	24.26	4.5	28.13	6.5	22.94	8.5	24.33	10.5	21.85

Table E.2: Mean values of the measured responses from the final experiments - Part 2.

Test	Measured force	Test	Measured force	Test	Measured force	Test	Measured force	Test	Measured force
11.1	8.88	17.1	3.51	23.1	3.47	29.1	2.27	35.1	2.13
11.2	9.94	17.2	3.19	23.2	3.61	29.2	2.35	35.2	2.12
11.3	9.87	17.3	3.54	23.3	3.48	29.3	2.26	35.3	2.18
11.4	10.50	17.4	3.33	23.4	3.61	29.4	2.29	35.4	2.35
11.5	10.32	17.5	3.17	23.5	3.37	29.5	2.30	35.5	2.25
12.1	21.28	18.1	6.04	24.1	6.61	30.1	4.10	36.1	4.18
12.2	21.73	18.2	6.04	24.2	6.09	30.2	4.16	36.2	5.06
12.3	22.31	18.3	6.33	24.3	6.31	30.3	3.92	36.3	4.05
12.4	22.60	18.4	5.97	24.4	6.44	30.4	4.08	36.4	4.13
12.5	22.19	18.5	6.07	24.5	6.31	30.5	4.24	36.5	4.15
13.1	3.29	19.1	3.55	25.1	2.47	31.1	2.26		
13.2	3.39	19.2	3.58	25.2	2.43	31.2	2.26		
13.3	3.41	19.3	3.48	25.3	2.39	31.3	2.18		
13.4	3.31	19.4	3.48	25.4	2.28	31.4	2.24		
13.5	3.36	19.5	3.49	25.5	2.32	31.5	2.16		
14.1	6.20	20.1	6.42	26.1	3.88	32.1	4.13		
14.2	6.11	20.2	6.26	26.2	4.49	32.2	4.02		
14.3	5.88	20.3	6.39	26.3	4.20	32.3	4.03		
14.4	5.74	20.4	6.48	26.4	4.33	32.4	3.92		
14.5	6.06	20.5	6.38	26.5	4.35	32.5	4.12		
15.1	3.53	21.1	3.51	27.1	2.15	33.1	2.35		
15.2	3.34	21.2	3.67	27.2	2.21	33.2	2.18		
15.3	3.39	21.3	3.37	27.3	2.16	33.3	2.23		
15.4	3.51	21.4	3.58	27.4	2.18	33.4	2.23		
15.5	3.58	21.5	3.59	27.5	2.24	33.5	2.37		
16.1	6.21	22.1	6.36	28.1	4.09	34.1	3.92		
16.2	6.84	22.2	6.18	28.2	4.20	34.2	4.07		
16.3	6.24	22.3	6.33	28.3	4.20	34.3	4.18		
16.4	6.37	22.4	6.46	28.4	4.25	34.4	4.08		
16.5	6.30	22.5	6.13	28.5	4.06	34.5	4.14		